

Copyright Warning & Restrictions

The copyright law of the United States (Title 17, United States Code) governs the making of photocopies or other reproductions of copyrighted material.

Under certain conditions specified in the law, libraries and archives are authorized to furnish a photocopy or other reproduction. One of these specified conditions is that the photocopy or reproduction is not to be “used for any purpose other than private study, scholarship, or research.” If a user makes a request for, or later uses, a photocopy or reproduction for purposes in excess of “fair use” that user may be liable for copyright infringement,

This institution reserves the right to refuse to accept a copying order if, in its judgment, fulfillment of the order would involve violation of copyright law.

Please Note: The author retains the copyright while the New Jersey Institute of Technology reserves the right to distribute this thesis or dissertation

Printing note: If you do not wish to print this page, then select “Pages from: first page # to: last page #” on the print dialog screen

The Van Houten library has removed some of the personal information and all signatures from the approval page and biographical sketches of theses and dissertations in order to protect the identity of NJIT graduates and faculty.

ABSTRACT

SYNTHESIS AND CHARACTERIZATION OF NOVEL BORON-BASED NANOSTRUCTURES AND COMPOSITES

**by
Rajen B. Patel**

A number of nanomaterials have been synthesized by using a method that has been previously utilized to make pure boron nanostructures through the addition of different reactant gases to the process. This method was pioneered by Iqbal-Liu and will be referred to as the IL method in this dissertation. The IL method successfully created boron nanowires, boron nanoflakes, and boron nanotubes. In this dissertation, by adding methane, hydrogen sulfide, and ammonia to the process, an entire family of nanomaterials is prepared. These include nanowires, nano-heterostructures, and thin nanoplatelets of a variety of elemental compositions. These materials can be integrated with other known nanostructures to form a number of novel electronic nanodevices and nanosensors.

A method to create nanocomposites by the chemical vapor infiltration (CVI) of nanomaterials into a metal matrix has been developed further. This work builds on past efforts which successfully developed carbon nanotube (CNT)-infiltrated metal composites which demonstrated enhanced mechanical strength. The nanocomposite method is successfully performed with boron nitride nanotubes in a nano-iron matrix. A graphene composite with iron is also synthesized but, unlike composites with CNTs, there was no strength enhancement. This could be attributed to the two-dimensional morphology of graphene.

To put the dissertation in perspective, a review of several characterization techniques utilized is presented, including Raman spectroscopy, scanning electron microscopy, and transmission electron microscopy. Additionally, a summary of possible novel growth mechanisms is required to explain the formation mechanism of the materials synthesized in this work. Nearly all of the materials synthesized in this work were grown with a vapor-liquid-growth mechanism. Background information on nanowires, nanotubes, and nanocomposites has also been included to clarify the significance of the research conducted. In conclusion, future experiments and some difficult to explain results are discussed.

**SYNTHESIS AND CHARACTERIZATION OF NOVEL BORON-BASED
NANOSTRUCTURES AND COMPOSITES**

by
Rajen B. Patel

**A Dissertation
Submitted to the Faculty of
New Jersey Institute of Technology
in Partial Fulfillment of the Requirements for the Degree of
Doctor of Philosophy in Materials Science and Engineering
Interdisciplinary Program in Materials Science and Engineering**

May 2013

Copyright © 2013 by Rajen B. Patel

ALL RIGHTS RESERVED

APPROVAL PAGE

**SYNTHESIS AND CHARACTERIZATION OF NOVEL BORON-BASED
NANOSTRUCTURES AND COMPOSITES**

Rajen B. Patel

Dr. Zafar Iqbal, Dissertation Co-Advisor Date
Research Professor of Chemistry and Environmental Science, NJIT

Dr. Ravindra M. Nugehalli, Dissertation Co-Advisor Date
Professor of Physics, NJIT

Dr. Marek Sosnowski, Committee Member Date
Professor of Electrical and Computer Engineering, NJIT

Dr. Boris Khusid, Committee Member Date
Professor of Chemical, Biological, and Pharmaceutical Engineering, NJIT

Dr. Frank J. Owens, Committee Member Date
Professor of Physics, Hunter College, CUNY

BIOGRAPHICAL SKETCH

Author: Rajen Bhupendra Patel

Degree: Doctor of Philosophy

Date: May 2013

Undergraduate and Graduate Education:

- Doctor of Philosophy in Materials Science & Engineering, New Jersey Institute of Technology, Newark, NJ, 2013
- Master of Science in Materials Science & Engineering, New Jersey Institute of Technology, Newark, NJ, 2008
- Bachelor of Science in Mechanical Engineering, New Jersey Institute of Technology, Newark, NJ, 2006

Major: Materials Science & Engineering

Presentations and Publications:

Rajen B. Patel, Jinwen Liu, James V. Scicolone, Sagar Roy, Somenath Mitra, Rajesh N. Dave, Zafar Iqbal, "Formation of stainless steel-carbon nanotube composites using a scalable chemical vapor infiltration process," February 2013, Journal of Materials Science Volume 48, pp 1387-1395

Rajen B. Patel, Jinwen Liu, Jennifer Eng, and Zafar Iqbal, "One-step CVD synthesis of a boron nitride nanotube-iron composite," May 2011, Journal of Materials Research, Volume 26, pp 1332-1339

This thesis is dedicated to my parents, Madhuben and Bhupendra Patel, for the boundless support they've provided. They gave me drive when I lacked ambition, courage when I had fear, and love when I was nothing.

ACKNOWLEDGMENTS

First and foremost, I would like to acknowledge my dissertation advisor, Dr. Zafar Iqbal, who has provided invaluable mentoring and support over the past 7 years. I would like to thank my department head and co-advisor, Dr. Ravindra Nuggehalli, who has helped me to navigate my doctorate and imparted wisdom freely during the process. I would like to acknowledge Dr. Frank Owens, who encouraged me to pursue advanced study, and continues to provide support to this day. I would like to thank my other committee members, Dr. Marek Sosnowski and Dr. Boris Khusid, for taking their time to evaluate my dissertation and attend my defense. I would like to thank ARDEC, Picatinny Arsenal because it was instrumental in providing funding and facilities at which to conduct some of the experiments. Much appreciation is dedicated to Chi Yu and Dr. Jinwen Liu, who worked with me over the course of a number of experiments. I would also like to acknowledge Dr. Alex Tsengming Chou of Stevens Institute of Technology, who performed the transmission electron microscopy of the nanomaterials discussed in this dissertation. I would like to thank Dr. Victor Stepanov, a colleague at ARDEC who provided guidance over the course of a number of experiments. Dr. Alokik Kanwal should also be recognized, for assistance with electrical measurements which will be performed on the materials in the thesis.

Specifically in reference to work discussed in Chapter 6, I would like to thank the following collaborators: Dr. Victor Greenhut for assistance with the SEM imaging of the fracture surface, Dr. Paul Anderson for general guidance in setting up the laboratory equipment and use of his laboratory space, Peggy Sanchez for performing the FTIR measurements, Mike Hespos for performing the hardness measurements, Sean Swaszek

for measuring the stress-strain curves, Dr. Steve Miller and Dr. Wojtek Tutak for help in obtaining the TEM images, Steve Bottglieri for Knoop hardness measurements and Ed Hochberg for UV-Visible spectroscopic analysis. I would also like to thank Dr. Wes Cobb at University of Denver for assistance in making ultrasound measurements and Bill Davis for help with image processing. In reference to work reported in Appendix B, I would like to thank Dr. Kelley Caflin and Dr. Edward Hochberg at ARDEC, Picatinny Arsenal for performing the XRD measurements and the ICP-AES chemical analysis, respectively.

TABLE OF CONTENTS

Chapter	Page
<u>1</u> INTRODUCTION	1
<u>1.1</u> The IL Method	1
<u>1.2</u> Nanowires.....	4
<u>1.3</u> Nanowire Heterostructures.....	6
<u>1.4</u> Nanotubes.....	8
<u>1.5</u> Mechanical Properties of Nanotubes.....	13
<u>1.6</u> Graphene and its Boron Nitride Analog.....	16
<u>1.7</u> Boron Carbonitride Nanotubes and Nanotube Heterostructures.....	18
<u>2</u> SYNTHESIS AND CHARACTERIZATION TECHNIQUES USED.....	23
<u>2.1</u> Chemical Vapor Deposition (CVD) Synthesis.....	23
<u>2.2</u> Scanning Electron Microscopy (SEM).....	25
<u>2.3</u> Transmission Electron Microscopy (TEM).....	28
<u>2.4</u> Selected Area Electron Diffraction (SAED).....	30
<u>2.5</u> Electron Energy Loss Spectroscopy (EELS).....	33
<u>2.6</u> Raman Spectroscopy.....	34
<u>2.7</u> Four Point Probe Electrical Characterization.....	37

TABLE OF CONTENTS
(Continued)

Chapter	Page
2.8 Other Techniques Used.....	39
2.8.1 FTIR (Fourier Transform Infrared Spectroscopy).....	39
2.8.2 Hardness.....	40
2.8.3 Compressive Test (Mechanical Property).....	41
2.8.4 ICP-AES (Inductively Coupled Plasma Atomic Emission Spectroscopy)	41
2.8.5 XRD (X-Ray Diffraction).....	42
3 CARBON BORON NANOSTRUCTURES.....	44
4 BORON NITROGEN HETEROSTRUCTURES.....	50
4.1 Magnesium Oxide Filled Boron Nitride Nanotubes.....	50
4.2 Pure Boron Nitride Nanowires.....	54
4.3 Pure Boron Nanowires and Boron Nitrogen Nanowire Heterostructures.....	56
4.4 Boron Nitride Nanotubes, Revisited.....	59
5 BORON-SULFUR NANOSTRUCTURES.....	64
5.1 Nanorods and Nanowires from Ammonia and Hydrogen Sulfide.....	64
5.2 Boron-Sulfur-Carbon Nanosheets.....	73
5.3 Amorphous Sulfur-Doped Boron Nitride Amorphous Nanoflakes.....	82

TABLE OF CONTENTS
(Continued)

Chapter	Page
6 ONE-STEP CVD SYNTHESIS OF A BNNT-IRON COMPOSITE.....	98
6.1 Introduction to Nanotube Composites.....	98
6.2 Synthesis of BNNT-Fe Composites.....	101
6.3 Results and Discussion of BNNT-Fe Composites.....	103
7 CONCLUSIONS.....	115
7.1 Review of Critical Results.....	115
7.2 Purpose of the Various Catalyst Precursors in the Reaction.....	116
7.3 Novel Growth Mechanisms and other Insights.....	117
7.4 Review of Nanoflakes and Nanofiber Heterostructures.....	118
7.5 Review of Composites.....	120
7.6 Challenges to Overcome in the IL Method and Future Experiments.....	121
REFERENCES	126
APPENDICES	
A NOVEL SYNTHESIS ROUTE OF GRAPHENE USING IRON NANOPARTICLES.....	134
A.1 Summary.....	134

TABLE OF CONTENTS
(Continued)

Chapter	Page
A.2 Introduction.....	134
A.3 Experimental Details.....	136
A.4 Results.....	140
A.5 Discussion.....	150
A.6 Conclusions.....	154
B RAPID SYNTHESIS AND CHARACTERIZATION OF AMORPHOUS MnO _x NANOWIRES/NANOFIBERS AT ROOM TEMPERATURE.....	155
B.1 Summary.....	155
B.2 Introduction.....	155
B.3 Experimental Details.....	156
B.4 Results and Discussion.....	158
APPENDIX REFERENCES	165

LIST OF TABLES

Table	Page
1.1 Strength and Fracture Toughness of G18 Glass and Composite Reinforced With 4 wt% BNNTs [29].....	15
5.1 Summary of the Experiments Attempted in this Section. Only when Sulfur is Added to the Reaction is There a Truly Exciting Product.....	97
6.1 Hardness of Pellets with Varying Amounts of Catalyst.....	106
6.2 Hardness of Gas-Treated Pellets.....	106
6.3 Ultrasound Measurements from 0% Catalyst and 100% Catalyst Pellets. The Density is in g/cc, the Velocity is in mm/ μ m, the Bulk Modulus is in GPa, and the Specific Modulus is in kN•m/kg.....	107
6.4 Mechanical Properties Obtained from the Stress-Strain Curve.....	109
6.5 Spacings Observed from Electron Diffraction Pattern and Phase Assignments....	113
7.1 Summary of the Results of this Dissertation.....	124
A.1 Table Detailing which Experimental Runs were Performed.....	139
A.2 Table Summarizing Results of Raman Intensity Ratios for the Samples in the Study. ‘Not Available’ Indicates no Graphene was Grown. Sample F Seemed to be the Highest Quality Material Available. D/G Ratio Could be an Indication of the Amount of Defects in the Graphene, and G/2D Ratio Could be an Indication of the Number Layers.....	147
B.1 ICP analysis for Product of Reaction Before and After Calcining at 500° C.....	159

LIST OF FIGURES

Figure	Page
1.1 (Top) Schematic diagram of the CVD system used in these experiments. (Bottom) A photograph of the experimental apparatus.....	3
1.2 Structural schematics and representative transmission electron microscopy (TEM) images of uniform single-crystal semiconductor NWs, axial NW heterostructures, and radial (core/shell, core/multi-shell) NW heterostructures. Scale bars are all 10 nm [10].....	7
1.3 Schematic diagrams showing that hexagonal boron nitride (left [11]) is isostructural with graphite (right [12]).....	9
1.4 TEM images and corresponding EDX data for BNNTs synthesized using FeB catalyst in a CVD process.....	11
1.5 TEM images of BNNTs grown without using metal catalyst showing large bulbous tips. A schematic of the growth mechanism is also included.....	13
1.6 Weibull strength distribution of G18 glass reinforced with 4 wt% BNNTs. The Weibull data for G18 glass are also included for comparison [29].....	15
1.7 Comparison of h-BN and graphene membranes. a.) h-BN membrane and b.) single-layer graphene membrane HRTEM images. Note that the h-BN only has monovacancies but graphene shows reconstructed vacancies [37].....	18
1.8 a.) Fresnel projection microscope images a.) before and b.) after transport measurements. The current-voltage curves are shown in c.) where the solid curve is the first sweep, the dashed curve is the second sweep, and the dotted curve is the third sweep. These curves are that of a semiconductor with an estimated band gap below 1 eV [44].....	19
1.9 (Left) Room temperature PL spectra from BCNNTs. As one goes from a-e the concentration of C decreases. (Right) Attempt to match reproducibility of d from left images. Note that even when growth conditions are held supposedly constant there is some variation in PL intensity, though the frequency remains unchanged [45].....	20
1.10 Layout of experimental setup used to measure electrical properties of individual tubes with AFM. Current-voltage curve of b.) BCNNT/CNT junction, c.) individual CNT and d.) individual BCNNT [46].....	21

LIST OF FIGURES
(Continued)

Figure	Page
1.11 BCN nanojunctions grown from split nickel particles: a.) TEM image of a heterojunction showing deactivated catalyst. b.) SEM of three nanotubes grown from tip of a single nanotube. c.) Close-up image of Y-shaped nanojunction [47].....	21
2.1 (a) Fixed-bed technique: (1) furnace, (2) thermocouple, (3) carrier gas, (4) reactant and carrier gases, (5) catalyst/solid reactant (if needed), (6) outlet [49]...	24
2.2 Illustration of the VLS method which is used to grow a nanorod. This is the presumed method of growth for the nanomaterials to be discussed in this work [50].....	24
2.3 High (top) and low (bottom) temperature CVD systems used in this study.....	25
2.4 Schematic showing the set up of an SEM [51].....	27
2.5 An electron which impacts an inner shell electron will scatter inelastically and will cause the impacted electron to eject [52]. When another electron drops into the place of the now missing electron, either an X-Ray photon is given off at a characteristic energy level, or an outer electron is ejected (Auger Emission). Energy dispersive X-ray (EDX) emission spectroscopy is used for chemical analyses in this dissertation.....	28
2.6 Schematic of a TEM operating in the imaging mode (left) vs. diffraction mode (right). The instrumental set up is the same but the electron beam in each is focused differently [53].....	32
2.7 Schematic illustration of the Ewald sphere. The points which are intersected by the circle cut out from the Ewald sphere will diffract because they satisfy the Bragg condition [54].....	32
2.8 (Left) Illustration depicting how an incident electron loses energy when striking an inner shell electron in a sample. (Right) Binding energy vs. atomic number, Z, plots showing variation of the binding energies in each electronic shell as a function of Z [56].....	34
2.9 Raman effect vs. Rayleigh scattering. Note that in Rayleigh scattering the scattered light has the same wavelength as the incident laser radiation, but in Raman scattering there is a vibrational frequency-dependent shift in wavelength either to higher values (anti-Stokes) or to lower values (Stokes) [57].....	36

LIST OF FIGURES
(Continued)

Figure	Page
2.10 Stokes, anti-Stokes, and Rayleigh lines. Note that in Rayleigh scattering the electron goes from the ground state to the virtual state and back to the ground state without interacting with the vibrational levels [58].....	37
2.11 Schematic depiction of Raman Spectroscopy [59]. Inelastically scattered light from a sample after it has been irradiated by a laser beam. A filter removes Rayleigh light, and a spectrometer is used to disperse the Raman light onto a detector, where the intensity vs. frequency of the light is recorded.....	37
2.12 Schematic of a 4-point probe measurement. Note the current flow through terminals a and d and the voltage drop between b and c [60].....	39
2.13 (Left) SEM image of 50 nm thick boron nanowire with leads drawn onto it. (Right) Overlay drawn onto entire doped silicon chip. Six separate nanomaterials can be tested with this one chip if they are placed on the red center grid.....	39
3.1 (Left) SEM image of numerous boron-carbon nanowires protruding from surface of particle. (Right) High magnification image of nanowire, clearly showing the nanowires are not completely straight and have a bulbous tip from the catalyst.....	45
3.2 (Left) TEM image of core boron-carbon nanowires growing out of catalyst. (Right) High magnification TEM image of the nanowires.....	46
3.3 (Left) Very high resolution TEM image of catalyst particle in boron-carbon nanowire. Note the outside of the nanowire appears to be of a different structure than the interior of the nanowire. The outer part of the nanowire is the material which encapsulates the catalyst. (Right) FFT of the outside of the nanowire, which showed spacings of approximately 0.36 to 0.39 nm, size of box is 12.65 nm X 12.65 nm. (Bottom) Profile plot of outside of nanowire, confirming results from FFT analysis.....	46
3.4 (Top Left) High resolution TEM image of boron-carbon nanowire. FFT was performed on the interior of the nanowire with labeled spacings and directions. (Top Right) Raw FFT of interior of nanowire, note that 6 different spacings are evident, size of box is 25.63 nm X 25.63 nm. (Bottom Left) Masked image of FFT with labeled points, making analysis easier. The following were measured using the ImageJ software suit, EC=DC=.48, AC=.44 to .45, BC=0.38, $\angle ACB=46.9^\circ$, $\angle BCD=54.6^\circ$, $\angle ACE=77.7^\circ$. (Bottom Right) Another profile of the outside of the nanowire, this confirms the results from Figure 3.3.....	47

LIST OF FIGURES
(Continued)

Figure	Page
3.5 (Top Left) Another high resolution image of a boron-carbon nanowire. (Top Right) FFT analysis of the outer walls, again showing a spacing of approximately 0.36 nm to 0.39 nm, size of box is 12.75X12.75 nm. This shows the spacing of the material around the catalyst is the same as the material which goes along the outside of the nanowire. (Bottom) Profile plot of the outside of the nanowire, confirming previous results.....	48
3.6 (Left) Boron EELS image and (Right) Carbon EELS Image. Note the boron is in the inside of the nanowire and the carbon is on the outside of the nanowire, including the catalyst head. The nanowire moved during analysis which is causing the raster scan distortion.....	48
4.1 Desired theoretical nanoheterostructure, where black represents boron and green represents boron nitride. This could be a nanowire or nanotube heterostructure.	51
4.2 SEM images of nanowires which result from intermittent ammonia doping using the IL method with MgB ₂	52
4.3 (Left) TEM image of a long nanowire from IL method with intermittent ammonia addition and MgB ₂ . Note that there seems to be periodic contrast in the structure of the nanowire. (Right) Same nanostructure except at high magnification. Note the nanowire appears to be composed of two different structures, the interior is amorphous and the exterior is layered, like a nanotube.	53
4.4 EELS mapping image of nanowire which results from MgB ₂ and intermittent ammonia doping, with (left) showing nitrogen and (right) showing magnesium. This image also includes the catalyst at the head of the nanowire. The nitrogen is always found with boron and the magnesium is always found with oxygen in these nanowires.....	53
4.5 (Left) SEM image of nanowires which result from using intermittent doping of ammonia with the IL method using Mg(BH ₄) ₂ . (Right) High magnification SEM image of same structure, showing some nanowires have interesting discontinuities which may result from intermittent doping.....	54
4.6 (Left) TEM Image of nanowire which results from intermittent doping of ammonia using the IL method with Mg(BH ₄) ₂ . Note that the nanowires seem to long and thin, with diameters ranging from 10 nm to 40 nm, and lengths in the microns. (Right) High magnification TEM image of the nanowires showing that discontinuities in the material occur often. This might be due to the partial doping.....	55

LIST OF FIGURES
(Continued)

Figure	Page
4.7 (Top) STEM image of representative nanowires from intermittent doping of ammonia using the IL method with $\text{Mg}(\text{BH}_4)_2$. (Middle) EELS map of boron and (Bottom) nitrogen. These nanowires seemed to have discontinuities which may have resulted from intermittent doping but the nitrogen is evenly distributed in the nanowire.....	56
4.8 (Top Left) TEM image of relatively rare nanowire found in the product of the IL method using intermittent doping of ammonia with $\text{Mg}(\text{BH}_4)_2$. (Top Right and Bottom) STEM images of same nanowire showing where EELS analysis was performed. All EELS analysis indicate the material is pure boron.....	57
4.9 (Top Left) TEM image of a very rare nanowire with obvious discontinuity. (Top Right) STEM image of same nanowire, showing damage from where EELS analysis was performed. (Middle) Nitrogen EELS map of nanowire, note that it is not continuous through the material. (Bottom) Boron EELS map of nanowire, note that unlike nitrogen boron is found through the entire nanowire.....	58
4.10 Low magnification SEM image of nanowires made through methane and ammonia addition to the IL method. (Right) Higher magnification image of the same.....	59
4.11 TEM images of bundles of nanostructures encased in amorphous carbon.....	60
4.12 TEM images of the nanotubes which result from altering the IL method by doping with methane and ammonia gas and using MgB_2 . The nanotubes are only a few layered, ranging from 4-10 layers, and commensurately have diameters ranging from 10 nm to 20 nm. In this case, there is no magnesium filling. Catalyst particles can be seen on the inside of some of the nanotubes, but they're clearly not filled completely with any material.....	61
5.1 (Left) Low magnification SEM image of the result of adding ammonia and hydrogen sulfide to the IL method with MgB_2 . Note that relatively thick nanorods appear to cover the sample. (Right) High magnification SEM image of the same showing the nanorods have diameters of roughly 100 nm and lengths in the microns. A thick catalyst head is visible at the tip of each of the nanostructures.....	65
5.2 SEM image of the product which results when adding ammonia and hydrogen sulfide to the IL method with $\text{Mg}(\text{BH}_4)_2$. Long thin nanowires are growing from the sample at a moderate yield.....	65

LIST OF FIGURES
(Continued)

Figure	Page
<p>5.3 (Top left) Low resolution TEM image of a nanorod which results from the IL variation using MgB₂ with the addition of hydrogen sulfide and ammonia. Note that the nanorod is thick and short compared with other nanostructures discussed in this dissertation and has a number of ‘kinks.’ (Top right) Typical HRTEM image of the nanorods, the ‘kinks’ make in depth analysis difficult.....</p>	66
<p>5.4 (Top left) HRTEM image of a particularly crystalline area of the sample, here crystal spacings of 0.60 nm and 1 nm were measured (contrast plots used for the measurement are given in Figure 5.5). This part of the sample may not be representative because it was difficult to find, however analysis on it was the most reliable because of the high resolution possible. (Top right) FFT of the highly crystalline area, used to confirm measurements of crystal spacings. A masked image is given in Figure 5.5 where spacings are easier to interpret. (Bottom) CBED of the sample, spacings are difficult to measure, but this does show the sample is kinked heavily.....</p>	68
<p>5.5 (Top) Masked FFT image based on FFT image from Figure 5.4. Spacings of 0.55, 1, and 0.60 nm are shown, which are measured from the point to the center in the image. Note that $\angle DCB = 33^\circ$ and $\angle BCA = 48^\circ$. (Middle) Contrast profile plot confirming 0.60 nm crystal spacing. (Bottom) Contrast profile plot going in nearly perpendicular direction to previous profile, showing crystal spacing of 1 nm.....</p>	69
<p>5.6 (Top left) TEM image of a long thin nanowire, note that it has a long aspect ratio and appears undamaged. (Top right) HRTEM image of same nanowire, it is 20 nm in diameter and possesses a highly ordered crystal structure. The direction and size of the crystal spacings calculated from the FFT analysis given in Figure 5.7 are displayed. (Bottom left) CBED and (Bottom right) SAD pattern of same nanowire, used to confirm the crystal spacings.....</p>	70
<p>5.7 (Left) FFT image of HRTEM found Figure 5.6. (Right) Masked FFT image for ease of analysis. The corresponding crystal spacings are given and $\angle BCD = 35^\circ$ and $\angle ACD = 55^\circ$.....</p>	71
<p>5.8 SEM images of the product which results when adding methane and hydrogen sulfide to the IL method with MgB₂. (Top left) Dramatic example of the stacking which occurs with this material. (Top right) The sheets could sometimes stack in a pyramiding fashion. (Bottom left) High magnification image of stacking sheets. (Bottom right) Folds evident in the sheets.....</p>	74
<p>5.9 TEM images of the amorphous flakes which result from adding hydrogen sulfide and methane to the IL method using MgB₂.....</p>	75

LIST OF FIGURES
(Continued)

Figure	Page
5.10 Optical images of the stacked sheets: (Left) transmission mode (Right) reflective mode, and (Bottom) normal.....	76
5.11 (Top) Raman and (Bottom) FTIR spectra of the amorphous sheets which result.	77
5.12 (Top left and right) Low and high magnification (respectively) images of nanostructures which result from the IL method using MgB_2 with no MCM-41. They appear to be some sort of nanofiber with a distorted morphology. (Bottom) Nanostructures found in product of IL method using $Mg(BH_4)_2$ with methane and hydrogen sulfide.....	78
5.13 Raman spectra of the products which result when performing the IL experiment with MgB_2 (no MCM-41) and $Mg(BH_4)_2$ with flowing methane (20 sccm) and hydrogen sulfide (10 sccm). They both appear to be MWCNTs with a moderate amount of defects.....	80
5.14 (Top) Model of the CVD set up used for these experiments. (Bottom) Picture of CVD set up used for the high temperature reactions needed for the doping of BNNTs. A carbon crucible was heated with an Ameritherm Induction heater. The crucible was sheathed in layers of yttria stabilized zirconia felt and was held up by a porous disk of quartz. The entire reaction chamber was made of quartz.....	84
5.15 SEM images of the material found in the carbon crucible when trying to recreate the original conditions described in literature. The material appears to be thick nanorods, 100 nm to 500 nm in diameter and microns in length.....	85
5.16 SEM images of the material found on the sidewalls of the reaction vessel. The thin fibrous material was presumed to be boron nitride nanotubes.....	85
5.17 (Left) SEM image of possible nanostructure which resulted from manganese doping of BNNTs. The material appears to be a damaged nanostructure. (Right) SEM image showing the results of the carbon doping experiment, where methane was added. The result seemed similar to product obtained from simply repeating the literature process. The thin fibrous material could be some sort of doped nanotube, but this could not be confirmed.....	86

LIST OF FIGURES
(Continued)

Figure	Page
5.18 (Left) SEM image of result from adding ammonia to the original literature process used to grow BNNTs. These nanotubes did not have excess nitrogen as hoped, but the addition of ammonia did increase the yield and quality of the BNNTs dramatically. The nanotubes are roughly 10 nm in diameter and microns in length. The thin fibrous nature is similar to the material found with no doping, but in the case of the addition of ammonia, the material is much more abundant. (Right) TEM image confirming these structures are nanotubes.....	87
5.19 (Top left and right) Nanorods found in the sulfur doping experiment. The rods appear to be 100 nm to 500 nm in diameter and several microns in length. (Bottom left) Nanowires found in the product of the sulfur doping experiment. The nanowires are roughly 20 nm in diameter and have large aspect ratios. These were difficult to find in the sample. (Bottom right) Interesting branching nanoribbon, an extremely rare find in the sample. It is most likely two-dimensional in shape, though it could be a branched nanowire. Each ‘branch’ seems to be 10 nm wide with a distance of 50-100 nm between each branch. The branches have a large aspect ratio.....	90
5.20 (Top left) Nanorods scattered about the TEM grid, confirming results from SEM analysis. (Top right) Nanoplatelets that were found throughout the entire sample. (Bottom left) Nanoplatelets flaked from a nanorod. (Bottom right) High magnification image of flakes stacked on top of each other.....	91
5.21 (Left) Fast Fourier transform of flakes indicating amorphous structure. (Right) Small area electron diffraction of flakes confirming amorphous structure.....	93
5.22 Raman signal of the experimental run with sulfur vs. boron nitride nanotubes. Note that the 1369 cm^{-1} is completely eliminated and there is a very small amount of Raman activity near $1124\text{-}1138\text{ cm}^{-1}$. This small peak is repeatable and was confirmed through independent analysis using another Raman instrument. For convenience and better analysis, the small area in the dashed box was plotted separately in Figure 5.23.....	94
5.23 Much closer look at the Raman spectrum identified in the product of the S doped experimental run, clearly showing a very small doublet peak.....	95
6.1 Optical images at 500X of: (Left) A pellet before CVD reaction, and (Right) after CVD reaction.....	103
6.2 Specific stress-strain curves of Fe-BNNT composite (black) and pure Fe (blue).	109
6.3 SEM images of: (Left) The surface of a BNNT-iron composite pellet, and (Right) interior of a cracked BNNT-iron composite pellet.....	111

LIST OF FIGURES
(Continued)

Figure	Page
6.4 SEM images of: (Left) Interior of a cracked BNNT-Fe pellet showing BNNTs bridging from particle to particle, and (Right) a closer view of two particles joined by BNNTs.....	112
6.5 SEM images showing: (Left) overview of BNNT-Fe composite with multitude of BNNTs, and (Right) Closer view of two iron particles bridged by a stretched BNNT bundle in the composite.....	112
6.6 (Left)TEM image of a multiwall BNNT with ten walls joining two iron particles in the BNNT-Fe composite; and (b) selected area electron diffraction taken from the BNNT-Fe composite. The spacings and assignments of the different phases in the composite are given in Table 5.....	113
7.1 An example of an atomically thin, complicated device possible through the IL method.....	119
7.2 Nanowire of sections of material which could be created through the IL method. Graphene could easily be joined with CNTs.....	120
7.3 Graphene joined to a boron nanowire covered in a CNT. This structure could have interesting electrical properties as well. Morphologically, a boron nitride sheet could form around a boron nitride covered MgO nanowire in the same manner.....	120
A.1 (Top Left) 20 nm iron purchased from American Elements. (Top Right) 100 nm iron purchased from same source. (Bottom) Diagram of chemical vapor deposition set up used in experiments.....	138
A.2 (Left) Raman spectrum of Sample A, x units in cm^{-1} and y axis is intensity. (Right) Graphene growing on catalyst in Sample A.....	141
A.3 Raman of Sample B, x units in cm^{-1} and y axis is intensity. (Top Right) SEM image of Sample B, showing a number of nanotubes populating an area. (Bottom) Nanotubes and graphene covering a large area of Sample B.....	141
A.4 Raman Spectrum of Sample C, x units in cm^{-1} and y axis is intensity. (Top Right) Raman Spectrum of Sample D. (Bottom Left) Raman Spectrum of Sample E. (Bottom Right) Raman Spectrum of Sample H.....	143

LIST OF FIGURES
(Continued)

Figure	Page
<p>A.5 (Top Left) Raman spectra from Sample F, x units in cm^{-1} and y axis is intensity, this is the highest quality graphene made in the study. (Top Right) SEM image of Sample F, note the growth of a large number of graphene sheets on the surface of the particles. (Bottom) Zoomed in image showing an area with a particularly dense concentration of graphene sheets.....</p>	145
<p>A.6 (Top Left) Raman spectrum of Sample G, x units in cm^{-1} and y axis is intensity. (Top Right) SEM image of product of Sample G placed on TEM grid, note that it is so thin that the grid can easily be seen underneath. (Bottom) Large area of graphene sheets found on the TEM grid.....</p>	146
<p>A.7 (Top Left) TEM image showing clearly faceted growth, which is an indication of the growth of graphene. (Top Right) TEM image showing the catalyst-iron interface. Whether there is an actual connection, or if the iron particle is simply on top of the graphene or vice versa, is unclear. (Mid Left) STEM image of the sample. Note the contrast can be used to find the iron catalyst and also examine the relative thickness of the graphene. (Mid Right) Diffraction pattern showing 0.34 nm spacing and possible 6 fold symmetry indicative of layered carbon formation. (Bottom Left) Lower magnification TEM image of graphene growing on the 20 nm particle. (Bottom Right) Graphene growing from nanoparticles.....</p>	149
<p>A.8 (Top Left) Graphene with presumably very few layers forming a stack. (Top Right) Lower magnification TEM image of Sample G on TEM Grid. (Bottom Left) Higher magnification image showing that the graphene seems to agglomerate using the deposition methods discussed. (Bottom Right) High magnification of a particularly thin area of graphene which does not have many agglomerates.....</p>	150
<p>A.9 Presumably, the flower model is the most accurate model to describe the growth conditions. (Top) Representative iron catalyst particles before growth, analogous to free standing ‘ovules.’ While only one flat layer is shown, any number of nanoparticles could simultaneously be surrounded by carbon layers which would eventually form graphene. (Middle) Iron catalyst surrounded by graphene layers, analogous to flower bulb. (Bottom) In this part of the image, the carbon layers are opening up to form graphene, analogous to a blooming flower petal. An arbitrary location was chosen as to where the carbon layer splits to form graphene in the image, although the split could happen anywhere in the layer.....</p>	152
<p>B.1 X-ray diffraction (left panel) and Raman (right panel) of the nanowire/nanofiber samples. X-axis in degrees and cm^{-1} respectively. See text for discussion.....</p>	159

LIST OF FIGURES
(Continued)

Figure	Page
B.2 SEM images of the samples showing agglomerated nanowire/nanofiber morphologies.....	160
B.3 TEM images and electron diffraction of the H ₂ O:MnO _x nanowires/nanofibers before calcining: (Top Left) Higher resolution image of a nanowire protruding from a bundle. (Top Right) Lower magnification image of a bundle of nanowires/nanofibers. (Bottom Left) Nanowires/nanofibers after sonication showing that the sidewalls are extensively damaged. (Bottom Right) Typical selected area electron diffraction from the sample showing that the sample is largely amorphous.....	161
B.4 (Top Left) SEM of calcined nanowires. Note the nanowire morphology is still intact. (Top Right) XRD of calcined nanowires, which indicates the calcining process creates a more crystalline material. (Bottom) Raman of calcined material. Interestingly, the Raman signal is not dramatically altered through the calcining process.....	163

LIST OF SYMBOLS AND DEFINITIONS

BNNT	Boron nitride nanotube, nanostructure consisting of a rolled sheet or several nested rolled sheets of hexagonal boron nitride
CNT	Carbon nanotube, nanostructure consisting of a rolled sheet or several nested rolled sheets of graphene
CVD	Chemical vapor deposition, process commonly used to create nanomaterials, involves the use of a nanostructured catalyst with a variety of reactant gases
Graphene	A single, atomically thin layer of graphite
Nanofiber	Category of nanomaterials containing nanotubes, nanowires, and nanorods, frequently found in bundles in samples
Nanoheterostructure	Two nanomaterials joined to one another in the nanoscale
Nanomaterial	A material which has some or all dimensions restricted to <100 nm
Nanoparticle	A nanomaterial with three dimensions <100 nm
Nanoplatelet	A nanomaterial with one dimension <100 nm, also referred to as a nanoflake
Nanorod	A short, thick nanowire
Nanowire	A nanomaterial with two dimensions <100 nm
Raman Spectroscopy	Spectroscopic technique based on the inelastic scattering of photons
SEM	Scanning electron microscopy, high resolution imaging technique based on the scattering of electrons from a sample
TEM	Transmission electron microscopy, high resolution imaging technique based on the transmission of electrons through a thin sample

CHAPTER 1

INTRODUCTION

1.1 The IL Method

The goal of the research performed in this dissertation is to create novel nanomaterials and characterize them. Nanomaterials frequently exhibit a number of useful properties for industrial applications. A method was found which is amenable to the creation of a number of different nanomaterials. A process previously utilized to make pure boron nanostructures can also synthesize a number of other nanomaterials through the addition of different reactant gases to the method. The addition of methane, hydrogen sulfide, and ammonia to the process produced an entire family of nanomaterials. These materials could presumably be integrated with other known nanostructures to form a variety of novel devices. Composite materials of these new nanostructures could also be formed by depositing them onto a matrix material. This project will study some of the possible novel nanomaterials and devices, and methods to create nanocomposites using the same materials. The dissertation will also evaluate the potential for device fabrication by creating new materials and measuring their electrical properties.

The synthesis of nanostructures has been a field of significant research and industrial value. Nanostructures have been shown to have important advantages in comparison to their bulk analogs. Therefore, the synthesis of new nanomaterials will present exciting opportunities for research which may also have some practical value. While there are many methods available to synthesize nanomaterials, the preferred method for this project is chemical vapor deposition (CVD). CVD processes are relatively simple to implement, scalable, and are very flexible in terms of processing

parameters. CVD methods are able to create numerous interesting nanostructures, and the aim of this research is to create and characterize novel materials of this type.

A process which seemed to have high potential to form nanomaterials is one used originally to grow pure boron-based nanostructures [1]. This method is a purely solid-solid reaction performed in an inert flowing gas atmosphere at high temperatures, making it a thermal vapor deposition process. First, the following is crushed together using a mortar and pestle: 50 wt% MgB_2 (Alfa Aesar Company) powder, 30 wt% nano-NiB (synthesized in a manner following [2]) and 20 wt% of mesostructured hexagonal framework MCM-41 zeolite (Sigma Aldrich) powder. Typically, 0.02 – 0.1 gms of mixture are added and grinded in an agate mortar for about an hour manually to ensure that the powder is well mixed. This material is then ground further for several hours using a rotary mixer which uses cylindrical ceramic pieces as a milling media. Finally, the mixture is loaded into the quartz reactor of the CVD set up shown in Figure 1.1.

The quartz tube is pumped down to 10^{-3} torr and heated to $950\text{ }^\circ\text{C}$ at a rate of $10\text{ }^\circ\text{C}/\text{min}$ under flowing argon at 100 sccm (standard cubic centimeters per minute). The temperature is held at $950\text{ }^\circ\text{C}$ for 60 minutes. After completion of the reaction, the furnace is switched off and the reaction tube is allowed to cool down to room temperature under flowing argon. Alternatively, one can use $\text{Mg}(\text{BH}_4)_2$ instead of MgB_2 , but then the optimal reaction temperature is 800°C . The use of $\text{Mg}(\text{BH}_4)_2$ generally results in structures different than what is obtained using MgB_2 , most likely because of the presence of hydrogen radicals in the reaction. Figure 1.1 shows the CVD oven used for the experimentation.

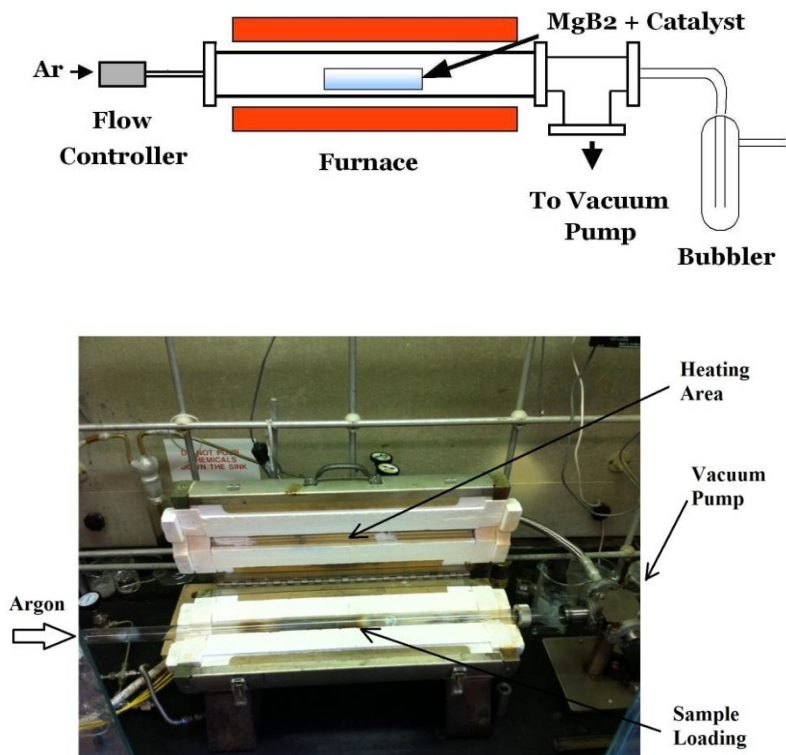


Figure 1.1 (Top) Schematic diagram of the CVD system used in these experiments. (Bottom) A photograph of the experimental apparatus.

This method referred to here as the Iqbal-Liu method has been successful in synthesizing novel boron-based nanostructures, which will be discussed in soon to be published work [Patel et al., to be published]. Since the IL process was initially developed without the use of any reaction gases, an interesting variation was the use of different reactive gases which could result in even more new structures. The most obvious choice for a reaction gas was ammonia, because nitrogen reacts readily with boron, and boron nitride itself can form a number of interesting nanostructures. The next choice was methane, because it would add carbon to the nanostructures formed. Carbon, among all elements, has the most accommodating chemistry for the formation of nanomaterials, and will typically form carbides with boron. The last choice made for a

reactive gas was hydrogen sulfide, because sulfur is electron rich and will readily react with electron-deficient boron atoms to form stable nanostructures. A number of variations of the IL method have been attempted resulting in novel nanostructures which will be discussed in this dissertation.

An alternative method to create novel nanostructures resulted in materials similar to those prepared using the IL method, see [Section 5.3](#). The ability to create nanocomposites is also of great interest, since current techniques do not provide composites with the best possible properties. A novel chemical vapor infiltration technique greatly simplified the methods used to create nanocomposites, see [Section 6](#). This process was used with more mature synthesis methods and materials, but could easily be applied to the nanomaterials synthesized using the IL process. The results described in Appendix A and B, though not directly related to this dissertation, are included because the work came about because of the research discussed here. To understand the significance of the materials produce by the IL method, a short review of prior work on related nanomaterials, such as graphene and its boron nitride analog, is also given.

1.2 Nanowires

Nanowires (NWs) are one-dimensional, highly anisotropic structures which, due to their unique aspect ratios, can have enhanced material properties in comparison to their bulk analogs. Due to problems with semantics, some time will be taken to discuss the difference between nanorods, nanowires, and nanotubes (all of which will be considered to fall into the category of nanofibers). All are one-dimensional structures, and are difficult to differentiate using a scanning electron microscope. Nanotubes are hollow

cylinders formed by rolled flat sheets with no bonding between walls. This implies that typically, only materials with a layered crystal structure, such as that of graphite, will form nanotubes. Nanowires, as the term suggests, are fully dense and not hollow. Electron transport, therefore, occurs through the bulk of a nanowire and only along the walls in nanotubes. Although sometimes incorrectly referred to as nanowires, nanotubes are not nanowires. Nanowires essentially retain the three-dimensional crystal structure of the corresponding bulk solid and rarely grow to diameters as small as 10 nm. Nanotubes, on the other hand, can be grown to a diameter as small as 0.5 nm and can be nested to form multiwalled architectures. Carbon nanotubes do not have a three-dimensional crystal structure and are held together through conjugated carbon-carbon network bonding. In multiwalled carbon nanotubes, however, the individual concentric walls are held together by non-covalent π - π stacking interactions similar to that of the layers in graphite. Nanorods tend to refer to materials which are long and elongated, but with diameters larger than nanowires and much less anisotropy (with aspect ratios of 1-10 as opposed to >100 as seen in nanowires) [7]. Nanowires will be the focus of this section, as by comparison nanorods are typically not unique in relation to their bulk analogs and nanotubes are discussed at great length later in this dissertation. Nanowires can be synthesized using a variety of ‘bottom up’ techniques, but for this discussion chemical vapor deposition (CVD) is the most important. CVD methods are extremely flexible (see [Section 2.1](#)) and amenable to integration with modern electronic systems.

Nanowires offer some advantages in comparison to their bulk analogs:

- They are usually stronger. This is driven by Hall-Petch mechanics and makes them useful for structural applications [8]. This strengthening effect is usually only seen in nanowires with diameters below a critical size determined by the chemistry of the nanomaterial [9].

- Nanowires have an unusual fiber-like morphology, significantly affecting practical application. For example, their unique structure allows them to form fiber reinforced composites. This is extremely practical as fiber reinforced composites fail differently compared with traditional materials. This results in stronger and more reliable structural materials. Another practical benefit of the one-dimensional morphology of nanowires is their ability to be used in electronic devices and only consume space in one direction. This property will allow for more compact, and therefore, faster and more efficient electronic devices.
- If the nanowires' diameters approach dimensions smaller than the Bohr radius of an electron-hole pair, typically below 20 nm, quantum confinement of electronic and vibrational (phonon) states can occur resulting in novel electronic and vibrational properties similar to those observed in quantum dots. (Confinement is dependent on the material and the wavelength of the conduction carriers, for semi conductors this can be as large as a micron and as small as 0.5 nm.)

1.3 Nanowire Heterostructures

Nanowires of different types can be combined together into one structure, which allows for the creation of a multitude of novel heterostructures. Nanowire heterostructures will be defined as a nanowire composed of several types of crystal structures or elemental compositions. This heterostructure allows for the creation of an entire device onto one nanowire, which can have exciting properties that may be exploitable for electronic applications. For example, one could form a silicon nanowire with one part which is p-doped and one part which is n-doped, creating a diode. If alternating p- and n- doped sections are placed in a nanowire, the nanowire would function as a transistor. These nanowire heterostructures will be nanoscale devices which can have many advantages over traditional, bulk electronic devices. Another exciting possibility is that since these devices are at the nanoscale, novel quantum scale effects, such as electron and phonon localization may occur. This would allow the formation of an entirely new generation of devices, not simply incremental improvements over older technology. One can consider

two types of nanowire heterostructures, axial (different sections along the wire axis), and radial (a core shell type heterostructure where the core and the shell are different materials) as shown in Figure 1.2 [10]. Using these heterostructures, nearly any device which can be fabricated in the macro-scale can be produced at the nano-scale on one nanowire, allowing for a number of significant improvements in efficiency and speed (following on Moore's Law).

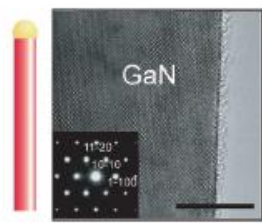
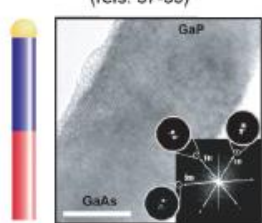
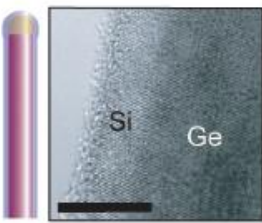
	Group IV	Group III/V	Group II/VI
Homogeneous Structure (refs. 18, 21-36) 	Si Si:B (p-type) Si:P (n-type) Ge Ge:B (p-type) Ge:P (n-type) $\text{Si}_x\text{Ge}_{1-x}$	GaN GaN:Mg (p-type) GaN:Si (n-type) GaN:Mn GaP InP InP:Zn (p-type) InP:Te (n-type) GaAs InAs $\text{GaAs}_y\text{P}_{1-y}$ $\text{InAs}_y\text{P}_{1-y}$	ZnS ZnS:Mn CdS CdS:Mn ZnSe CdSe
Axial Heterostructure (refs. 37-39) 	n-Si/p-Si n-Si/i-Si/p-Si $(\text{n-Si/n-Si})_n$ Si/NiSi	$(\text{GaAs/GaP})_n$ n-InP/p-InP	
Radial Heterostructure (refs. 40-46) 	i-Si/p-Si Si/Ge Ge/Si Si/SiO ₂ Si/Ge/Si i-Si/SiO ₂ /p-Si p-Si/i-Ge/ SiO ₂ /p-Ge	n-GaN/InGaN/p-GaN n-GaN/InGaN/ p-AlGaIn/p-GaN n-GaN/(InGaN MQW) /p-AlGaIn/p-GaN GaN/AlN/AlGaIn	CdS/CdSe Si/CdS

Figure 1.2 Structural schematics and representative transmission electron microscopy (TEM) images of uniform single-crystal semiconductor NWs, axial NW heterostructures, and radial (core/shell, core/multi-shell) NW heterostructures. Scale bars are all 10 nm [10].

Nanowire heterostructures could form nearly any electronic device, such as transistors and photodiodes. Since effects due to quantum confinement in devices are currently not completely understood, nanowire transistors may have surprising characteristics in comparison to their bulk analogs. The IL method and its variations can synthesize a number of nanowires and nanowire heterostructures. These materials can be integrated by altering the growth conditions of the IL method, creating the heterostructures *in situ* and synthesizing structures for a whole host of new devices. Even more exciting than nanowires are nanotubes, which exhibit even greater size and property differences in comparison to their bulk analogs than nanowires do.

1.4 Nanotubes

Nanotubes of different elements and compounds have elicited enormous attention because of their remarkable electrical and mechanical properties; however, the bulk of this research has been conducted on *carbon* nanotubes (CNT). Carbon can form nanotubes because of its graphitic crystal structure from which graphene layers can be extracted and rolled up. Logically, other elements or compounds which have a layered hexagonal crystal structure should be able to form nanotubes as well; presumably with a change in properties as dramatic as going from graphitic carbon to CNTs. Boron nitride is one of the few materials which can also form flat graphitic layers which implies it can make a variety of nanostructures like carbon. Indeed, boron nitride can form boron nitride nanotubes (BNNTs), which have a number of remarkable properties. Boron nitride in its hexagonal form, commonly abbreviated h-BN, is analogous to graphitic carbon. This is readily apparent in Figure 1.3, where h-BN can be compared to graphite.

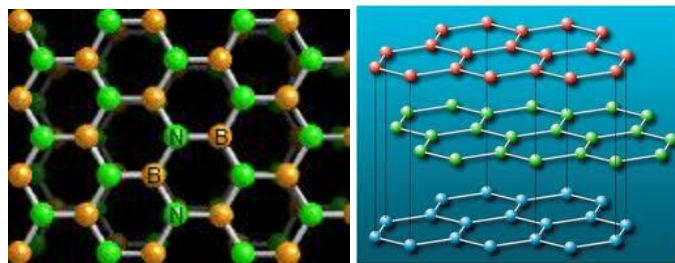


Figure 1.3 Schematic diagrams showing that hexagonal boron nitride (left [11]) is isostructural with graphite (right [12]).

Carbon, in both its graphitic and diamond allotrope, has had a tremendous impact on technology. The discovery of a third allotrope of carbon, C_{60} -fullerene, in 1985, created a new branch of materials science and chemistry. This was followed by the discovered of carbon nanotubes and graphene, which has led to a revolution in nanotechnology. Amazingly, boron nitride is capable of forming just as many allotropes; all isostructural with their carbon analogs. This is because the electron deficiency of boron is compensated by the high electron content of nitrogen. For example, the similarities between BNNTs and CNTs are remarkable considering that BNNTs are nanotubes of a compound whereas CNTs are those of a single element. Indeed, they are difficult to differentiate in mid-level resolution TEM image electron microscopy images and possess similar atomic arrangements. While they may look similar, there are key differences between the two materials. The first and perhaps most important is the character of their bonds. CNTs are entirely conjugated C-C bonds, while BNNTs' bonds are a mix of covalent and ionic bonding. These bonds, combined with the obvious elemental disparity in their compositions, accounts for the difference between the properties of the two seemingly identical materials. The IL method and its variations can create boron nitride, carbon and boron nanotubes. (Boron nanotubes are extremely fascinating because pure boron does not have a graphitic structure because of the electron

deficiency of boron; however, graphene-like sheets of boron have been theoretically predicted to be thermodynamically stable and may form transiently to create boron nanotubes.) While the IL method was successful in creating a variety of other nanotubes, other CVD techniques to create BNNTs should be examined because they possess relevance for the work in this dissertation.

High quality BNNTs were synthesized with a rather straight-forward process involving the use of iron boride (FeB) [13]. Nano-FeB was synthesized through the addition of iron sulfate (FeSO_4) to potassium borohydride (KBH_4) with both in solution. (A similar method was used to produce the NiB catalyst used in the IL method.) This process is well known and has been characterized extensively [14-17]. The iron boride was placed in an oven and heated to 1100°C in an argon atmosphere. The argon flow was shut off and the material was exposed to a mixture of ammonia gas and nitrogen. The result of this reaction was a mixture of BN and left over catalyst. The catalyst was washed away with HCl leaving behind mostly BNNTs. The BNNTs produced had lengths up to many micrometers and diameters that were about 20 nm. These BNNTs were characterized using a TEM, as shown in Figure 1.4. This method was modified to synthesize an iron-BNNT composite, as discussed in [Chapter 6](#).

The synthesis processes for BNNTs presented previously are not optimal for all situations. In any case where residual metal catalyst will interfere with measurements, for example in magnetic studies, the aforementioned methods would be problematic. Ridding a sample of metal catalyst is impossible; it is difficult to wash when on the outside of the BNNTs, and the metal in the BNNTs will never be removed. For certain

experiments therefore, a method which does not use any metal catalysts at all would be desirable.

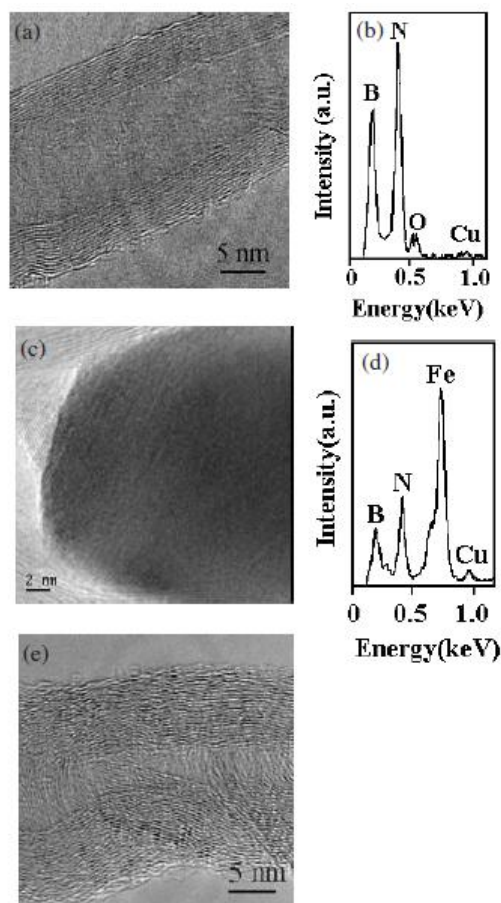


Figure 1.4 TEM images and corresponding EDX data for BNNTs synthesized using FeB catalyst in a CVD process.

A CVD synthesis method of producing BNNTs without the use of catalysts has been reported [18]. First, melamine diborate was prepared as a white powder by cooling a hot aqueous solution of melamine and boric acid. This material was then calcined in air at 500° C and then annealed in nitrogen at 800° C. This material was then placed in an oven which was rapidly heated to 1700° C with a N₂ gas stream. During the reaction, the material evaporates and deposits on the sidewall of the oven. This product is boron

nitride nanotubes, with diameters ranging from 5-20 nm and length in microns. The most striking feature of these nanotubes seems to be the bulbous tips. The bulbous tips are an amorphous B-N-O mixture. BNNTs cannot have neat caps with the pentagonal formation because there would by necessity be N-N or B-B bonds. Thus, even in the case where a metal catalyst is not used, some sort of material must act as a growth starting point. This method requires tremendous temperatures and can be dangerous. The yields of this process can also be low, and the bulbous tips may be undesirable. However, this method does allow a way to grow BNNTs without using metal catalyst, making it ideal for studies where left over metal catalyst can produce unacceptable interference with experiments. These BNNTs and their unusual morphology are shown in Figure 1.5.

This method has a number of advantages for the creation of doped boron nitride nanotubes. The process introduces no metal catalyst, which would interfere with measurement of electromagnetic properties. Additionally, the reaction is performed at an extremely high temperature, increasing the chances of a dopant diffusing into the structure of the BNNTs. This process was adapted to synthesize doped boron nitride structures as discussed in [Section 5.3](#). One end result was a material structurally similar to some of the materials made by the IL method.

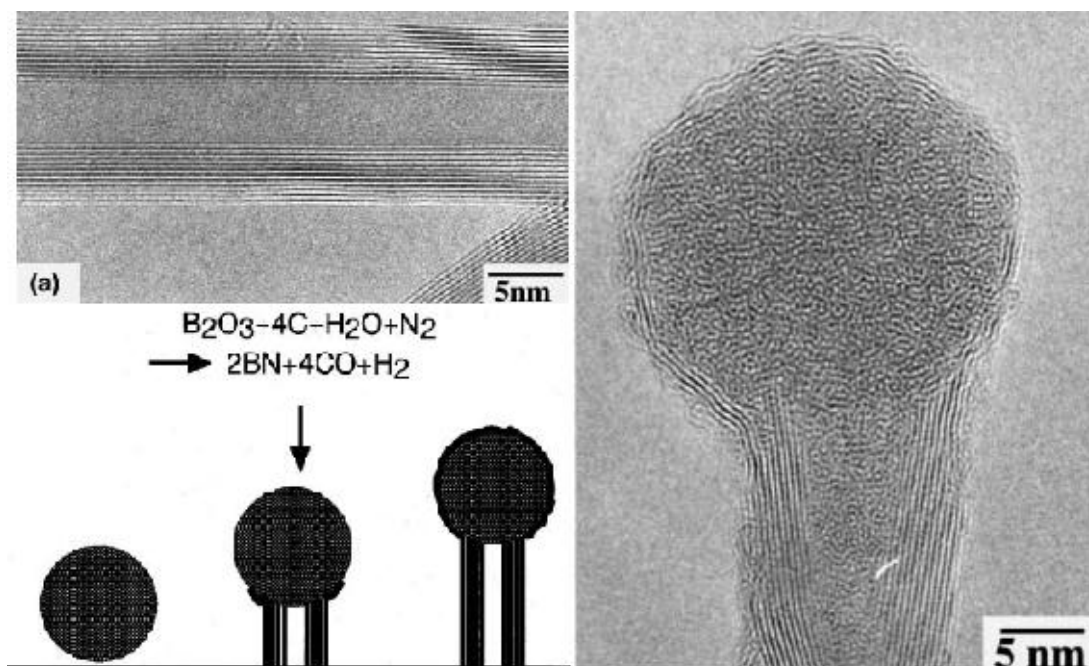


Figure 1.5 TEM images of BNNTs grown without using metal catalyst showing large bulbous tips. A schematic of the growth mechanism is also included.

1.5 Mechanical Properties of Nanotubes

Nanotubes have been shown to have tremendous axial strength and good bending flexibility [19-26]. Clearly, these mechanical properties could be highly useful and they are one of the primary reasons so much attention is devoted to nanotubes. Nearly all theoretical analysis to date predicts that BNNTs should be mechanically more stable than CNTs. One example indicates that CNTs are nearly 50% stiffer than BNNTs when comparing their respective Young's moduli [27]. However, actual experimental evidence is far kinder to BNNTs. Chopra, Zettl et al. have reported a Young's modulus of 1.25 ± 0.24 TPa [28] for multiwalled BNNTs which compares very well to the value of 1.28 ± 0.59 TPa [22], which Wong et al. report for multiwalled CNTs. These values should be regarded carefully, as nanotube strength is highly defect dependent, and depends on a hosts of variables such as tube diameter, impurity content, etc., so each literature value

will probably be different from another. However, these values do seem to indicate that BNNTs can at least be competitive with CNTs in mechanical properties. While BNNTs should be much weaker than CNTs in theory, most likely, BNNTs have fewer defects, closing much of the gap (see Figure 1.7 which alludes to this by examining nanosheets). There is a possibility that on average BNNTs could be stronger than CNTs due to this. When considering which will perform well in composites one should also remember that some BNNTs will bond better to some matrices than CNTs and vice versa, meaning the substrate material may ultimately determine which nanotube is preferred.

For practical applications, most likely one would consider performance in composites to be more critical than Young's modulus of individual nanotubes. BNNTs have not been studied extensively in composites, but there has been interesting preliminary work done [29]. BNNTs are much more thermally stable than CNTs in oxidizing environments which gave them preference in reinforcing glass composites used in solid oxide fuel cells. These fuel cells function in space bound rockets which typically operate in temperatures well over 700° C. The enhancement in strength of the composite was demonstrated with a small loading of BNNTs (4% wt) added to a barium calcium aluminosilicate (BCAS) glass powder of composition (mol%) 35BaO–15CaO–5Al₂O₃–10B₂O₃–35SiO₂ or 56.4BaO–8.8CaO–5.4Al₂O₃–7.3B₂O₃–22.1SiO₂ (wt%) with an average particle size of 14.2 μm (G18 glass). Even this relatively small loading resulted in a dramatic increase in mechanical properties. The fracture toughness went up 35% and the strength nearly doubled. This would not be a desirable application for CNTs because of the extremely high temperatures of use; however, BNNTs should function acceptably. Figure 1.6 shows a strength distribution of the G18 glass with and without BNNT

reinforcement and Table 1.1 shows the enhancement in mechanical properties because of the addition of BNNTs. The work in this dissertation shows that addition of nanotubes can dramatically alter the strength of metals ([Chapter 6](#)), but when using graphene, there is no benefit ([Appendix A](#)). This probably arises due to the fibrous morphology of carbon nanotubes compared with the two-dimensional morphology of graphene.

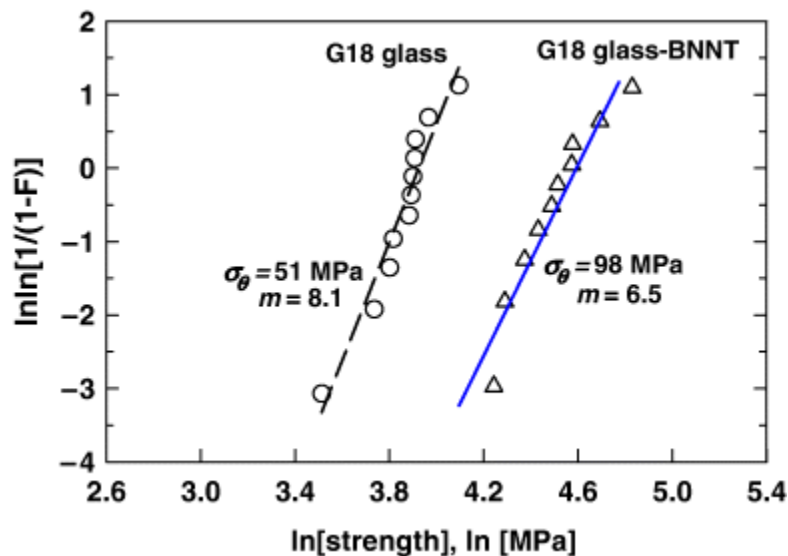


Figure 1.6 Weibull strength distribution of G18 glass reinforced with 4 wt% BNNTs. The Weibull data for G18 glass are also included for comparison [29]. Y-axis is a dimensionless number, used to understand the statistical variation of mechanical properties in the samples.

Table 1.1 Strength and Fracture Toughness of G18 Glass and Composite Reinforced with 4 wt% BNNTs [29]

Property	G18	G18-BNNT composite
Flexural Strength (MPa)	48±7	92±17
Fracture Toughness (MPa*m ^{1/2})	0.51±0.03	0.69±0.09

1.6 Graphene and its Boron Nitride Analog

From 2005-2013, interest in carbon-based graphene has increased dramatically. Graphene has a number of exciting electrical and optical properties which are different from that of other carbon allotropes. Graphene is simply a single layer of graphite. The first ‘synthesis’ method of graphene was the legendarily simple process of applying scotch tape to graphite and peeling away repeatedly. Subsequently, the lead investigators won the Nobel Prize for this rather clever experiment. Other techniques were discovered which could create graphene in a more efficient manner. A novel chemical vapor deposition synthesis technique to create graphene is given in the appendix, where growth mechanisms are discussed. Logically, boron nitride can also form single flat layers, however, the amount of work done on them is minimal compared to the amount of work done on carbon.

Single layer boron nitride flakes, BN-nanosheets, were first synthesized in a method very similar to the method first used to synthesize carbon graphene [30]. Boron nitride powders were put onto adhesive tape, and this sample itself was exposed to adhesive tape which was then pulled off. This process was continued until very few layered h-BN was obtained [31]. A flake was then put onto a TEM grid and underwent electron microscopy. A high current beam was used in the TEM to remove layers so that a single layer of h-BN was obtained, a BN-nanosheet. Sonication can also be used to produce single layers of h-BN. One hour of sonication of BN crystals in a 1,2 dichloroethane solution of poly(*m*-phenyl-enevinylene-co-2,5-dioxy-*p*-phenylvinylene) can produce very few or even single layered h-BN sheets [32]. A TEM of the h-BN-nanosheets and graphene is shown in Figure 1.7.

The defects of the BN-nanosheets and C-graphene are found to be very different. Single hole defects are found in graphene, and a reconstruction is used to form a pentagon-nonagon structure in some cases (the other cases have no reconstruction). Stone Wales defects are also seen frequently in graphene. The BN graphene layers have no observable Stone Waals and reconstruction defects, indeed, the B-B and N-N bond is highly unfavorable energetically. This is interesting because curved h-BN sheets have been shown to have some reconstructed defects, but flat sheets apparently don't have a significant number. The only observable defects are single vacancy defects, and evidence indicates only one type of element, either nitrogen or boron, is the missing atom, i.e. all of the vacancies are the same missing element. Unfortunately, which element is missing is currently unknown.

This type of material could find use in conjunction with C-graphene as an insulator, especially since the lattice constants of both materials are similar. The study of absorbates on this material would also be of interest. These materials have also been referred to as Boron Nitride Nanoribbons (BNNR) [33-36], especially when the nanosheet is rectangular (having a small width in comparison to length). Novel materials discussed in this dissertation ([Sections 5.2](#) and [5.3](#)) seem to be similar to graphene and its boron nitride analog. These materials could be joined together to create nanoheterostructures, much like the nanowires previously discussed, and the nanotube heterostructures to be reviewed in the next section.

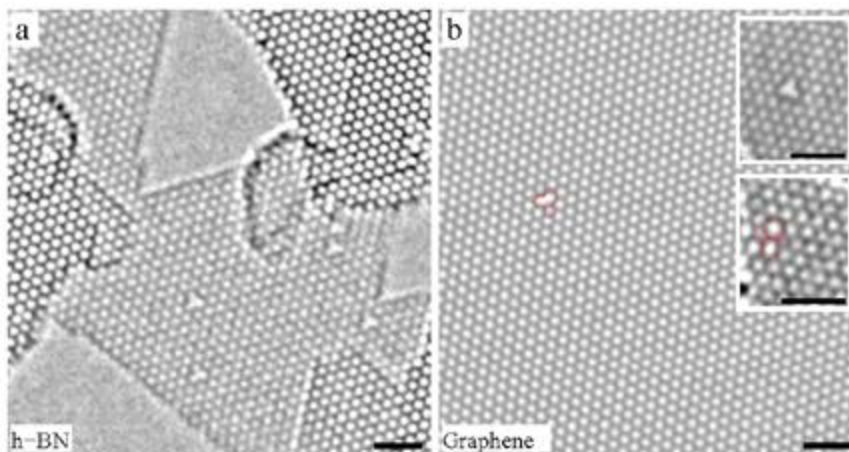


Figure 1.7 Comparison of h-BN and graphene membranes. a.) h-BN membrane and b.) single-layer graphene membrane HRTEM images. Note that the h-BN only has monovacancies but graphene shows reconstructed vacancies [37].

1.7 Boron Carbonitride Nanotubes and Nanotube Heterostructures

Since the lattice constants of BNNTs and CNTs are similar, they should be compatible enough to form structures which are mixtures of the elements. Doping of CNTs with boron and nitrogen is well known [38-42]. In fact, the materials are so similar they can form completely hybrid structures with little restrictions. Indeed, the carbon content can vary from 0% (a pure BNNT) to 100% (a pure CNT) and have any value in between. Boron Carbon Nitride Nanotubes (BCNNTs) were first reported [43] using arc discharge (most nanomaterials discovered in the 90's were first synthesized using the arc discharge technique), but they can be synthesized with a variety of techniques now.

A current-voltage curve of a bundle of BCNNTs is shown in Figure 1.8 [44]. In this particular sample, the carbon content was low. The bandgap was estimated to be 1 eV (very close to that of silicon which is 1.12 eV at room temperature). Obviously, depending on the study, this value will change and be most strongly correlated with carbon content, though defects and other physical traits of the tube will affect the value.

However, the most important observation is that this value is between that of CNTs and BNNTs. The optical properties follow suit. A photoluminescence (PL) spectrum is shown in Figure 1.9, note that as that carbon concentration decreases the BCNNTs spectra move to the left, closer to the emission spectra of BNNTs. The intensity of the spectra can change from sample to sample even when growth conditions are held constant. As manufacturing processes become more sophisticated, this difference should disappear. Interesting electrical and optical properties should whet the research community's interest, but the ability to form semiconducting devices such as junctions makes BCNNTs a truly fascinating material. These devices are similar to the heterostructures discussed in [Section 1.3](#) and can hopefully be made using variations of the IL method.

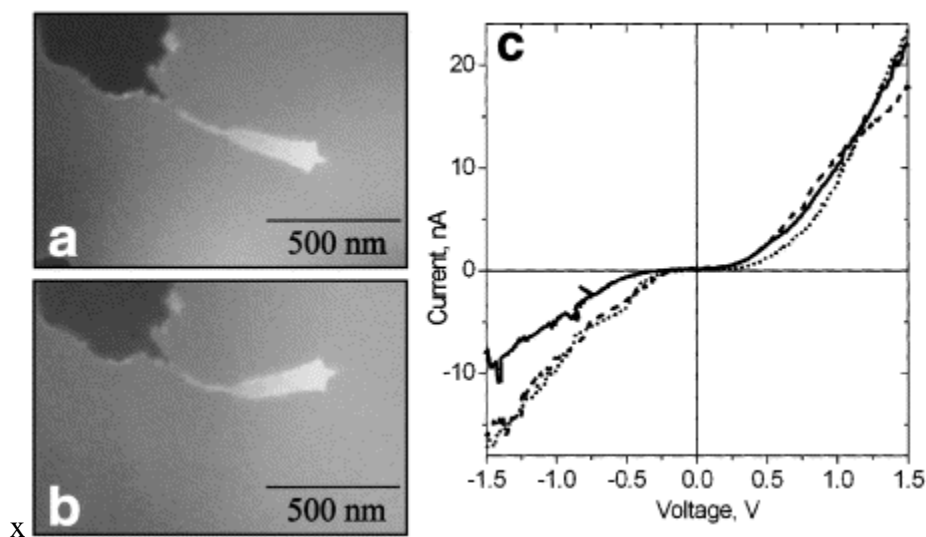


Figure 1.8 a.) Fresnel projection microscope images a.) before and b.) after transport measurements. The current-voltage curves are shown in c.) where the solid curve is the first sweep, the dashed curve is the second sweep, and the dotted curve is the third sweep. These curves are that of a semiconductor with an estimated band gap below 1 eV [44].

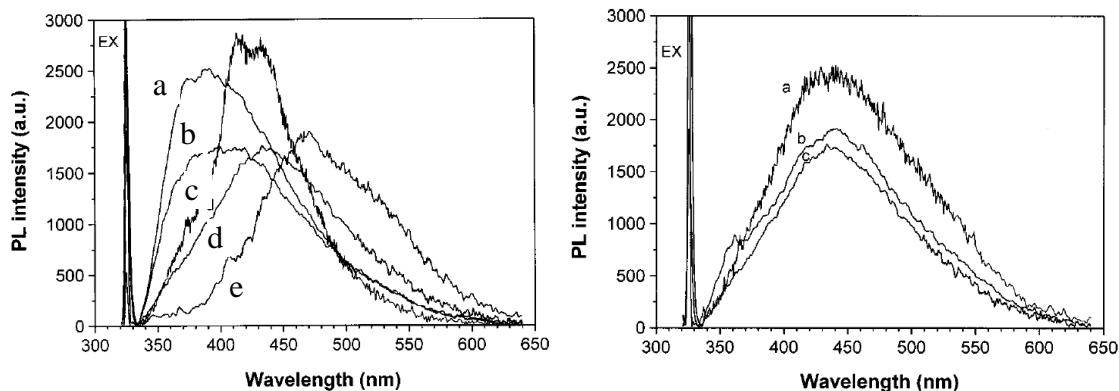


Figure 1.9 (Left) Room temperature PL spectra from BCNNTs. As one goes from a-e the concentration of C decreases. (Right) Attempt to match reproducibility of d from left images. Note that even when growth conditions are held supposedly constant there is some variation in PL intensity, though the frequency remains unchanged [45].

A nano-diode arrow has been successfully synthesized by creating a junction between a CNT and a BCNNT. A hot filament chemical vapor deposition process was used to grow the carbon nanotubes, and the process conditions were simply changed mid run by leaking in B_2H_6 and lowering the temperature to allow the growth of BCN. The results of this experiment are shown in Figure 1.10. Note the IV curve of the BCN-CNT junction is that of a rectifier. This particular rectifier is extremely small and thermally/mechanically incredibly stable. This is not the only clever use of BCN and C to create nanocircuits. By modifying the process described to make junctions, one can even create Y-junctions as shown in Figure 1.11.

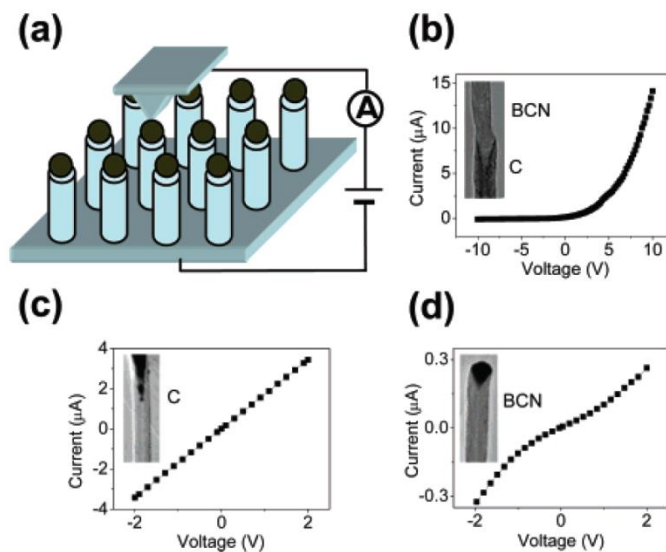


Figure 1.10 Layout of experimental setup used to measure electrical properties of individual tubes with AFM. Current-voltage curve of b.) BCNNNT/CNT junction, c.) individual CNT and d.) individual BCNNNT [46].

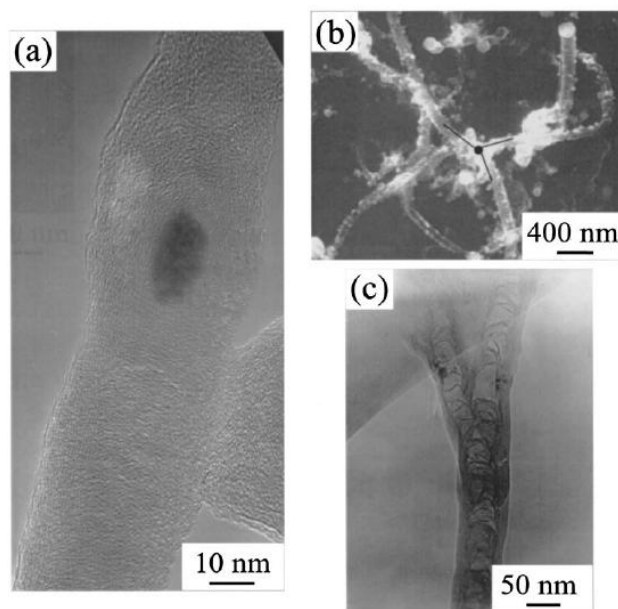


Figure 1.11 BCN nanojunctions grown from split nickel particles: a.) TEM image of a heterojunction showing deactivated catalyst. b.) SEM of three nanotubes grown from tip of a single nanotube. c.) Close-up image of Y-shaped nanojunction [47].

The extremely high thermal conductivity of all the nanotubes, the high conductivity of CNTs, and the insulator quality of BNNTs and the ability to grow junctions between them rather easily could prove to be highly valuable to the electronics

industry of the future. Remarkably complex electronic devices could be synthesized on nanotubes by controlling the CVD properties. For example, one could create a nanotube with sections composed of BNNTs, CNTs, and BCNNTs allowing for each section to have a tailored bandgap. If catalyst splitting can be controlled more effectively, Y junctions can also be formed. Circuits composed of these junctions could be much smaller, rid themselves of heat effectively (and make less heat to begin with), and would be far more thermally and mechanically stable than current circuits. An even more tantalizing idea would be utilizing the incredibly small dimensions available using these processes to allow the exploitation of exotic quantum effects to perform computation.

Nanotube and nanowire heterostructures would be highly desirable products from the IL method. The IL method and its variations have been shown to be able to create a number of novel nanomaterials and nanoheterostructures, whose properties have not been determined. However, once these materials have been evaluated, potential applications and desirable devices can be identified. As will be seen in this dissertation, the IL method has a remarkable ability to create a number of nanomaterials and can innately create radial nanoheterostructures, and through careful manipulation of growth conditions, can also create axial heterostructures. However, before discussion of the novel results of this dissertation can commence, a review of the synthesis and characterization techniques utilized is necessary.

CHAPTER 2

SYNTHESIS AND CHARACTERIZATION TECHNIQUES USED

2.1 Chemical Vapor Deposition (CVD) Synthesis

Chemical Vapor Deposition (CVD) synthesis is the most discussed synthesis method in this dissertation. For ease of use and future efforts at scaling, all of the work is done at atmospheric pressure (AP). CVD synthesis is generally convenient and can be done at low cost and risk. A sample (usually a catalyst or sometimes a catalyst mixture on a substrate which can in some cases be the solid reactant) is placed in a chamber which is pumped down and then back filled with flowing inert gas. Alternatively, the chamber initially filled with air can be purged with inert gas flow creating an oxygen-free environment. The sample is then heated to a specified reaction temperature, and various reactant gases (typically mixed with an inert carrier gas) are allowed to flow into the reaction chamber. The reactant gases then react with each other, the reactant solid (if needed), and the catalyst particles in the chamber. If the correct conditions are achieved a novel nanomaterial can be formed, as shown in Figure 2.1.

Usually, a direct gas-to-solid reaction would proceed too slowly to form some of the nanomaterials to be discussed in this study, and would certainly proceed too slowly to explain the fast growth mechanisms observed [48] in the growth of some of these nanostructures. The Vapor-Liquid-Solid (VLS) model successfully circumvents these kinetic issues entirely by assuming that the catalyst/solid reactant forms a liquid droplet at the CVD reaction temperature. The reactant gases then dissolve in the droplet until the supersaturation point. Afterwards, the reaction produces a solid which grows with the

liquid catalyst at its head. This is shown in Figure 2.2. The VLS method is assumed to be the mechanism of growth for most of the nanomaterials grown in the research discussed in this dissertation.

While the ability to alter the pressure and/or apply a low pressure plasma could result in new structures, larger yields, or higher quality structures; overall, these methods are more complicated and more difficult to implement. Modern manufacturing techniques employing CVD are usually carried out at a low pressure or under plasma conditions, because these modifications can introduce significant benefits. However, with the goal of developing commercially viable, cost-effective methods, the focus of this dissertation will be on nanomaterials produced by atmospheric pressure CVD. The two experimental systems used for this purpose in this dissertation are shown in Figure 2.3.

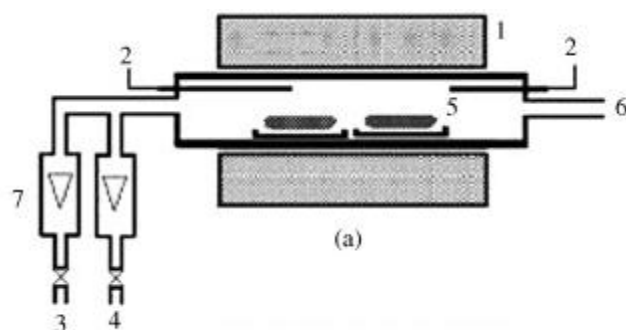


Figure 2.1 (a) Fixed-bed technique: (1) furnace, (2) thermocouple, (3) carrier gas, (4) reactant and carrier gases, (5) catalyst/solid reactant (if needed), (6) outlet [49].

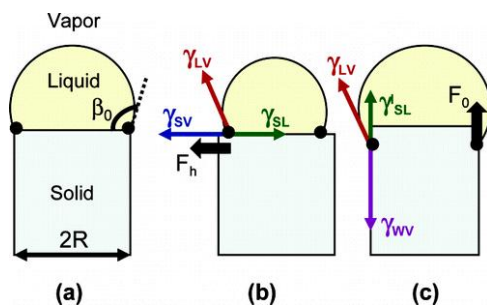


Figure 2.2 Illustration of the VLS method which is used to grow a nanorod. This is the presumed method of growth for the nanomaterials to be discussed in this work [50].

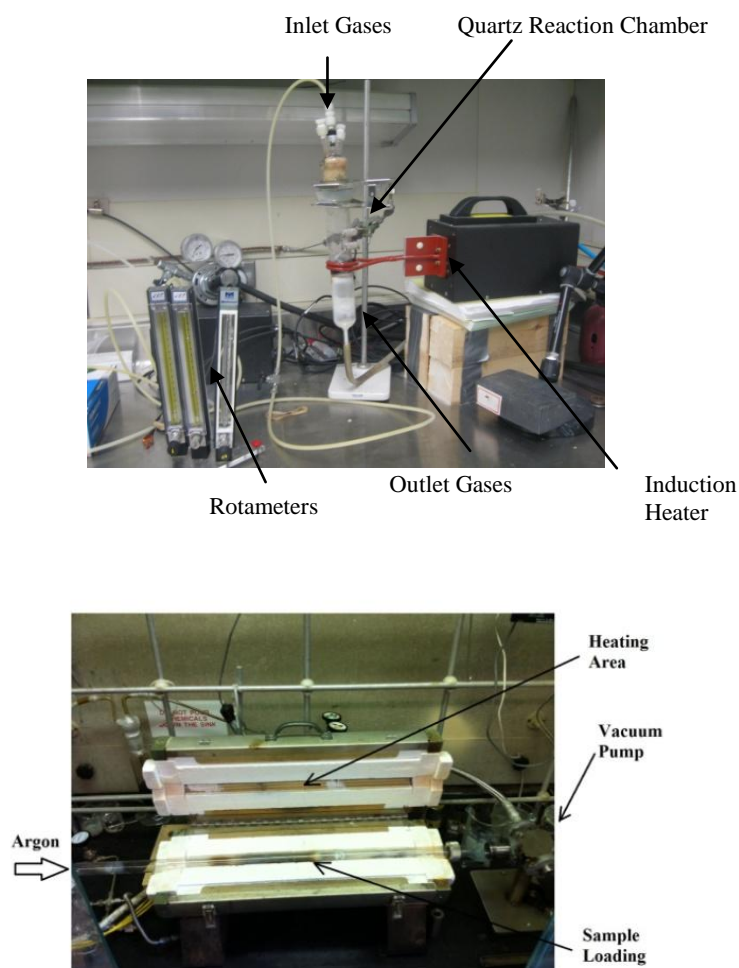


Figure 2.3 High (top) and low (bottom) temperature CVD systems used in this study.

2.2 Scanning Electron Microscope (SEM)

The principle of operation of an SEM is based on the raster scanning of the surface of a sample with a narrow beam of electrons. Radiation from the specimen stimulated by the incident electron beam is detected, amplified, and used to modulate the brightness of a second beam of electrons scanned synchronously with the first beam across a cathode ray tube display. Currently, the resolution of an SEM can approach 0.5 nm, rivaling that of the transmission electron microscope (TEM), and it can handle specimens as large as silicon wafers. Therefore, it is widely used to provide morphological information of

nanomaterials at nanoscale resolution. Combining SEM with EDX, chemical analysis is also achievable at these resolutions. An SEM is much less expensive and easier to use than a TEM, so it is typically used to screen samples, which are then examined further at higher resolution and with electron diffraction using TEM. The materials synthesized during the course of the research for this dissertation were all initially examined using SEM. In an SEM, an electron beam is generated either thermionically using a tungsten filament or a lanthanum hexaboride cathodic source. These electrons are then accelerated to an energy which is typically in the range from 40 eV to 200 eV. The beam of electrons leaving the gun is then focused onto the specimen by one or more condenser lenses. Typically, the final objective lens has been of the pin-hole design with the sample sitting outside the magnetic field of the lens, since this arrangement gives good physical access to the specimen. A series of magnetic lenses and apertures then directs the electron beam. As the beam raster-scans the sample surface, which should have sufficient electrical conductivity to allow the electrons to flow, scattered electrons and X-Rays are generated which reveal morphological and chemical information about the sample (see Figure 2.4 for the schematic for an SEM). Most of the SEM images in this dissertation were obtained with the In Lens detector of an SEM. The In Lens detector provides the highest two-dimensional resolution of the sample, but some of the topographic information is lost. Every sample was also analyzed for elemental composition using Energy Dispersive X-ray (EDX) spectroscopy. Here, incident electrons excite inner shell electrons of the sample, which are re-emitted as X-rays [51] that provide elemental information. EDX analysis, therefore, gives a reasonably accurate quantitative measure of the sample

composition. The processes involved in EDX spectroscopy are shown schematically in Figure 2.5.

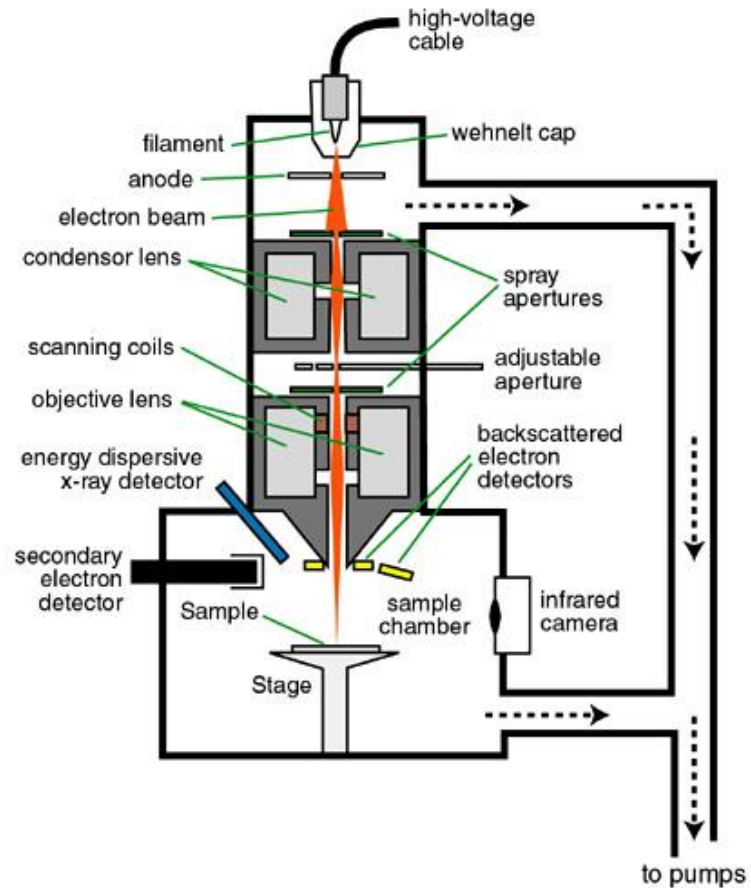


Figure 2.4 Schematic showing the set up of an SEM [51].

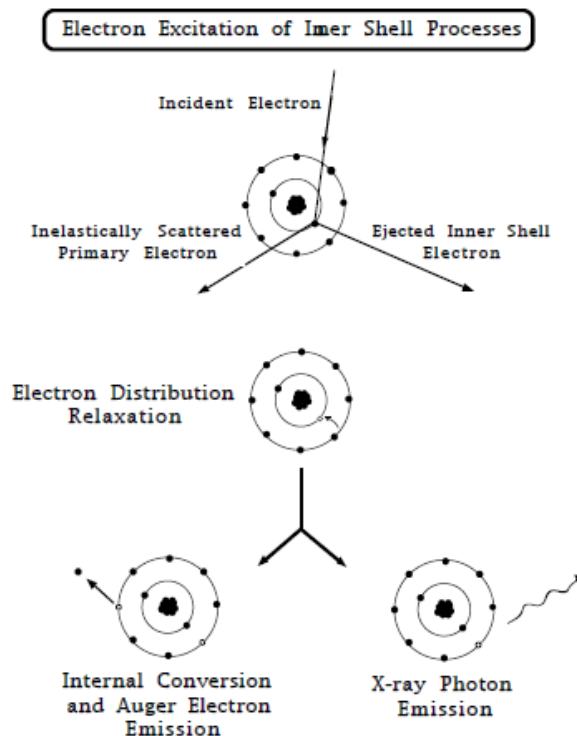


Figure 2.5 An electron which impacts an inner shell electron will scatter inelastically and will cause the impacted electron to eject [52]. When another electron drops into the place of the now missing electron, either an X-Ray photon is given off at a characteristic energy level, or an outer electron is ejected (Auger Emission). Energy dispersive X-ray (EDX) emission spectroscopy is used for chemical analyses in this dissertation.

2.3 Transmission Electron Microscope (TEM)

Proper operation and understanding of a TEM is critical for comprehending and charactering nanoscale materials. A high resolution TEM produces images of unparalleled spatial resolution (down to 0.1 nm, which is near the length scale of atoms) while also providing important structural information and elemental compositions at these extremely small length scales. For an electron with $KE = 200$ eV and rest mass energy of 0.511 MeV, the associated DeBroglie wavelength is 0.23 pm, approaching the size of atoms. This size is about three orders of magnitude smaller than that of a 1 eV photon consistent with equations 2.1 and 2.2. This explains why optical microscopes can

only image at a spatial resolution in the range of the wavelengths of visible photons which lie between 400 and 700 nm.

$$d = \frac{\lambda}{2n \sin \alpha} \approx \frac{\lambda}{2 \text{NA}} \quad (2.1)$$

Where λ is wavelength, NA is numerical aperture of instrument, and d is maximum resolution.

$$\lambda_e \approx \frac{h}{\sqrt{2m_0 E \left(1 + \frac{E}{2m_0 c^2}\right)}} \quad (2.2)$$

Where h is Planck's constant, m_0 is the rest mass, c is the speed of light, E is the energy of the electron, and λ_e is the electron wavelength corrected for relativistic effects.

The TEM process, although quite straightforward, requires an extremely sophisticated device for high resolution nanoscale imaging. A beam of electrons travels through a vacuum in the column of the microscope and is then transmitted through an ultrathin sample specimen where the two interact to generate an image. Generally, a tungsten filament or a lanthanum hexaboride source is used to produce electrons thermionically or by field emission, respectively, by application of a large voltage (100 kV to 300kV) to the source. The electron beam is then narrowed by the use of apertures. After it interacts with the sample, different lenses based on electromagnets are used to alter which focal plane is imaged. In this manner, facile switching between imaging and diffraction modes as well as focusing is achieved. The beam is then directed to a charge coupled device (CCD) detector attached to an yttria aluminum garnet screen coupled to a

computer for image and related data analyses. Figure 2.6 shows a schematic of a TEM used in both imaging and diffraction modes.

2.4 Selected Area Electron Diffraction (SAED or SAD)

An important principle in the operation of a TEM is the dual wave-particle nature of the electron (Equation 2.1). The wavelength of the electrons is much smaller than the crystal spacings in a solid. This means that the incident beam will produce electron diffraction patterns strongly dependent on crystal structure and orientation in a sample. A region of a specimen can be selected for examination using an aperture as shown in Figure 2.6 to obtain selected area electron diffraction (SAED). This is important for polycrystalline specimens where more than one crystallite can contribute to the diffraction pattern. SAED of nanoparticles or nanocrystals gives ring patterns analogous to those from X-rays, and can be used to discriminate nanocrystalline from amorphous phases present in the sample. Largely amorphous samples will give rise to broad or diffuse ring patterns.

SAED has numerous advantages in comparison to comparable diffraction techniques. Unlike X-ray diffraction (to be discussed later), which typically lacks the ability to focus on precise areas of a sample, an electron diffraction pattern can be taken from an area as small as 4 nm^2 . This allows for spatially located crystallographic information. An example of the utility of this ability would be if one had a composite material that was a mixture of a number of different morphologies and structures, such as nanowires mixed with nanoparticles of a different structure. In a TEM, one can determine the structure for each morphology separately and image the area under examination. This would not be possible in an X-ray diffraction experiment. The

interaction with matter is also much stronger with focused electron beams, which means electron diffraction can be used to generate useful information much more quickly, as long as the sample remains stable in a high energy electron beam. Finally, the Ewald sphere for electrons is much larger than that of X-Rays (see Figure 2.7), because the wavelength of typical 200 keV electrons is two orders of magnitude smaller than that of X-rays, which means that more reflections are found in an SAED pattern. The difference in the imaging and the diffraction modes in a TEM is shown in Figure 2.6. Rarely in the dissertation, convergent beam electron diffraction is (CBED) performed. In SAED, a parallel beam of electrons is used to create a diffraction pattern, but in CBED, a convergent cone of electrons is used. The advantage of the CBED is that multiple angles of incidence are used simultaneously, providing 3-D analysis of the crystal. CBED can be far more difficult to interpret than SAD, and so is only used for appropriate situations.

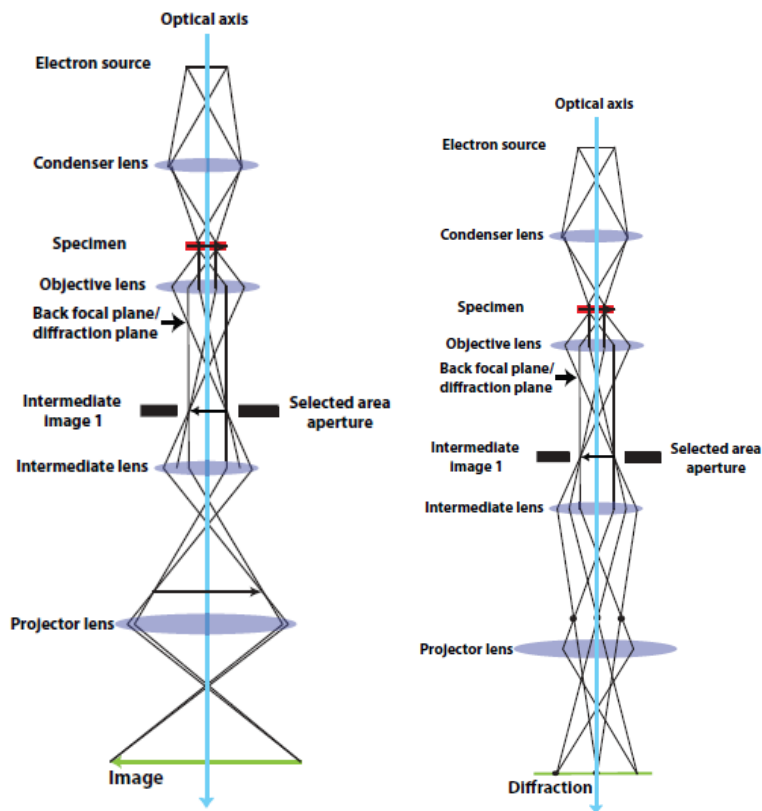


Figure 2.6 Schematic of a TEM operating in the imaging mode (left) vs. diffraction mode (right). The instrumental set up is the same but the electron beam in each is focused differently [53].

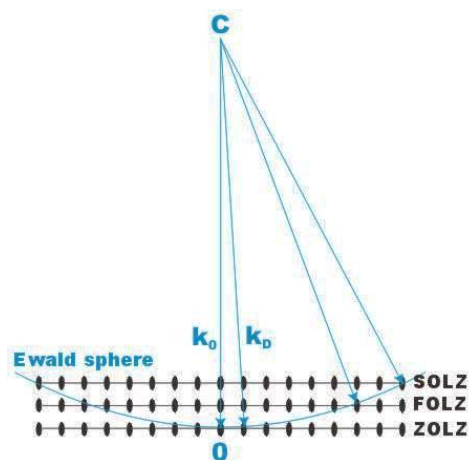


Figure 2.7 Schematic illustration of the Ewald sphere. The points which are intersected by the circle cut out from the Ewald sphere will diffract because they satisfy the Bragg condition [54].

2.5 Electron Energy Loss Spectroscopy (EELS)

EELS is another analytical technique which can be performed in TEMs equipped with spectrometers. When a beam of electrons is transmitted through a sample, electron energy loss occurs and the spectrum obtained can be used to extract the following: atomic composition, details about chemical bonding, valence and conduction band electronic properties, surface properties, and element-specific pair distance distribution functions. Moreover, the spectra of 3d transition metals can be analyzed to identify the oxidation states of the atoms, for instance in oxides [55]. This ability to "fingerprint" different forms of the oxidation states of the same element is a strong advantage of EELS over EDX, which is primarily because EELS has a spectral resolution of 1 eV or better, whereas EDX resolutions are at least an order of magnitude lower. For purposes of the work done in this dissertation, the most critical mode of energy loss of the electron beam is the inner shell ionization of the atoms (Figure 2.8). In this phenomenon, the electrons in the beam strike inner shell electrons of the sample, which causes some electrons in the beam to lose a very specific amount of energy. This is highly dependent on the electron shell structure of the material in question. By examining this energy loss, one can determine the elemental composition of the sample. EELS was used to determine the composition of some of the nanomaterials synthesized in this work, and was frequently used to confirm the results obtained by EDX and vice versa.

EELS is often considered complementary to EDX. EDX excels at identifying the atomic composition of a material, is quite easy to use, and is particularly sensitive to heavier elements, particularly those with $Z > 5$. Another differentiating feature is that EDX can be performed under the SEM and also under the much higher spatial resolution of a

TEM. EELS on the other hand can only be performed in a TEM using ultra-thin (<100 nm) samples.

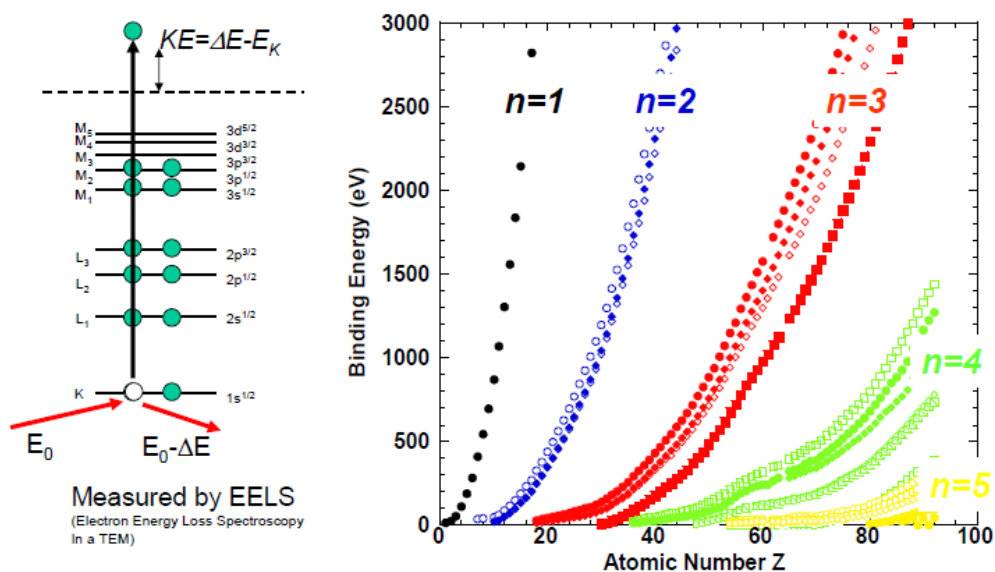


Figure 2.8 (Left) Illustration depicting how an incident electron loses energy when striking an inner shell electron in a sample. (Right) Binding energy vs. atomic number, Z , plots showing variation of the binding energies in each electronic shell as a function of Z [56].

2.6 Raman Spectroscopy

When light interacts with matter, it can be either absorbed or scattered. During the scattering process, the majority of the light is scattered elastically with no energy transfer between light and the medium. This is a high probability event which is referred to as Rayleigh scattering. However, when the oscillating electric field of the incoming radiation interacts with the medium, there is also a small, but finite probability of inelastic scattering as a result of the generation of vibrational excitations in the medium. Inelastic scattering is a low probability event which is typically six orders of magnitude weaker than Rayleigh scattering.

During the interaction, the energy carried by incoming photons excites vibrational states within the medium by distorting the electron clouds around molecular or

intermolecular bonds. This shift in electron cloud distribution results in a change in bond polarizability (α) and induces a temporary dipole moment (P) and excites the molecule or solid into a virtual excited state when the interaction is non-resonant. Since excited states have finite lifetimes, the scattering events occur in 10^{-12} sec or less after which the molecule or solid relaxes back to its ground state, emitting a photon at a specific frequency (ν_{vib}). Depending on the energy difference between the original and the relaxed states, there is a change in the frequency of the emitted light from that of the incident light. Molecules or solids mainly relax back to the pre-excited state and emit the same frequency (ν) light as the elastic or Rayleigh scattering.

Molecules or solids that relax to a different vibrational state, however, emit a photon of different energy to give rise to inelastic scattering. This generated photon is shifted in frequency by an amount corresponding to the energy of a particular vibrational transition. If the final state is more energetic than the initial state, the emitted photon will be shifted to a lower energy ($\nu - \nu_{\text{vib}}$) designated as a Stokes shift. If the final state is less energetic, the emitted photon will be shifted to a higher frequency ($\nu + \nu_{\text{vib}}$) resulting in an anti-Stokes shift as shown in Figure 2.9 and Figure 2.10. Such a change in energy gives rise to inelastic scattering of photons to provide a vibrational frequency fingerprint of the molecule or solid. The energy difference corresponds to a vibrational or rotational (librational in the case of solids) frequency of a molecule within gaseous, liquid and solid media, or of vibrations between molecules or ions in a solid, and is referred to as the spontaneous Raman Effect.

Since the Stokes process is more probable than the Boltzmann factor-dependent anti-Stokes process, it is relatively more intense and is usually measured and displayed in

modern Raman spectrometers. If the incident photon energy corresponds to an actual electronic state of the molecule or solid, the Raman process is resonantly enhanced in intensity. The Raman intensity can also be enhanced by surface plasmons generated on nanostructured silver or gold substrates to give rise to surface-enhanced Raman scattering (SERS). SERS, in combination with resonance Raman scattering can, under the right conditions, allow single molecule detection. For purposes of this dissertation, spontaneous Raman scattering and fourier-transform infrared spectroscopy (FTIR, discussed later) will be used to characterize the vibrational frequencies with the structure of the nanomaterials prepared.

In practice, Raman scattering spectroscopy is carried out using a laser of known wavelength, in conjunction with a holographic grating spectrometer, a notch or edge filter to eliminate the Rayleigh scattering wing, and a CCD detector coupled to a computer for sensitive detection of weak light signals as shown in Figure 2.11.

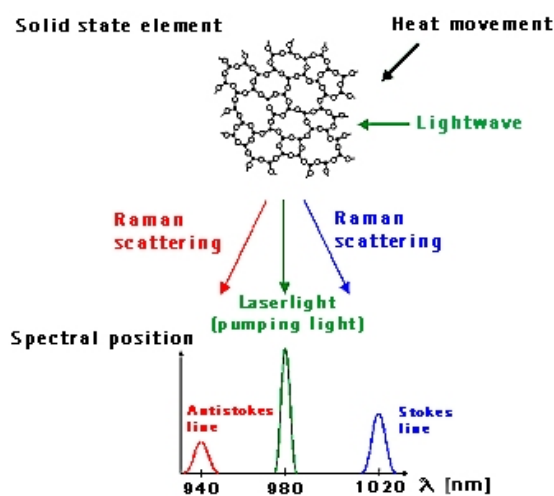


Figure 2.9 Raman effect vs. Rayleigh scattering. Note that in Rayleigh scattering, the scattered light has the same wavelength as the incident laser radiation, but in Raman scattering there is a vibrational frequency-dependent shift in wavelength either to higher values (anti-Stokes) or to lower values (Stokes) [57].

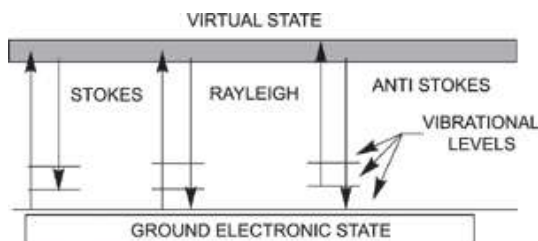


Figure 2.10 Stokes, anti-Stokes, and Rayleigh lines. Note that in Rayleigh scattering the electron goes from the ground state to the virtual state and back to the ground state without interacting with the vibrational levels [58].

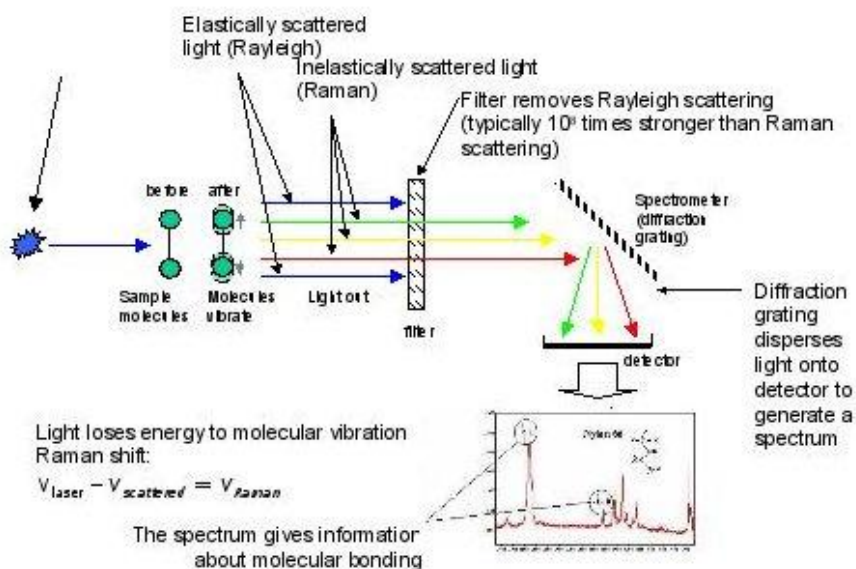


Figure 2.11 Schematic depiction of Raman Spectroscopy [59]. Inelastically scattered light from a sample after it has been irradiated by a laser beam. A filter removes Rayleigh light, and a spectrometer is used to disperse the Raman light onto a detector, where the intensity vs. frequency of the light is recorded.

2.7 Four Point Probe Electrical Characterization

The simplest method of determining the electrical properties of a material is to attach two probes to the material at a known distance, and then pass a current between them and measure the voltage drop. This gives the resistance via Ohm's law, $V=IR$, where V is the

voltage, I is the current and R is the resistance. By varying the sample temperature, other important properties can be gleaned, such as whether the material is a metal or a semiconductor. The problem with the 2-point method is that the contact and interconnect resistances cannot be taken into account, making it only suitable for very approximate measurements. The 4-point probe method (Figure 2.12), however, overcomes the problem of extraneous resistances by positioning 4 probes on a sample – one pair for the current and the other pair for measuring the generated voltage as depicted in the figure. This makes the measured resistance basically come from the sample itself.

A diagram showing how the four point probe technique works is given in Figure 2.12. In order to perform this on the nanoscale, specialized chips had to be made. A chip was designed which had several leads already built into it, and that would be easily navigated on SEM. A sample was then sonicated in a liquid to create a suspension and was deposited onto the chip. The chip was then taken to an SEM, and carefully, the location of the nanomaterials was then recorded. This was made easier by the design of the chip itself. Then, noting the locations of the nanomaterials, an overlay was designed for each individual chip. The overlay would put gold contacts directly onto the nanomaterial, in the manner depicted in Figure 2.12. Finally, the chips were taken to have overlay leads built onto the nanomaterials of interest. This was done using e-beam lithography. A nanomaterial with leads drawn onto it (via the overlay) and a view of the entire overlay of one chip, which connects many nanomaterials to leads, is given in Figure 2.13.

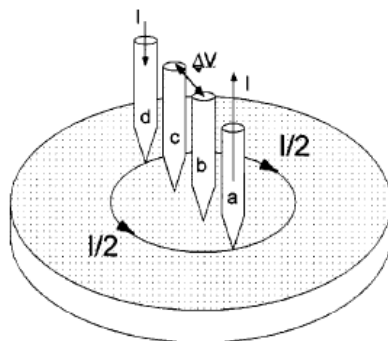


Figure 2.12 Schematic of a 4-point probe measurement. Note the current flow through terminals a and d and the voltage drop between b and c [60].

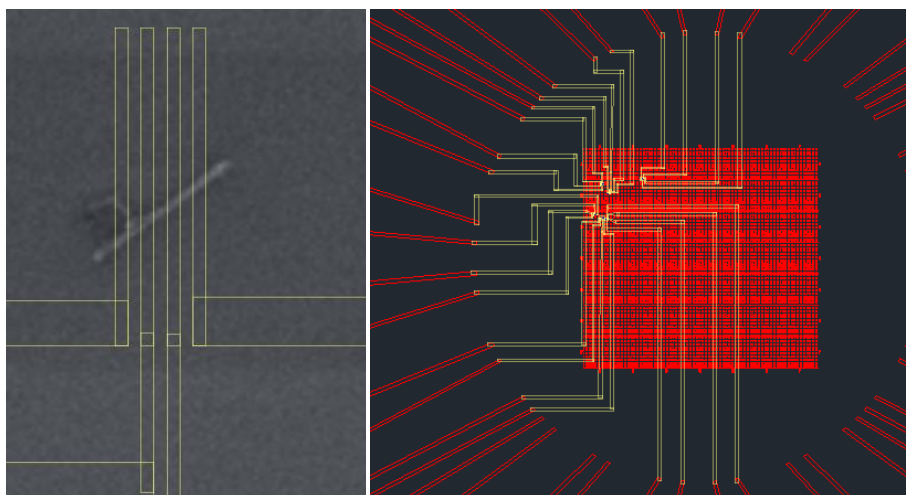


Figure 2.13 (Left) SEM image of 50 nm thick boron nanowire with leads drawn onto it. (Right) Overlay drawn onto entire doped silicon chip. Six separate nanomaterials can be tested with this one chip if they are placed on the red center grid.

Unfortunately, due to time constraints, the electrical measurements could not be made before the dissertation due date. However, they will be performed shortly after the final submission of the dissertation and results will be published in a peer reviewed format.

2.8 Other Techniques Used

2.8.1 FTIR (Fourier Transform Infrared Spectroscopy)

FTIR is used to obtain the spectra associated with the following: infrared-activated intra- and inter-atomic vibrations, rotations, librations and translations in a

solid, liquid or gas. Infrared activation occurs when atomic or molecular motions excited by infrared light give rise to a change in dipole moment. FTIR is complementary with Raman scattering spectroscopy discussed above, which measures the Raman-active atomic or molecular motions via a second order scattering event rather than by a direct absorption, reflection or emission process as in infrared spectroscopy. Raman activity occurs when the vibrational motion (quanta of which are referred to as phonons) causes a change in bond polarizability or charge density. FTIR spectra are typically taken using the following: absorption, reflection, emission or attenuated total reflection (ATR) techniques. An FTIR spectrometer simultaneously collects spectral data in a wide range. This confers a significant advantage of FTIR over a conventional dispersive infrared spectrometer which measures intensity over a narrow range of wavelengths discretely [61]. FTIR has made dispersive infrared spectrometers essentially obsolete (except for use in the near infrared, primarily for pharmaceutical monitoring applications). The term *Fourier transform infrared spectroscopy* originates because a mathematical Fourier transformation process is required to convert the raw data into the actual spectrum.

2.8.2 Hardness

Hardness is a measurement of the ability of a material to resist localized plastic deformation. The hardness measurements done in this dissertation are of the Rockwell variety. Rockwell Hardness tests apply a minor load followed by a major load onto a sample. The load is applied either through a steel sphere or a diamond cone. The amount of deformation in the sample is measured and an instant read out of the hardness is given. The Rockwell hardness measurement is easy and economical, and allows for quick feedback on the mechanical properties of a material. The tensile strength of a material

tends to correlate well with its hardness [62]. A number of conversion tables are available to translate a tensile strength to hardness value and vice versa. Realistically, this can prove difficult for a heterogenous material. For example, a surface hardened material can have a very high measured hardness, but can have relatively low compressive strength. This is because hardness only measures a small sample volume in comparison to a compressive strength test.

2.8.3 Compressive Test (Mechanical Property)

In compressive testing, a small pellet of a sample is loaded with increasing force. The strain induced by the force is then recorded. This creates a stress-strain diagram. The stress strain diagram can be used to determine Young's modulus and the ultimate tensile strength. The compressive mechanical properties are a critical parameter for a material. The compressive test was used in this dissertation to evaluate the mechanical properties of a number of nanotube-metal composites. The hardness tests were used to screen for interesting samples, but the compressive test was used as more reliable measurement of mechanical properties. This is because it tests a much larger sample volume, and provides more useful information than a simple hardness value [63].

2.8.4 ICP-AES (Inductively Coupled Plasma Atomic Emission Spectroscopy)

This method was used in many cases to determine the elemental composition in a material. Three concentric quartz tubes and an attached RF generator are utilized to create an inductively coupled argon plasma. The argon is then ignited/ionized by a Tesla coil and driven towards the RF Generator. The argon is now a plasma and has an average temperature of 7000K. If a sample is then introduced into the plasma, decomposition occurs, leaving only the constituent atoms. The constituent atoms emit radiation at

characteristic frequencies, allowing a qualitative identification of the atoms and a determination of the quantity of each element. The ICP technique is extremely accurate and is widely used to provide qualitative and quantitative information regarding the elements in a sample [64].

2.8.5 XRD (X-Ray Diffraction)

X-rays are short wavelength electromagnetic radiation produced when electrically charged particles of sufficient energy are decelerated in an X-ray tube. The high voltage maintained across the electrodes in the tube draws electrons toward a metal target (the anode) producing X-rays at the point of impact that radiate in all directions. Tubes with copper targets, which produce their strongest characteristic $K_{\alpha 1}$ radiation at a wavelength of about 1.5 \AA , are commonly used for obtaining powder diffraction patterns. General scattering occurs if a crystal or polycrystalline powder encounters an incident X-ray beam. This is followed by diffraction in accordance with Bragg's Law given by equation 2.3 [65]. Each crystalline material has a characteristic crystal structure, which gives rise to a unique X-ray diffraction pattern.

An X-ray diffractometer consists of a source of monochromatic X-ray radiation and an X-ray detector situated on the circumference of a graduated circle centered on the powder specimen. Divergent slits, located between the X-ray source and the specimen, and similar slits between the specimen and the detector limit non-diffracted radiation, reduce background noise, and collimate the radiation. The detector and specimen holder are mechanically coupled with a goniometer so that a rotation of the detector through $2x$ degrees occurs in conjunction with the rotation of the specimen through x degrees, at a fixed 2:1 ratio. A curved-crystal monochromator containing a graphite crystal is normally

used to ensure that the detected radiation is monochromatic. When positioned properly just in front of the detector, only the $K_{\alpha 1}$ radiation is directed into the detector and the K_{β} radiation is directed away. The signals from the detector are filtered by pulse-height analysis, scaled to measurable proportions, and sent to a linear rate meter for conversion into a continuous current for output to a computer. In this manner, an X-Ray diffraction can be created and displayed to a user in a convenient fashion.

$$n\lambda = 2d \sin \theta \tag{2.3}$$

Where, d is the distance between spacings, n is an integer, λ is wavelength of the incoming radiation, and θ is angle of incidence.

CHAPTER 3

CARBON-BORON NANOSTRUCTURES

Carbon is perhaps the most flexible element in the periodic table when it comes to making nanostructures and compounds. Indeed, the relative ease with which carbon can form nanostructures is apparent in their ability to form a variety of nanomaterials such as nanotubes, buckyballs, and graphene ([Section 1.4](#)). This makes the addition of carbon precursor gases a very exciting modification to the IL process. The process was the standard IL process discussed in [Section 1.1](#), however, methane was added in the amount of 10 sccm when the reaction temperature was achieved. The results when using MgB_2 were extremely exciting, however, the results when using $\text{Mg}(\text{BH}_4)_2$ were more mundane.

When using the IL method with $\text{Mg}(\text{BH}_4)_2$ and methane, the result is simply a mixture of boron nanowires and carbon fiber/nanotubes. Somehow, the carbon and the boron do not seem to react together. Since none of the work was considered novel, further investigation was discontinued. However, there might be some method or alteration to the process which can induce the boron and carbon to react to form a single structure when using $\text{Mg}(\text{BH}_4)_2$, and only further study will elucidate that. When using MgB_2 in the IL method, the results are far more interesting.

When utilizing MgB_2 with methane in the IL process, the product is a novel nanoheterostructure. SEM analysis was first conducted. The material seemed to be a nanowire with roughly 40-60 nm thickness and several microns length. The yield of this material was (determined qualitatively from SEM images) particularly good, and seemed

to ubiquitously cover the sample, as evident in Figure 3.1. After SEM analysis was found to be revealing, the material was taken for TEM analysis.

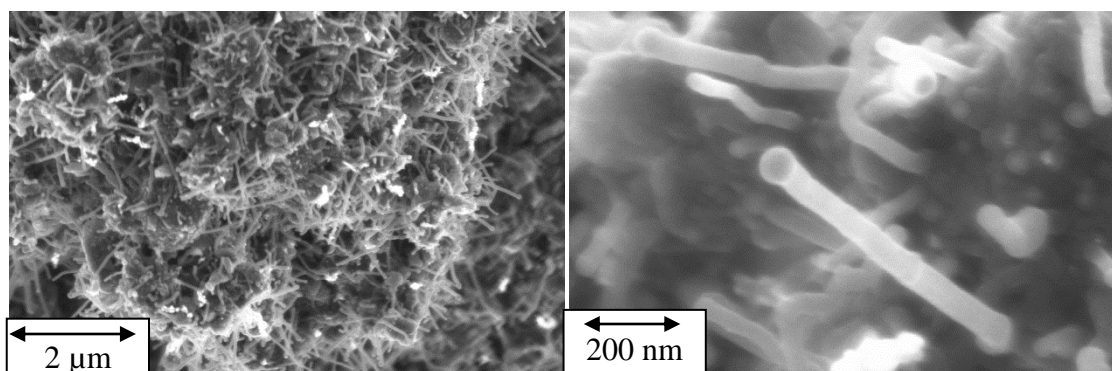


Figure 3.1 (Left) SEM image of numerous boron-carbon nanowires protruding from surface of particle. (Right) High magnification image of nanowire, clearly showing the nanowires are not completely straight and have a bulbous tip from the catalyst.

The TEM analysis of the material revealed even more information. TEM first confirmed the results from the SEM analysis. The material did seem to be thin nanowires grown at a high yield that had slight bends and curves. The nanowires clearly grew out of large particles with the catalyst at its head (see Figure 3.2). Most excitingly, there seemed to be two materials joined together intimately. This would be a core shell nanowire, a radial heterostructure (see [Section 1.3](#)). The outer part of each nanowire including the area curled around the catalyst appeared to be a layered, ‘wavy’ structure. Based on the image analysis, the interlayer spacing appeared to be between 0.36 nm to 0.39 nm, as confirmed in analysis from Figure 3.3 to 3.5. Determining the exact spacing is difficult because sharp images could not be made, most likely because the spacing itself varies significantly due to the ‘wavy’ nature of the layers. The inner part of the nanowires seemed to be similar to the nanowires which came from the IL process using MgB_2 without any dopant gases. Using FFT analysis, the spacings were found to be 0.48

nm, 0.38 nm, and 0.43 nm, with angles of 46.9° , 77.7° , and 54.6° as shown in Figure 3.4.

Further analysis was performed using EELS analysis in STEM mode.

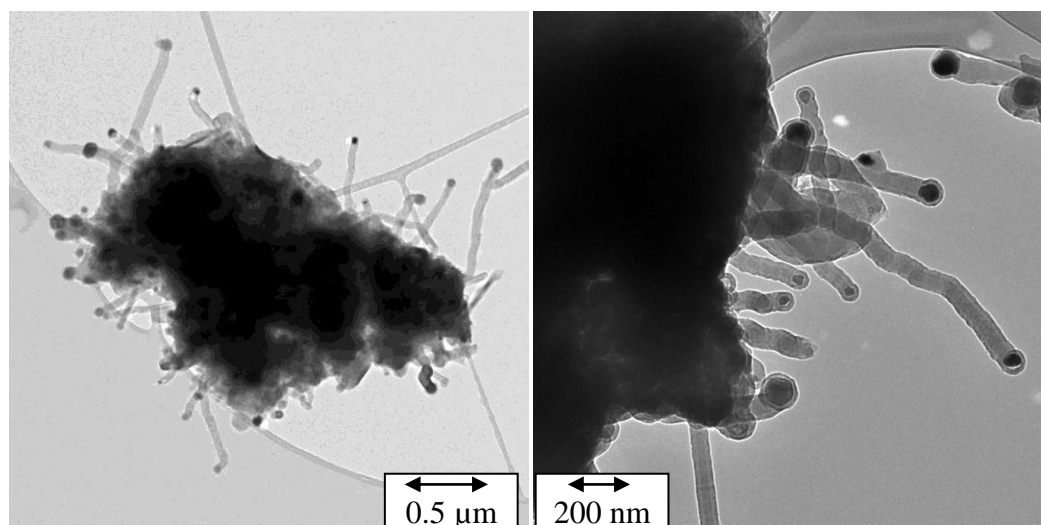


Figure 3.2 (Left) TEM image of core boron-carbon nanowires growing out of catalyst. (Right) High magnification TEM image of the nanowires.

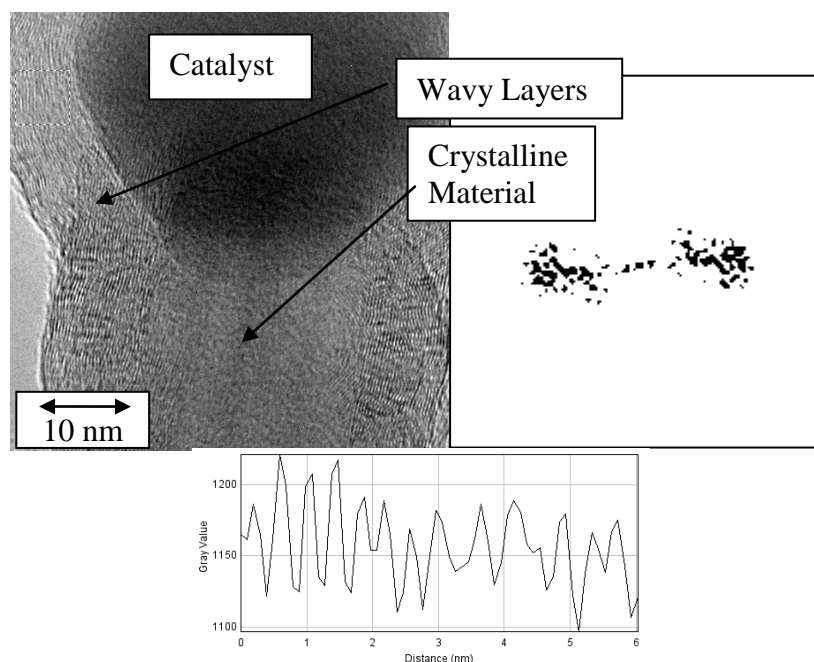


Figure 3.3 (Left) High resolution TEM image of catalyst particle in boron-carbon nanowire. Note the outside of the nanowire appears to be of a different structure than the interior of the nanowire. The outer part of the nanowire is the material which encapsulates the catalyst. (Right) FFT of the outside of the nanowire, which showed spacings of approximately 0.36 to 0.39 nm, size of box is 12.65 nm X 12.65 nm. (Bottom) Profile plot of outside of nanowire, confirming results from FFT analysis.

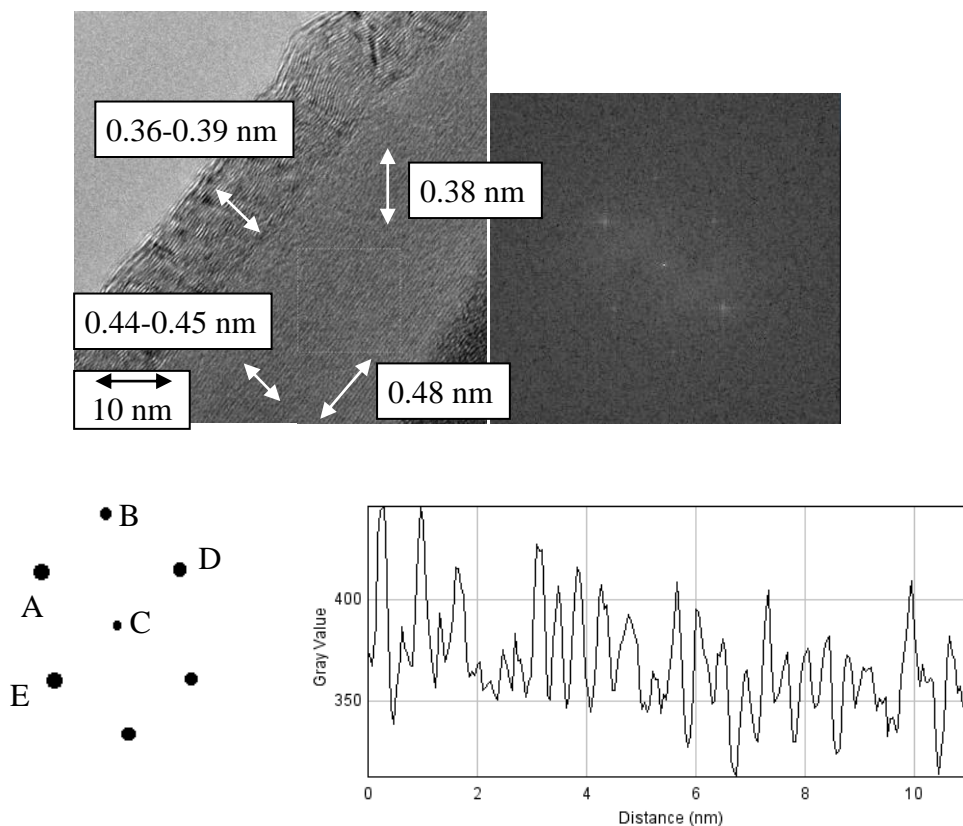


Figure 3.4 (Top Left) High resolution TEM image of boron-carbon nanowire. FFT was performed on the interior of the nanowire with labeled spacings and directions. (Top Right) Raw FFT of interior of nanowire, note that 6 different spacings are evident, size of box is 25.63 nm X 25.63 nm. (Bottom Left) Masked image of FFT with labeled points, making analysis easier. The following were measured using the ImageJ software suit, $EC=DC=.48$, $AC=.44$ to $.45$, $BC=0.38$, $\angle ACB=46.9^\circ$, $\angle BCD=54.6^\circ$, $\angle ACE=77.7^\circ$. (Bottom Right) Another profile of the outside of the nanowire, this confirms the results from Figure 3.

Using EELS analysis in STEM mode revealed the elemental composition and distribution of the nanowires (Figure 3.6). The inside and outside of the nanowire was found to be composed of boron and carbon, respectively. This, combined with the information from the bright field TEM analysis, reveals an interesting picture. Apparently, the nanowire heterostructure made in this process is a boron nanowire covered in layers of carbon. Essentially, it is a boron nanowire encased in a multiwalled carbon nanotube. The boron nanowire is basically the same structure that results from

the IL process without the use of dopant gases, however, in this case it is part of a heterostructure.

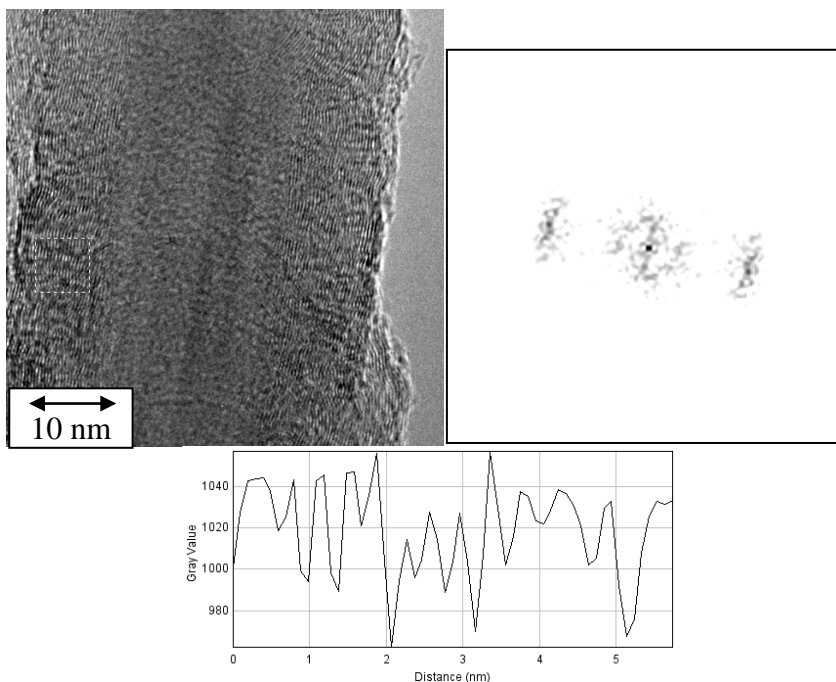


Figure 3.5 (Top Left) Another high resolution image of a boron-carbon nanowire. (Top Right) FFT analysis of the outer walls, again showing a spacing of approximately 0.36 nm to 0.39 nm, size of box is 12.75X12.75 nm. This shows the spacing of the material around the catalyst is the same as the material which goes along the outside of the nanowire. (Bottom) Profile plot of the outside of the nanowire, confirming previous results.

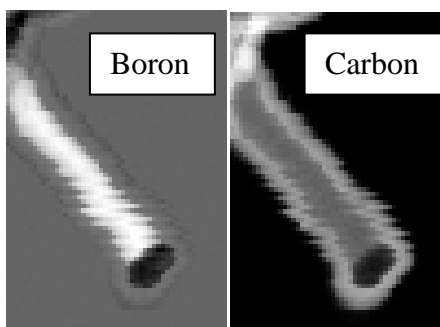


Figure 3.6 (Left) Boron map and (Right) carbon map. Note the boron is in the inside of the nanowire and the carbon is on the outside of the nanowire, including the catalyst head. The nanowire moved during analysis which is causing the raster scan distortion.

While this result is interesting, using other carbon containing gases, such as carbon monoxide or acetylene, could also result in novel structures. Alternatively, they could end up simply creating a mixture of boron nanowires and carbon nanotubes as is the case with $\text{Mg}(\text{BH}_4)_2$ and methane. The other question would be why the $\text{Mg}(\text{BH}_4)_2$ and the MgB_2 result in such different structures. Somehow, the borohydride prevents the mixture of the two elements into one structure. Finally, creating heterostructure is usually done by altering the growth conditions of a material *in situ*. This is a rare instance where one has demonstrated the ability to grow a nanoheterostructure using the same growth conditions throughout a run. This could have implications for the future synthesis of other nanoheterostructures. (This material should not be confused with simple boron carbide nanowires [66, 67], although it could almost be considered a novel phase of boron carbide.) Once the electrical properties of the C-BNT heterostructure is better known, applications can be determined.

CHAPTER 4

BORON-NITROGEN HETEROSTRUCTURES

4.1 Magnesium Oxide Filled Boron Nitride Nanotubes

The synthesis of a heterostructure using nanowires is a field with a variety of possible future applications in the semiconducting industry ([Section 1.3](#)). However, these efforts have mainly been focused on silicon based materials. This is mainly because silicon possesses a number of advantages over other semiconducting materials, making it the basis of nearly all modern electronics. However, boron possesses interesting properties as well. Boron is extremely light, and can form a variety of nanostructures [Patel et al., to be published]. Boron also easily reacts with nitrogen containing gases, creating the intriguing possibility of synthesizing boron to boron nitride nanowires. Boron possesses a bandgap of 1.6 to 2.1 eV and boron nitride has a bandgap of 5-6.4 eV, with both band gaps heavily dependent on crystal structure. Therefore, a junction between the two can have a bandgap difference of 2.9 eV to 4.8 eV, meaning these types of junctions could have applications dealing with violet to low energy UV emissions. These connections would act as PN junctions, due to the difference in the band gaps of the materials.

Of greater interest would be possible junctions between pure boron nanotubes and boron nitride nanotubes. The electronic properties of boron nanotubes are still unexplored, however, a junction between a boron nanotube and boron nitride structure could possess extremely exciting properties, much like theoretical junctions between carbon nanotubes and boron nitride nanotubes [68] or actual junctions between boron carbonitride nanotubes and carbon nanotubes ([Section 1.7](#)).

A method of growing boron to boron nitride heterostructures was attempted by modifying the IL method. The process was the standard IL process discussed in [Section 1.1](#), however, ammonia was added in the amount of 10 sccm when the reaction temperature was achieved. Ammonia was considered the most natural dopant gas to alter the IL method because boron reacts easily with nitrogen and boron nitride can form a number of different nanostructures ([Section 1.4](#)). The time interval was chosen because preliminary, rough experiments indicated the pure boron nanowires took at least 15 minutes at the reaction temperature to grow using the IL method. The hope for the intermittent doping scheme was that boron nanowires/tubes would grow normally when there was no dopant gas, and then when the ammonia was leaked in, the boron would take in the nitrogen from the ammonia. After the dopant gas was then shut off, the structure should grow normally again, as if no dopant gas was ever present. This would theoretically allow for the creation of alternating sections of boron nitride and boron, creating an axial nanowire heterostructure, see Figure 4.1. The intermittent doping with ammonia was done with both MgB_2 and $\text{Mg}(\text{BH}_4)_2$. Interestingly, using either material in the IL process with intermittent ammonia resulted in nanoheterostructures, though not in the expected manner.



Figure 4.1 Desired theoretical nanoheterostructure, where black represents boron and green represents boron nitride. This could be a nanowire or nanotube heterostructure.

When using MgB_2 , the resultant product is nanowires, though the yield is not great, as is evident through SEM analysis, see Figure 4.2. The wires seem very thin, ranging from 10 to 40 nm and are microns in length. They seem to also be fairly straight,

though there is some curvature at points, and a high degree of charging was evident, hinting the material was strongly insulating. The SEM analysis showed this could be an exciting material, so TEM analysis was conducted, which was far more revealing.

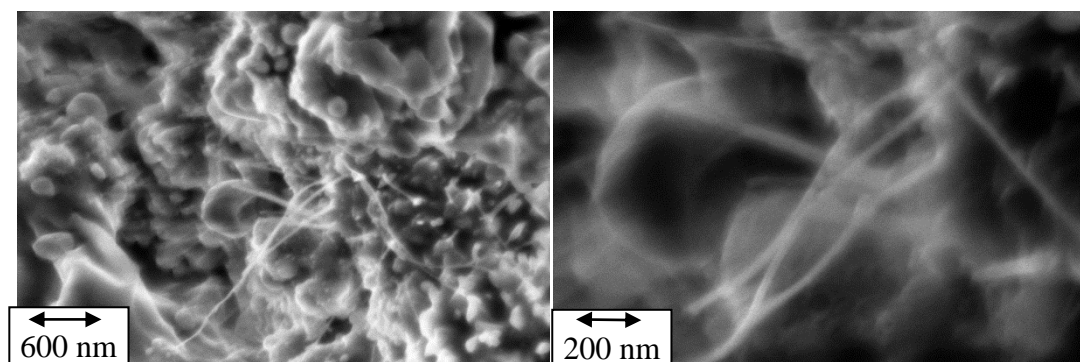


Figure 4.2 SEM images of nanowires which result from intermittent ammonia doping using the IL method with MgB_2 .

The TEM analysis, as seen in Figure 4.3, shows that the nanowires are composed of two separate materials; however, they form radial, not longitudinal nanowire heterostructures. The interior of the wire appears to be amorphous, and in comparison to the outside of the nanowire, exhibits higher Z contrast. This shows that the material inside the nanowire is of higher atomic weight than the material on the outside of the nanowire. The material on the outside of the nanowire seems to be a layered structure, like a multi walled nanotube. The number of layers range from four to five and some of the nanowires can grow extremely long. There is alternating TEM contrast, but it's difficult to attribute this to Z contrast, as it might also be due to strain in the nanowire or a charging effect. Z, or atomic number, contrast would indicate that the nanowire had different elemental compositions along the axis, which would be a success. However, contrast in the TEM can be caused by a number of different phenomena, therefore, EELS analysis must be conducted to obtain a reliable elemental distribution.

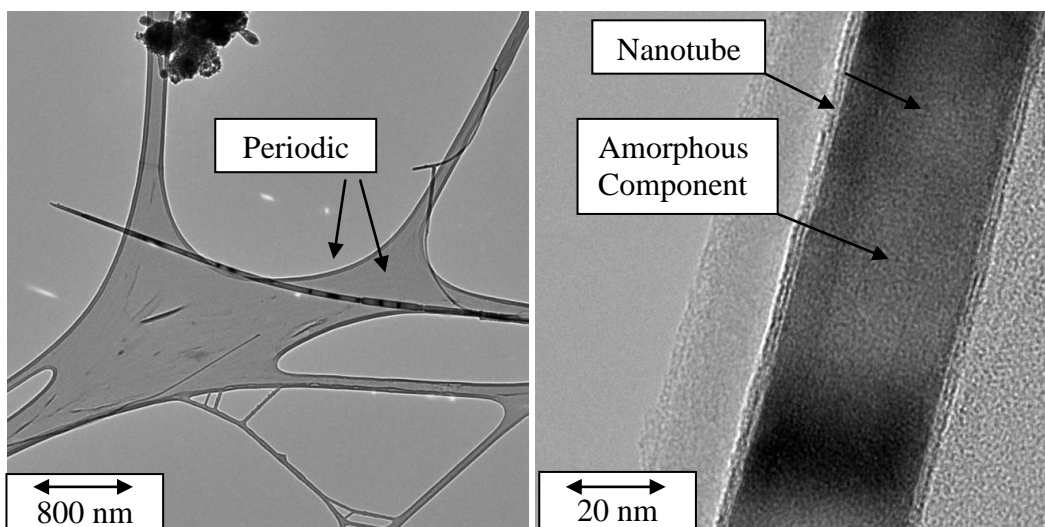


Figure 4.3 (Left) TEM image of a long nanowire from IL method with intermittent ammonia addition and MgB_2 . Note that there seems to be periodic contrast in the structure of the nanowire. (Right) Same nanostructure except at high magnification. Note the nanowire appears to be composed of two different structures, the interior is amorphous and the exterior is layered, like a nanotube.

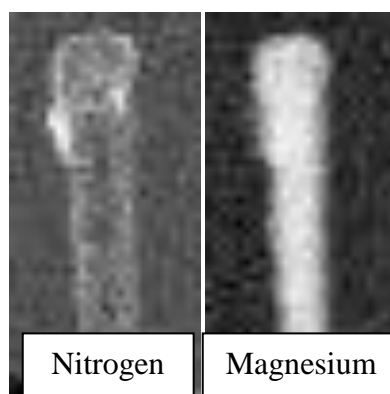


Figure 4.4 EELS mapping image of nanowire which results from MgB_2 and intermittent ammonia doping, with (left) showing nitrogen and (right) showing magnesium. This image also includes the catalyst at the head of the nanowire. The nitrogen is always found with boron and the magnesium is always found with oxygen in these nanowires.

EELS analysis was performed on the nanowire with a visible catalyst at its head, as shown in Figure 4.4. The EELS analysis revealed the inner and outer part of the nanowire seemed to be composed of magnesium oxide and boron nitride, respectively. The elemental composition of the nanowire does not vary along the length of the nanowire, only radially. This, combined with earlier analysis, reveals the resultant

nanowire is a radial nanowire, essentially the core shell type, with an interior composed of amorphous magnesium oxide and the exterior layers made of boron nitride. The heterostructure is a BNNT filled with amorphous magnesium oxide. This type of structure and some variations of it have already been reported [69]. While the product is not entirely novel, for this dissertation the true interest is how the ammonia dramatically alters the product of the IL method in an unexpected manner.

4.2 Pure Boron Nitride Nanowires

The results when performing the experiment with $\text{Mg}(\text{BH}_4)_2$ are slightly less unusual. The yield in this case is also relatively low, and the nanowires appear to be much straighter. The nanowires are very thin, again, from 10-40 nm in diameter and microns in length. Some nanowires appear to have discontinuities, which may be a result of the intermittent doping used to create them. The SEM images of this material are shown in Figure 4.5. TEM was performed on the sample as well, to reveal more information about the structure of the material.

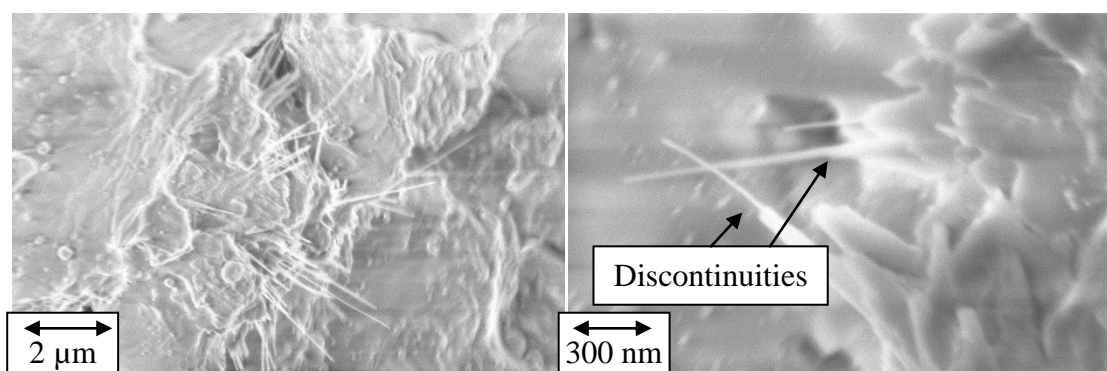


Figure 4.5 (Left) SEM image of nanowires which result from using intermittent doping of ammonia with the IL method using $\text{Mg}(\text{BH}_4)_2$. (Right) High magnification SEM image of same structure, showing some nanowires have interesting discontinuities which may result from intermittent doping.

TEM analysis initially showed that the nanowires are actually a mixture of thin and thick nanowires. The vast majority of the nanowires appear to have the morphology evident in Figure 4.6 and display a high degree of crystallinity. Additionally, some nanowires seemed to have discontinuities, as was evident in the SEM. While discontinuities visible in the TEM mode are interesting, they do not confirm the doping that was sought after. Therefore, EELS analysis was conducted.

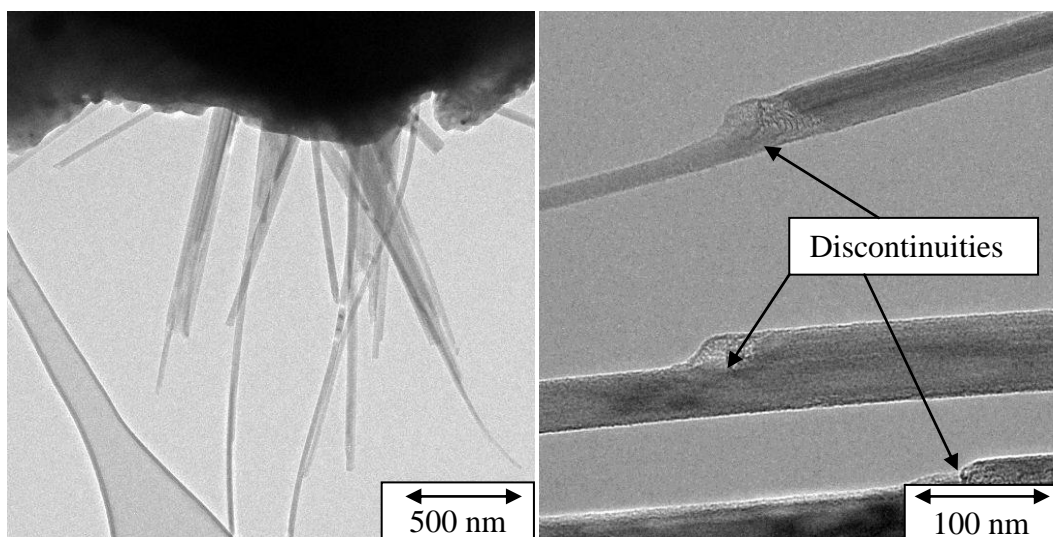


Figure 4.6 (Left) TEM Image of nanowire which results from intermittent doping of ammonia using the IL method with $\text{Mg}(\text{BH}_4)_2$. Note that the nanowires seem to long and thin, with diameters ranging from 10 nm to 40 nm, and lengths in the microns. (Right) High magnification TEM image of the nanowires showing that discontinuities in the material occur often. This might be due to the partial doping.

The EELS analysis was performed on the nanowires which seemed to comprise the majority of the sample. Mapping was performed with the target elements of boron and nitrogen. This was the most straightforward method to test the hypothesis that the nanowires would have sectional doping, creating PNP junctions, (junctions which can act as transistors). The boron and nitrogen were unfortunately found to be evenly distributed in the nanowire, as seen in Figure 4.7. This was confirmed by analyzing three different groups of nanowires (the results of one analysis are given). The boron and nitrogen also

seemed to be evenly distributed when examining discontinuous portions of the nanowire. Interestingly, there were clearly other types of nanomaterials in the product, though much rarer, and they were examined as well.

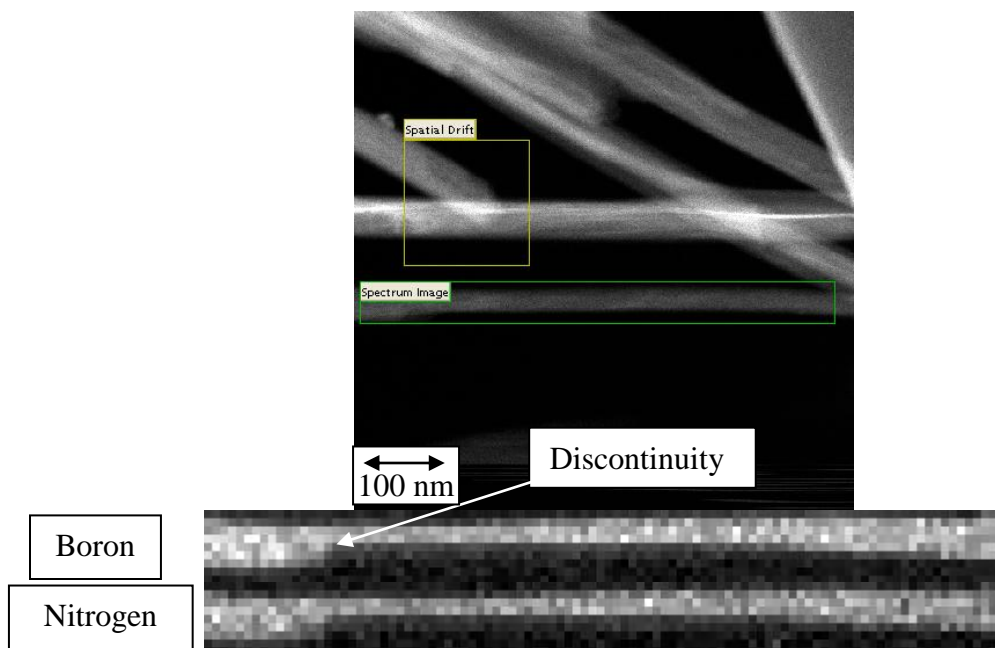


Figure 4.7 (Top) STEM image of representative nanowires from intermittent doping of ammonia using the IL method with $\text{Mg}(\text{BH}_4)_2$. (Middle) EELS map of boron and (Bottom) nitrogen. These nanowires seemed to have discontinuities which may have resulted from intermittent doping but the nitrogen is evenly distributed in the nanowire.

4.3 Pure Boron Nanowires and Boron Nitrogen Nanowire Heterostructures

A particularly thick nanorod was found and examined using TEM and STEM/EELS, as shown in Figure 4.8. The nanorod was obviously crystalline, and was relatively straight and long. (FFT analysis did show the nanowire was crystalline, unfortunately the resolution was not high enough to obtain crystal spacings). The nanorod was found using EELS analysis to be pure boron, having no nitrogen. While this type of nanorod was very rare in the sample, it does show that the process does result in product other than pure boron nitride nanowires. The rod was tested at the points indicated in Figure 4.8. A

final type of nanowire was found which was different than the materials previously discussed, which made it desirable for in-depth analysis.

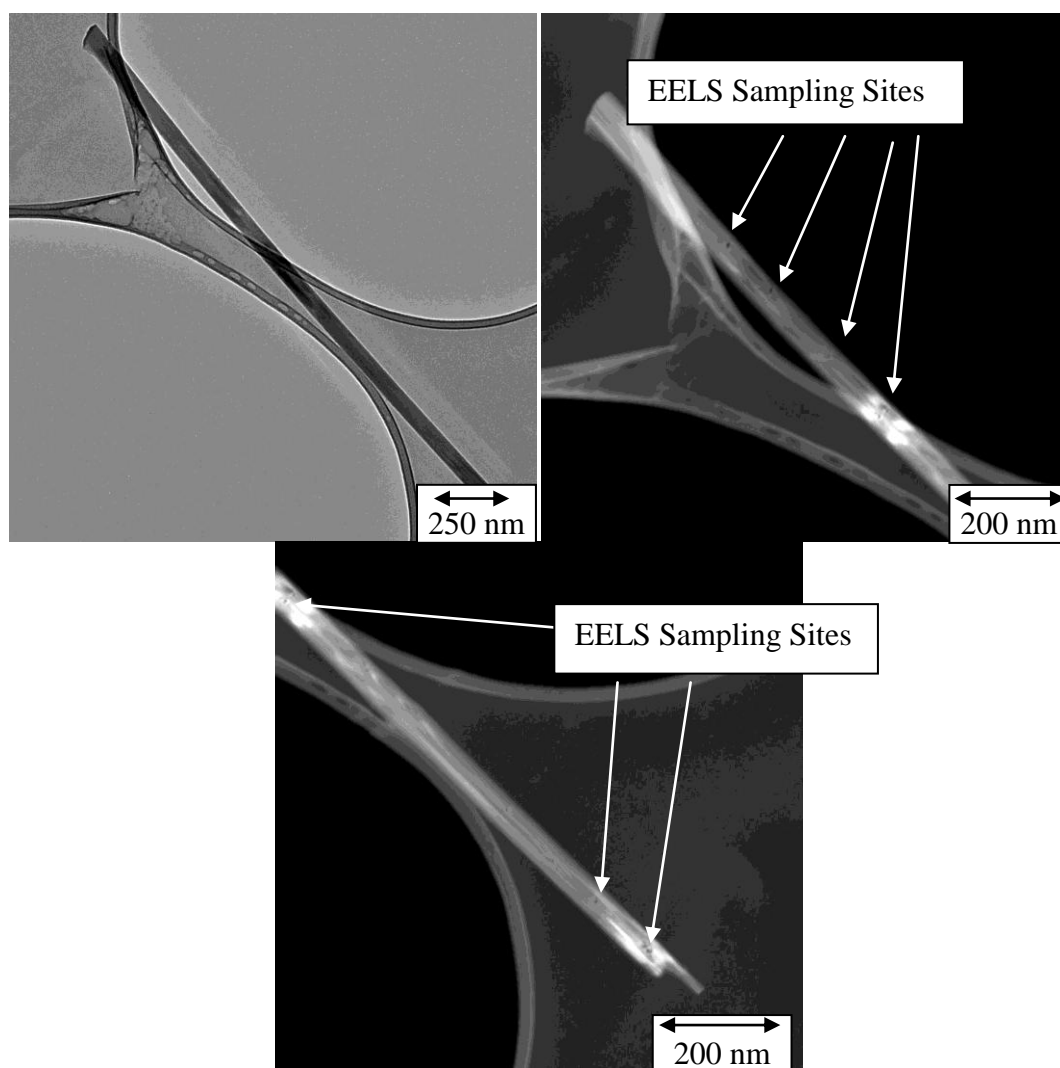


Figure 4.8 (Top Left) TEM image of relatively rare nanowire found in the product of the IL method using intermittent doping of ammonia with $\text{Mg}(\text{BH}_4)_2$. (Top Right and Bottom) STEM images of same nanowire showing where EELS analysis was performed. All EELS analysis indicate the material is pure boron.

The final nanowire found was particularly thick (it could be considered a nanorod, but comparing the thin end to the length makes it seem to be a nanowire), but also appeared to have some discontinuities in the structure, see Figure 4.9. There was also some visible TEM contrast, perhaps indicating some sort of strain. Therefore, it was

considered interesting for analysis with EELS. This particular nanowire finally did show some partial doping. The nitrogen was intermittently doped through the structure of the material, with boron present through the entire nanowire. While the doping is not clean, it does show it is possible to intermittently dope boron nanowires with nitrogen with the method described. The doping and yield of these nanoheterostructures could be improved perhaps by having a better method of controlling the ammonia flow or by varying other reaction conditions.

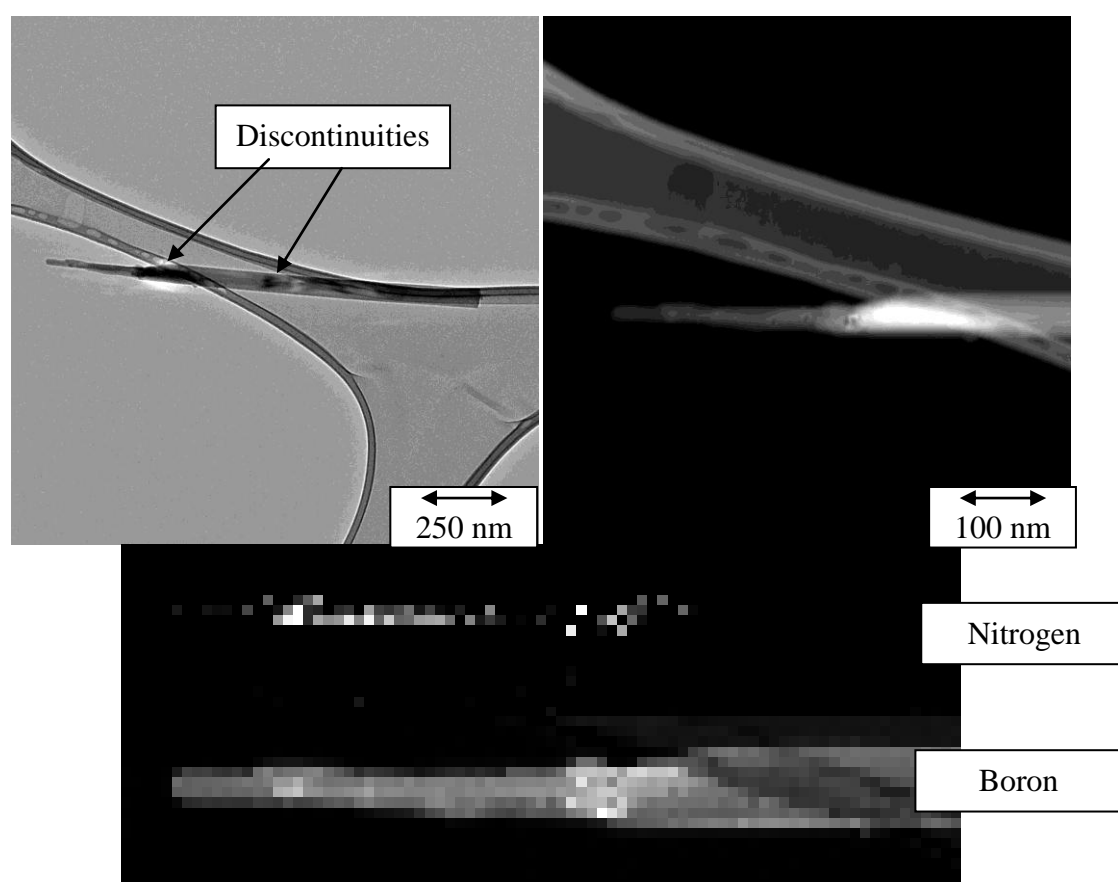


Figure 4.9 (Top Left) TEM image of very rare nanowire with obvious discontinuity. (Top Right) STEM image of same nanowire, showing damage from where EELS analysis was performed. (Middle) Nitrogen EELS map of nanowire, note that it is not continuous through the material. (Bottom) Boron EELS map of nanowire, note that unlike nitrogen boron is found through the entire nanowire.

4.4 Boron Nitride Nanotubes Revisited

Since ammonia and methane can both be used individually to alter the product of the IL method using MgB_2 , the combination of the two was experimented with using a steady gas flow. The process was the standard IL process discussed in [Section 1.1](#), however, methane and ammonia were each added in the amount of 10 sccm when the reaction temperature was achieved. (Methane doesn't seem to participate in the reaction when using $\text{Mg}(\text{BH}_4)_2$, see [Chapter 3](#). Therefore, the combination of these doping gases was not used with $\text{Mg}(\text{BH}_4)_2$.) This resulted in nanostructures which seemed very similar to the materials which were made without the addition of carbon. They were long, thin nanostructures with diameters near 10 nm and lengths measured in the microns as shown in Figure 4.10. These materials were examined under the TEM.

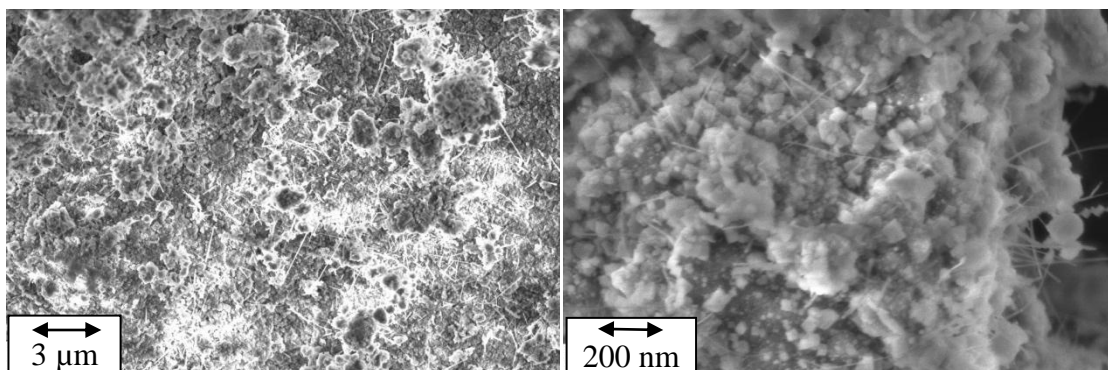


Figure 4.10 (Left) Low magnification SEM image of nanowires made through methane and ammonia addition to the IL method. (Right) Higher magnification image of the same.

The TEM revealed very little initially. This is because when using the normal TEM procedures, the nanostructures were found in large bundles surrounded by amorphous carbon, see Figure 4.11. In an attempt to break up the bundles, ultrasonication was used successfully. The materials were simply horn sonicated in methanol before they were dispersed onto a TEM grid. This seemed to break up the material nicely and help to remove some of the carbon build up.

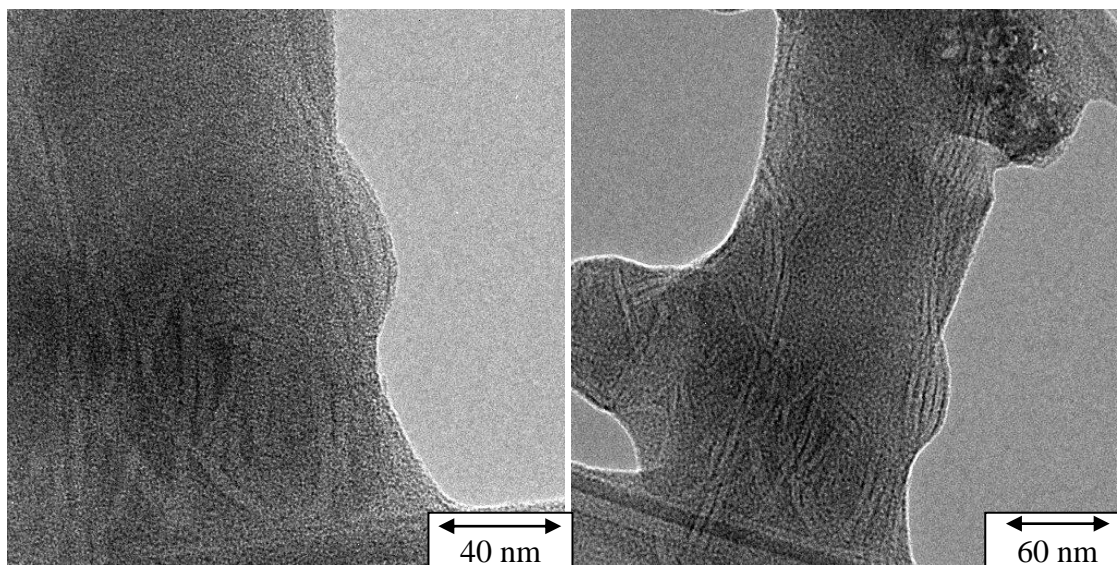


Figure 4.11 TEM images of bundles of nanostructures encased in amorphous carbon.

The result of the addition of ultrasonication is shown in Figure 4.12. Note that the material is layered structures with a very small diameter size. EELS analysis would confirm the material which composed the layered structure was boron nitride. This would mean the material was boron nitride nanotubes, no magnesium was found in the interior, however. Note that there is no darkening of the interior of the nanotubes, as there was in the case with no methane present during the reaction, see [Section 4.1](#). Thus, the presence of methane seems to prevent the magnesium oxide from filling the tube. This also shows the IL process is capable of not only making pure boron nanotubes, but also boron nitride nanotubes. Perhaps through further experimentation, a method to create nanotubes composed of boron joined to boron nitride in regular patterns will be realized.

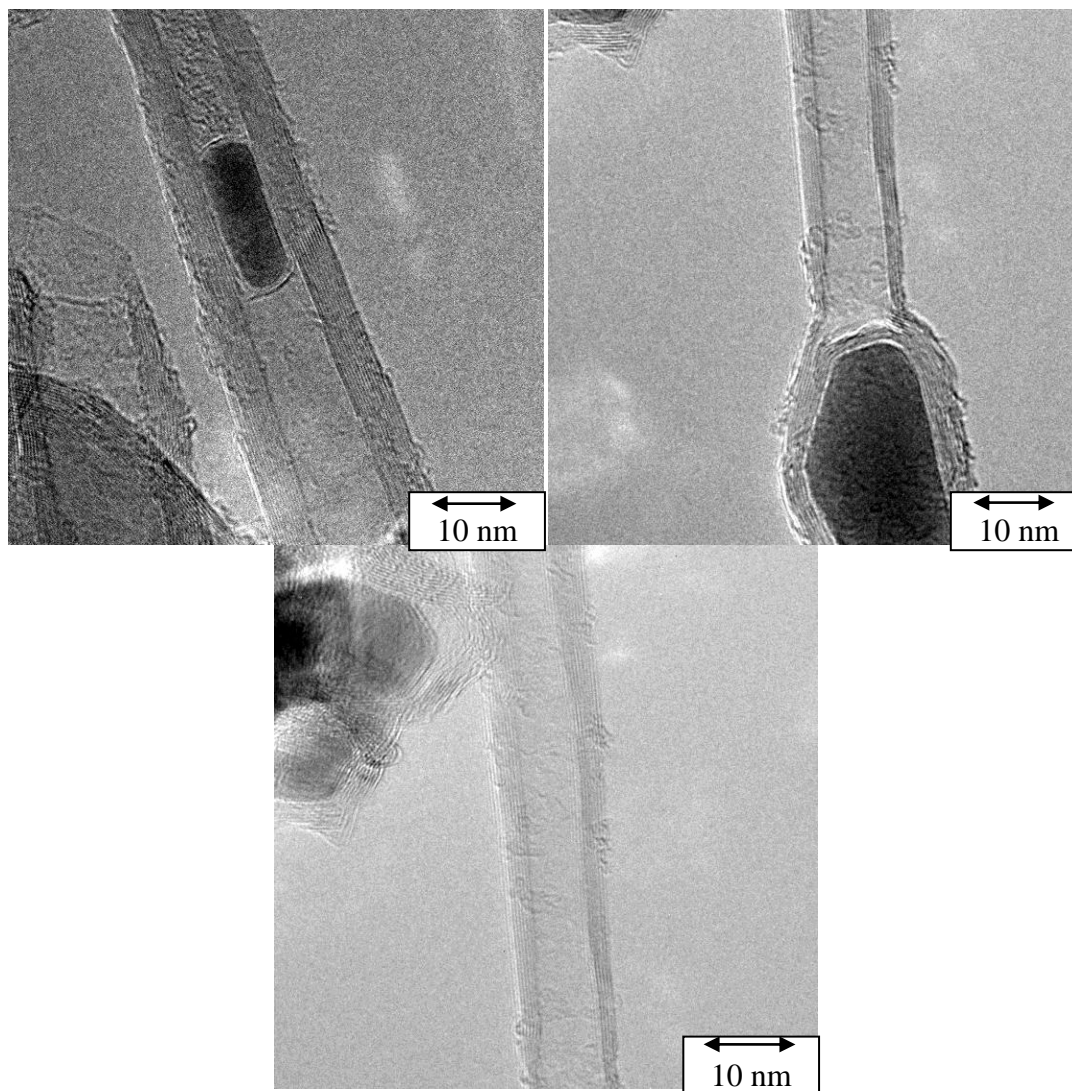


Figure 4.12 TEM images of the nanotubes which result from altering the IL method by doping with methane and ammonia gas and using MgB_2 . The nanotubes are only a few layered, ranging from 4-10 layers, and commensurately have diameters ranging from 10 nm to 20 nm. In this case, there is no magnesium filling. Catalyst particles can be seen on the inside of some of the nanotubes, but they're clearly not filled completely with any material.

In conclusion, the experiments with ammonia revealed that the IL method is capable of making boron nitride nanowires and boron nitride nanotubes. Unfortunately, the boron nitride nanotubes are covered in amorphous carbon which must be removed afterwards. Further experimentation might reveal a method to create the nanotubes using the IL method without the creation of the unnecessary carbon byproduct. From a

perspective of understanding reaction mechanisms, it is highly interesting that the methane essentially can be used to keep the magnesium oxide from filling the nanotube. When only doping with ammonia using MgB_2 in the IL method, the result is magnesium oxide filled BNNTs, however, with the addition of the methane; BNNTs essentially remain the same, except they have no oxide filling. Understanding how the methane does this might reveal some insights into the chemical reactions in this CVD process.

The IL method successfully made novel heterostructures such as boron nitride filled with magnesium oxide and boron nitride-boron nanowires, in addition to homogenous structures. Future experiments could be used to determine a method to reliably create boron nitride-boron nanowires, as the yield in this experiment for that particular heterostructure is quite low. The intermittent doping might be having a regular effect on the structure of the nanowires, because there are visible discontinuities in the structure, but the elemental composition is not altered in the desired manner in the majority of the nanowires. Another problem is that the doping needs to be controlled better in each wire even when it is successful, since as of now, the nitrogen doping is not regular and is spread diffusely in the nanowire. A more interesting material would be one that was composed of boron nitride nanotubes joined to boron nanotubes. This might be possible as the IL method has been shown to be able to make either type of structure, though the growth conditions found to create one material may not readily be used to create the other material because of different catalyst conditions. There certainly might be some variation of the IL system that could easily grow both structures, where switching between either could be done entirely by changing the doping gases. The IL variation most likely to grow boron nanotubes uses MgB_2 with no dopant gases or MCM-41.

Perhaps if ammonia or a combination of ammonia and methane could be used with this particular variation to create boron nitride nanotubes, intermittent doping of the correct gases could create boron nitride-boron nanotubes. The other nanoheterostructure discussed in this chapter was composed of boron nitride encapsulating magnesium oxide. This nanoheterostructure was made readily using the IL process and could be used for blue light emission applications, as the band gap of MgO and boron nitride nanotubes is 7.8 and 5.2 eV, respectively. The yield for this type of heterostructure in the process conditions described is quite high. In general, however, the effect of the many reaction parameters for this variation of the IL method are not well understood, therefore, future experimentation should probably use some sort of design of experiments to elucidate the fine nuances of this process. Overall, the use of ammonia has been demonstrated as an interesting way of altering the IL process, as it increases the number of possible nanostructures dramatically. When using other dopant gases, the number of nanostructures becomes even greater.

CHAPTER 5

EFFECT OF HYDROGEN SULFIDE AND AMMONIA ON THE IL METHOD

5.1 Nanorods and Nanowires from Ammonia and Hydrogen Sulfide

As shown in [Chapter 4](#), ammonia by itself can have a dramatic affect on the IL method. The addition of ammonia introduced the ability to synthesize several new nanostructures to the IL method. Intriguingly, sulfur is known to have dramatic effects on boron nitride structures [70-72]. Sulfur itself would not be useful for the IL method, because boron sulfides have melting points below that of the normally used reaction temperatures, meaning nanostructures composed of boron sulfides could not be formed using this process. Therefore, the IL method with MgB_2 and $\text{Mg}(\text{BH}_4)_2$ was modified with the addition of 20 sccm of ammonia and 10 sccm of hydrogen sulfide when the reaction temperature was achieved. Since a large amount of reactant gases are present, the argon gas flow was doubled, otherwise, it is the same process described in [Section 1.1](#).

SEM images of the product which results with the addition of hydrogen sulfide and ammonia using MgB_2 in the IL method is shown in Figure 5.1. The sample is covered in nanorods (some might argue they are nanowires, but the semantics specified for the purposes of this dissertation would define them as nanorods, see [Section 1.2](#)). The nanorods have diameters of 100 nm and lengths measured in microns. The catalyst at the tip of each sample is evident, indicating a vapor-liquid-solid (VLS) method is the growth mechanism of these structures. (In VLS synthesis, the catalyst is a liquid droplet at the reaction temperature. When reactant gases flow across the catalyst, they dissolve into the liquid catalyst and convert into a solid nanomaterial.) The result when using the same

conditions except with $\text{Mg}(\text{BH}_4)_2$ was clearly different. These are very thin nanowires, as shown in Figure 5.2. The yield for both cases was moderate. SEM analysis was successful, so TEM analysis was conducted.

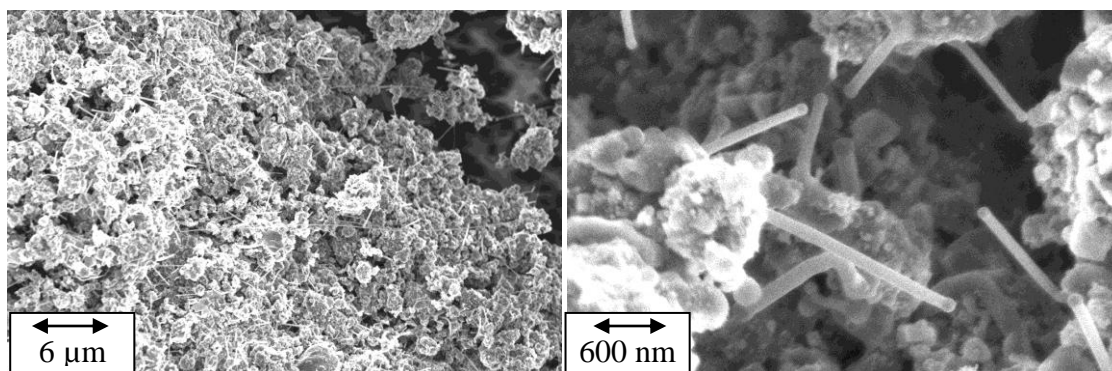


Figure 5.1 (Left) Low magnification SEM image of the result of adding ammonia and hydrogen sulfide to the IL method with MgB_2 . Note that relatively thick nanorods appear to cover the sample. (Right) High magnification SEM image of the same showing the nanorods have diameters of roughly 100 nm and lengths in the microns. A thick catalyst head is visible at the tip of each of the nanostructures.

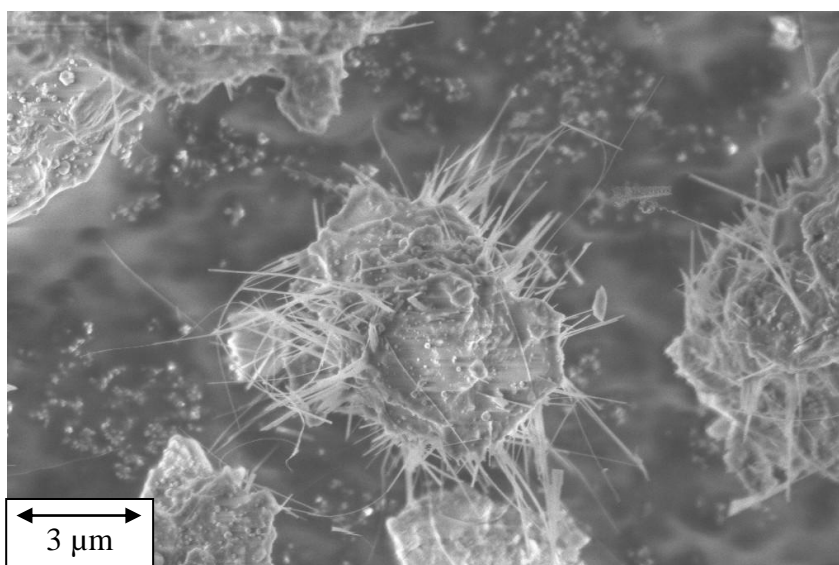


Figure 5.2 SEM image of the product which results when adding ammonia and hydrogen sulfide to the IL method with $\text{Mg}(\text{BH}_4)_2$. Long thin nanowires are growing from the sample at a moderate yield.

TEM analysis on the product of using the IL method with MgB_2 , ammonia, and hydrogen sulfide was conducted as shown in Figure 5.3 to 5.5. The nanorods which resulted are somewhat disordered, though they are still clearly crystalline, as visible in the TEM. The disorder comes from a number of ‘kinks’ keeping the nanorods from growing straight. The catalyst is evident in the tip by Z contrast. While high resolution TEM was difficult on such a disordered sample, a highly crystalline area was found and crystal spacings of 0.60 nm and 1 nm were measured using fast Fourier transform analysis and plots of the contrast found in the image. EDX and EELS analyses were conducted which indicated the material was primarily boron with magnesium and sulfur impurities. Fascinatingly, no nitrogen was found in the sample.

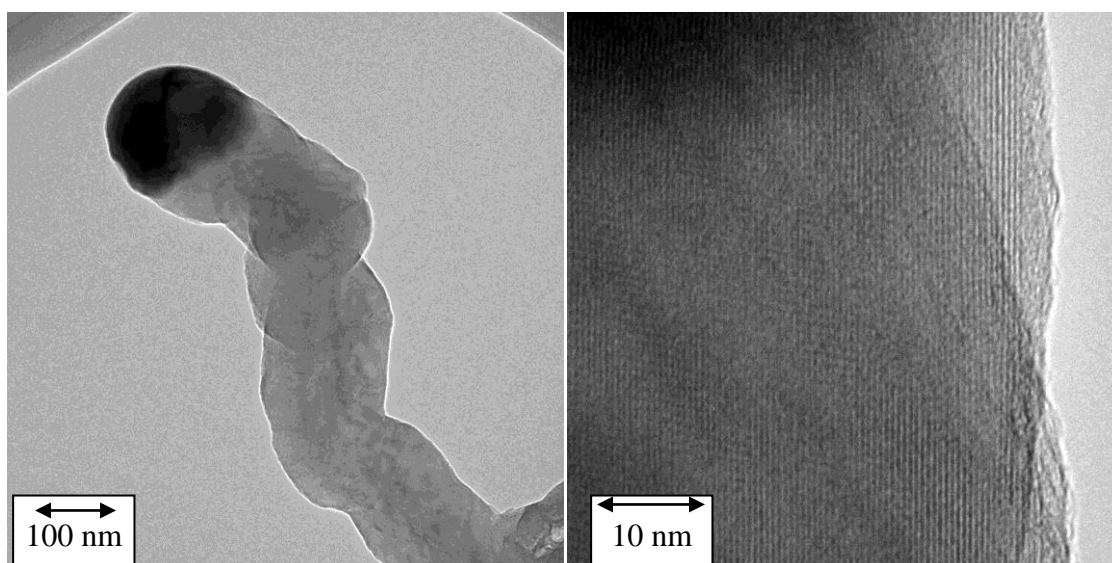


Figure 5.3 (Top left) Low resolution TEM image of a nanorod which results from the IL variation using MgB_2 with the addition of hydrogen sulfide and ammonia. Note that the nanorod is thick and short compared with other nanostructures discussed in this dissertation and has a number of ‘kinks.’ (Top right) Typical HRTEM image of the nanorods, the ‘kinks’ make in depth analysis difficult.

Combining all of the data shows these are most likely doped boron nanowires, where the dopants seem to change the allotrope and induce the disordered kinks found in the structure. The spacings are similar to those reported previously in literature for an orthorhombic boron nanowire [73], but not the same as the high temperature high pressure orthorhombic boron reported in 2009 [74]. The crystal does seem to have different spacings than the product when there are no dopants present. CBED analysis was conducted, though it only revealed the sample was somewhat disordered. The product created using the same reaction conditions except replacing $\text{Mg}(\text{BH}_4)_2$ with MgB_2 results in an entirely different material, which is clear when looking at the results from the TEM analysis.

TEM analysis was conducted on the ILY variation using $\text{Mg}(\text{BH}_4)_2$ with hydrogen sulfide and ammonia, see Figures 5.6 and 5.7. The result of this process is clearly long nanowires with diameters ranging from 20-40 nm and lengths well into the microns. The structure is highly ordered and crystalline. CBED, SAED, and FFT analysis all indicate the crystal spacings of nanowires are 0.28, 0.35, and 0.50 nm. EDX and EELS analysis revealed a 2:1 atomic ratio of boron and magnesium. Both the crystal spacings and the elemental analysis indicate the nanowires found are MgB_2 [75, 76]. (MgB_2 actually has a crystal spacing of 0.30 nm, not 0.28 nm, this discrepancy is either due to error or may be indication of some crystal distortion, though why it affects one crystal spacing and not the others is problematic.) MgB_2 is a material with known superconducting properties, which makes it highly exciting [75, 76]. Also of interest, MgB_2 has a hexagonal crystal phase, like carbon and boron nitride, though it is not the same as the graphitic structure.

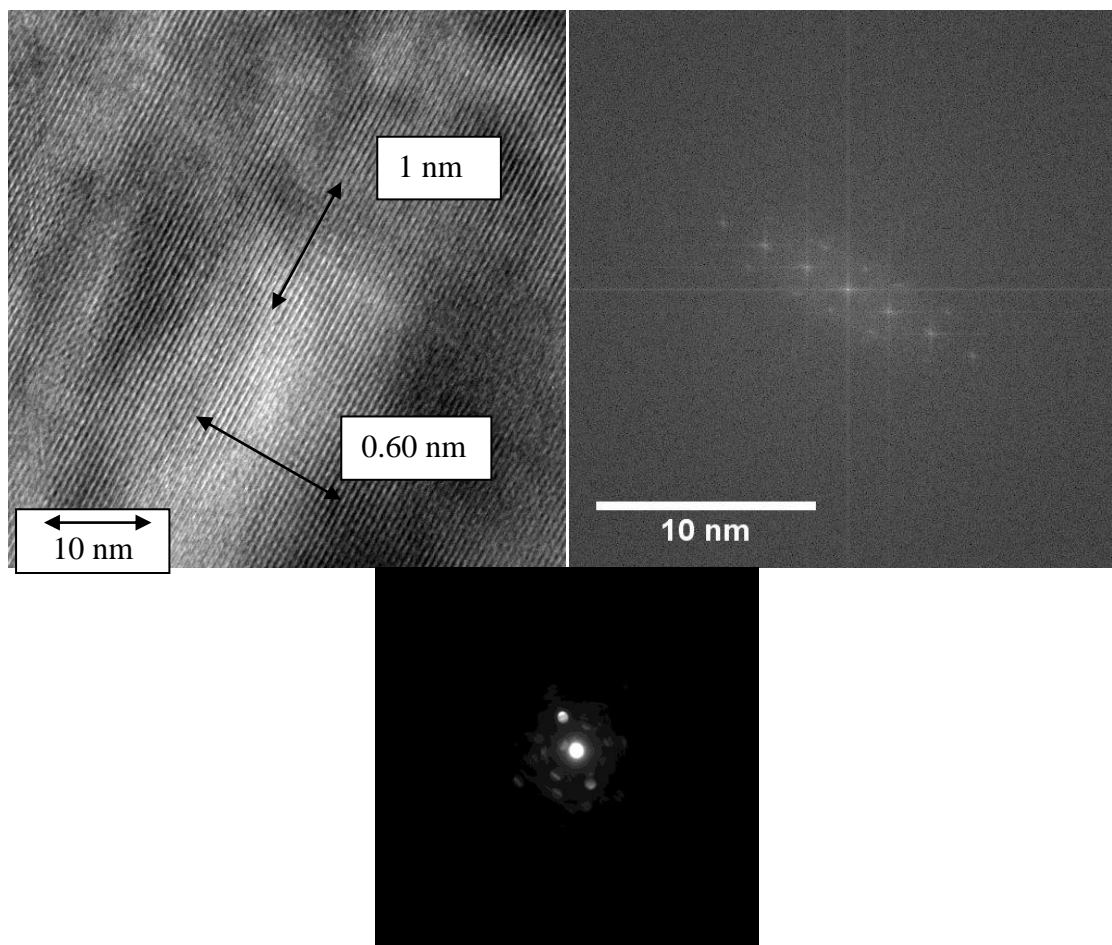


Figure 5.4 (Top left) HRTEM image of a particularly crystalline area of the sample, here crystal spacings of 0.60 nm and 1 nm were measured (contrast plots used for the measurement are given in Figure 5.5). This part of the sample may not be representative because it was difficult to find, however analysis on it was the most reliable because of the high resolution possible. (Top right) FFT of the highly crystalline area, used to confirm measurements of crystal spacings. A masked image is given in Figure 5.5 where spacings are easier to interpret. (Bottom) CBED of the sample, spacings are difficult to measure, but this does show the sample is kinked heavily.

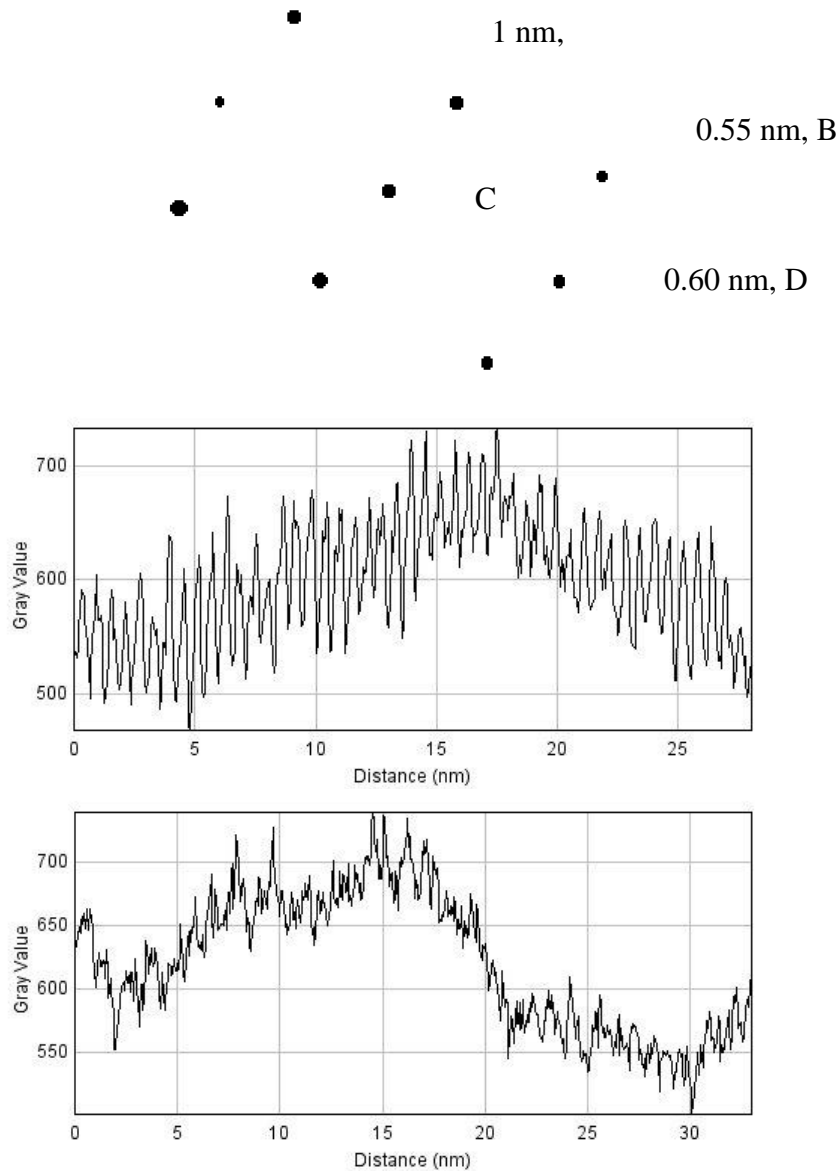


Figure 5.5 (Top) Masked FFT image based on FFT image from Figure 5.4. Spacings of 0.55, 1, and 0.60 nm are shown, which are measured from the point to the center in the image. Note that $\angle DCB = 33^\circ$ and $\angle BCA = 48^\circ$. (Middle) Contrast profile plot confirming 0.60 nm crystal spacing. (Bottom) Contrast profile plot going in nearly perpendicular direction to previous profile, showing crystal spacing of 1 nm.

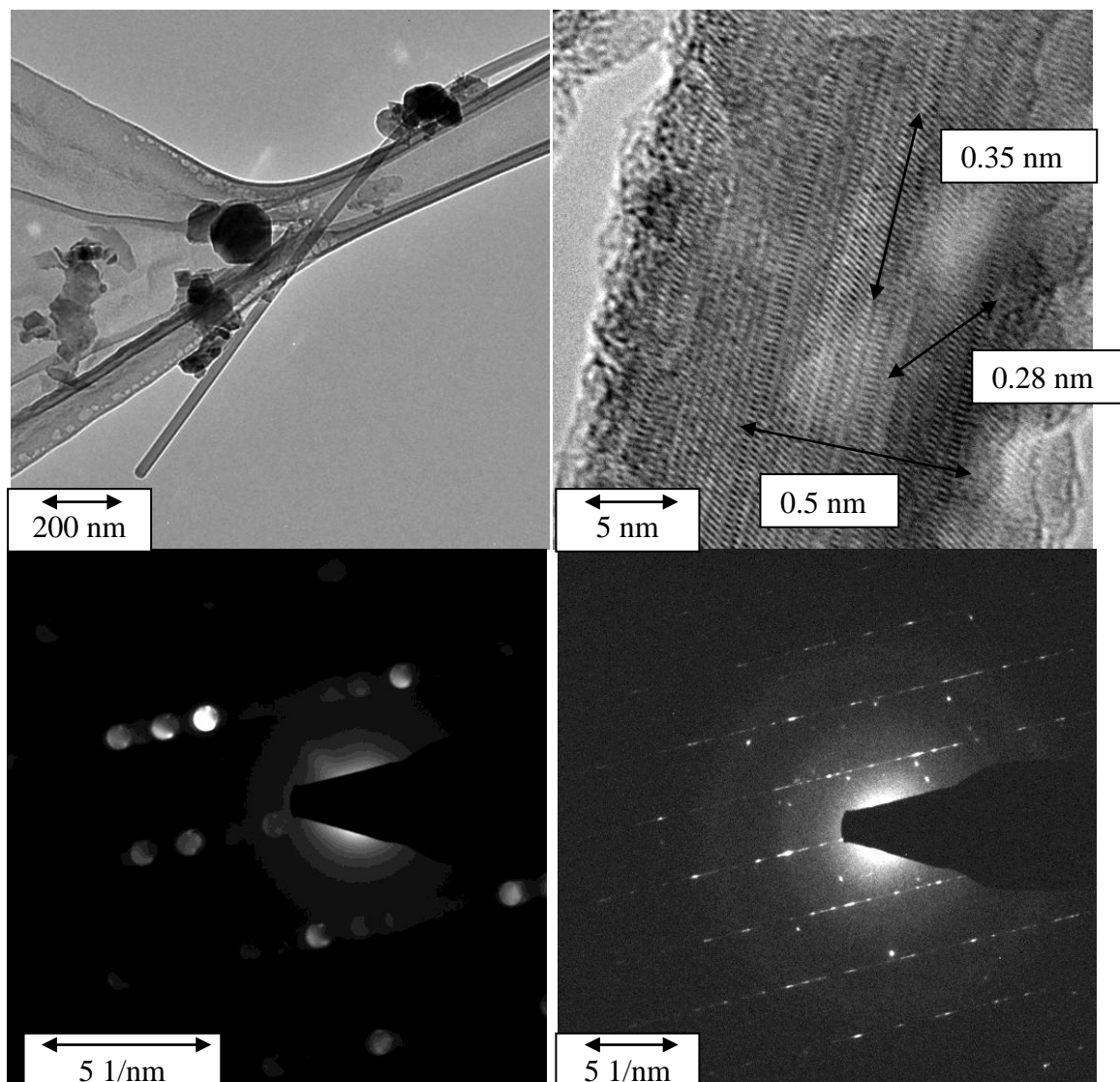


Figure 5.6 (Top left) TEM image of a long thin nanowire, note that it has a long aspect ratio and appears undamaged. (Top right) HRTEM image of same nanowire, it is 20 nm in diameter and possesses a highly ordered crystal structure. The direction and size of the crystal spacings calculated from the FFT analysis given in Figure 5.7 are displayed. (Bottom left) CBED and (Bottom right) SAD pattern of same nanowire, used to confirm the crystal spacings.

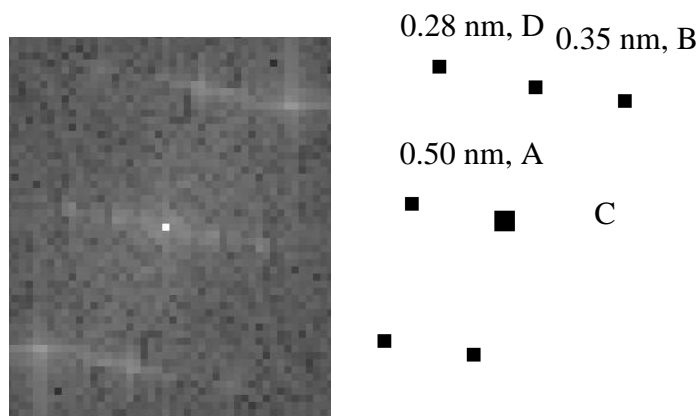


Figure 5.7 (Left) FFT image of HRTEM found Figure 5.6. (Right) Masked FFT image for ease of analysis. The corresponding crystal spacings are given and $\angle BCD = 35^\circ$ and $\angle ACD = 55^\circ$.

The IL variation of adding ammonia and hydrogen sulfide has yielded two interesting nanostructures. When using $Mg(BH_4)_2$, long thin nanowires of MgB_2 are created, a known structure [77]. MgB_2 is a well known and thoroughly characterized superconductor, which could have a great number of applications because MgB_2 is relatively inexpensive. MgB_2 has a non graphitic, but still hexagonal structure, hinting that the IL method tends to favor the growth of hexagonal materials. Coincidentally, using $Mg(BH_4)_2$ with the aforementioned dopant gases results in a nanowire analog of the other catalyst/reactant utilized, MgB_2 . Whether this is actually pure coincidence or is revealing something deep and important about the IL method is still conjecture. Also of interest is why the MgB_2 and the $Mg(BH_4)_2$ even result in different materials, because the $Mg(BH_4)_2$ creates MgB_2 nanowires, which are presumably even more reactive than bulk MgB_2 . The reaction should proceed further to create the same material as if one started with MgB_2 . Perhaps if the reaction was simply run longer it would result in the nanorods found when starting with MgB_2 , but considering how quickly VLS growth occurs this seems unlikely. The other difference is the reaction with MgB_2 is done at a higher temperature, which could explain the different structures as well.

When using MgB_2 with ammonia and hydrogen sulfide in the IL method, the result is highly distorted, but still crystalline, doped boron nanorods. These nanorods have crystal spacings different than the structure which results when using no dopant gases. The closest match to the crystal spacings that was found in literature indicates these are orthorhombic boron nanowires [73]. In the reference, they were also grown using a CVD process. Orthorhombic boron has been reported, but it was synthesized at a temperature of 1800°C and a pressure of 9 GPa [74], and its reported spacings are different from reference [73] and those that will be reported [Patel et al. to be published].

A tenuous, though tantalizing, possibility is that CVD allows for a simple and economical method of synthesizing orthorhombic boron. The obtained structure is different than the phase which results from the high temperature high pressure experiments. In the experiments of this dissertation, the presence of the hydrogen sulfide and ammonia not only changed the obtained polymorph, but also cause some doping of the structure. The presence of some dopants (magnesium and sulfur) is highly likely, as they are detected in elemental analysis and explain the ‘kinks’ in the structure, though the quantity of the dopants is unknown. This is because the EDX data was considered fine for qualitative analysis, but not for high accuracy quantitative analysis. (In reference [73], no kinking is reported. This could be because the nanostructures reported in literature are either not doped, or doped in a different manner).

The affect the dopants and ‘kinking’ have on the electrical properties of the nanorods would be fascinating to study. The alteration of the IL process by using sulfur and nitrogen should be considered a success, as two nanostructures were created, one is a

well known and exciting superconductor, and the other is doped boron nanorods which could have useful electrical properties.

5.2 Boron-Sulfur-Carbon Nanosheets

Using the IL method with the MgB_2 and the addition of methane to induce carbon doping results in a novel nanoheterostructure, see [Chapter 3](#). Flowing in hydrogen sulfide to induce sulfur doping is also known to cause interesting effects in the IL method, as seen in the [previous section](#). Furthermore, sulfur is a known promoter for the synthesis of CNTs and carbon fibers [78-80], although the reasons why are currently unknown. (Possible explanations include lowering of the melting point of the catalyst or interaction with CNTs as they grow, thereby lowering the free energy.) Therefore, the combination of methane and hydrogen sulfide was used with MgB_2 in the IL method to investigate whether novel structures would result from the addition of carbon and sulfur. The flow rate of methane and hydrogen sulfide was 20 sccm and 10 sccm, respectively, and the argon gas flow was doubled to 200 sccm, but otherwise it is the same as process described in [Section 1.1](#).

The outcome from this variation of the reaction was rather surprising. SEM images of the product are given in Figure 5.8. The material seems to be sheets with large areas which grow stacked on top of each other. The sheets clearly had a number of folds which appeared to be ‘veins’ in the SEM image. This is clearly a different material than graphene, its analogs, or boron nanoplatelets, though there is a morphological similarity. The thickness of the sheets is difficult to determine from SEM, but they are clearly thin.

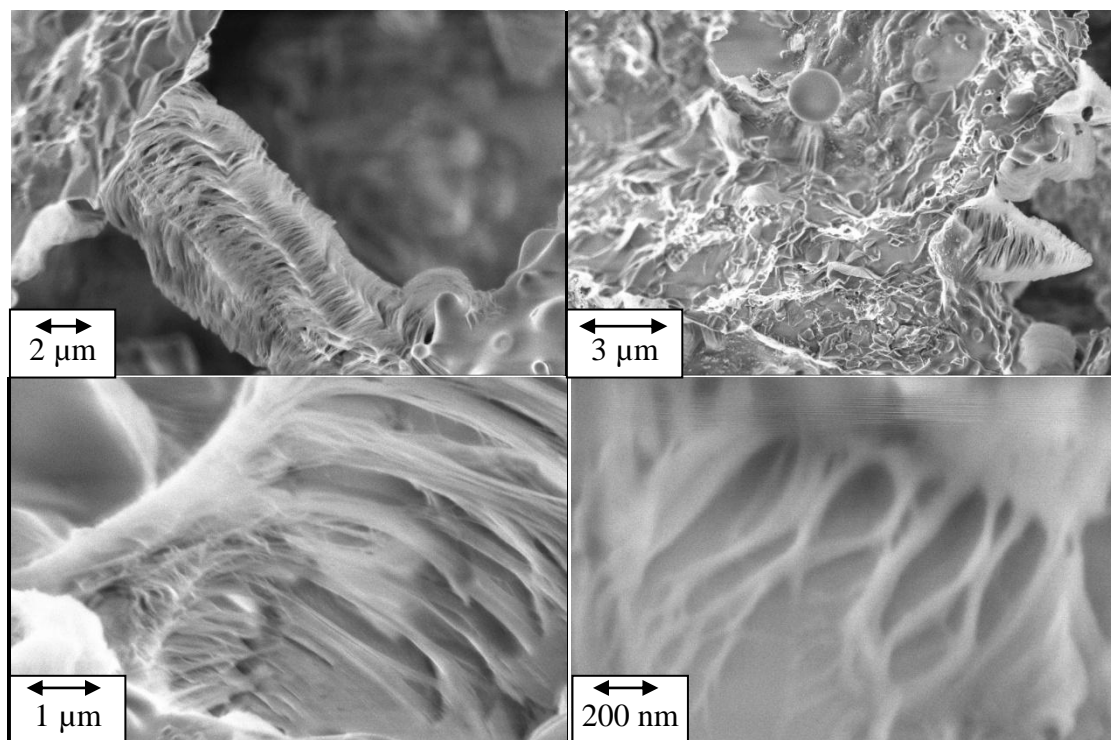


Figure 5.8 SEM images of the product which results when adding methane and hydrogen sulfide to the IL method with MgB_2 . (Top left) Dramatic example of the stacking which occurs with this material. (Top right) The sheets could sometimes stack in a pyramiding fashion. (Bottom left) High magnification image of stacking sheets. (Bottom right) Folds evident in the sheets.

TEM analysis revealed interesting information about the sheets. This is the first nanostructure of the IL method not connected with the catalyst/unwanted product, which means it can easily be separated. When preparing the TEM grid, the material was placed in a vial with methanol which was hand agitated. The heavy materials fell to the bottom while the nanomaterial stayed in suspension much longer. The nanomaterials were decanted and dropped onto the TEM grid. TEM images of the folded sheets are given in Figure 5.9. TEM confirms these materials are highly folded large area sheets. The TEM also shows that these materials are extremely amorphous, with almost no crystal order. Due to issues with carbon contamination, an accurate thickness determination could not be made. EELS and EDX analysis indicate these materials are carbon and boron with a

small amount of sulfur, nickel and magnesium. Since this material could easily be purified, optical microscopy was performed.

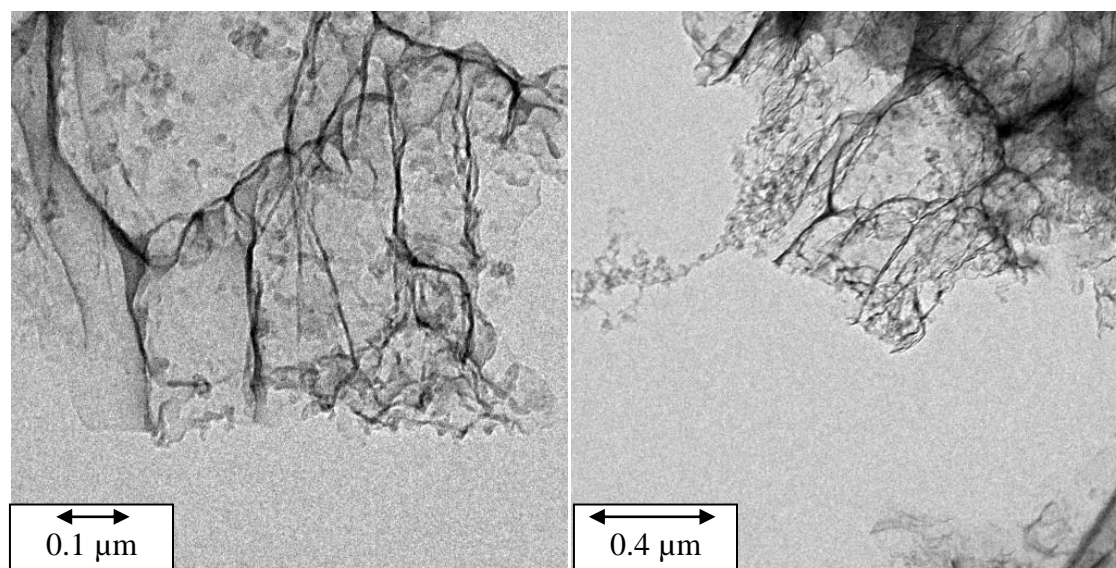


Figure 5.9 TEM images of the amorphous flakes which result from adding hydrogen sulfide and methane to the IL method using MgB_2 .

The polarized optical microscopy on the sample is given in Figure 5.10 at 1500 times magnification. The sheets seem to be able to group together in large, easily visible structures. In transmission mode, the sample is clearly transparent with a number of pores. In reflective modes, the sample displays a strange pattern, reminiscent of diffraction. There is a dark spot in the middle of each structure, which is surrounded by different colors of light.

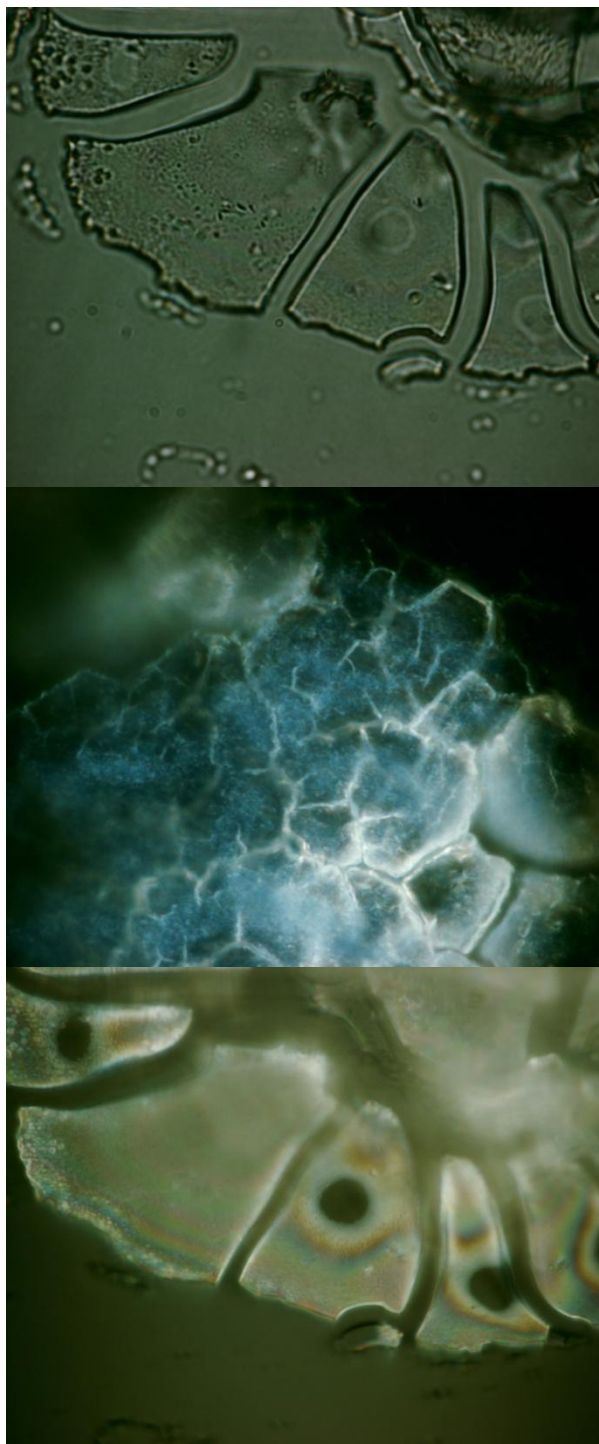


Figure 5.10 Optical images of the stacked sheets: (Top) transmission mode (Middle) reflective mode, and (Bottom) normal.

Raman and FTIR spectroscopy were performed on the sample. The sample showed Raman lines from 500 cm^{-1} to 1200 cm^{-1} . There were broad, small peaks at 566 ,

796, and 1108 cm^{-1} . The FTIR and Raman indicate there are irregular, B-C, S-S, C-S, and C-C bonds in the material, which corroborate spectroscopic analysis performed in the TEM. The Raman activity near 566 cm^{-1} can be related to the following, which all have Raman activity near that area: C-C, S-S, B-C and C-S bonds. The 1108 cm^{-1} peak is a possible sign of C-S double bonds. The 796 cm^{-1} peak is a sign of B-B bonds. [81-84].

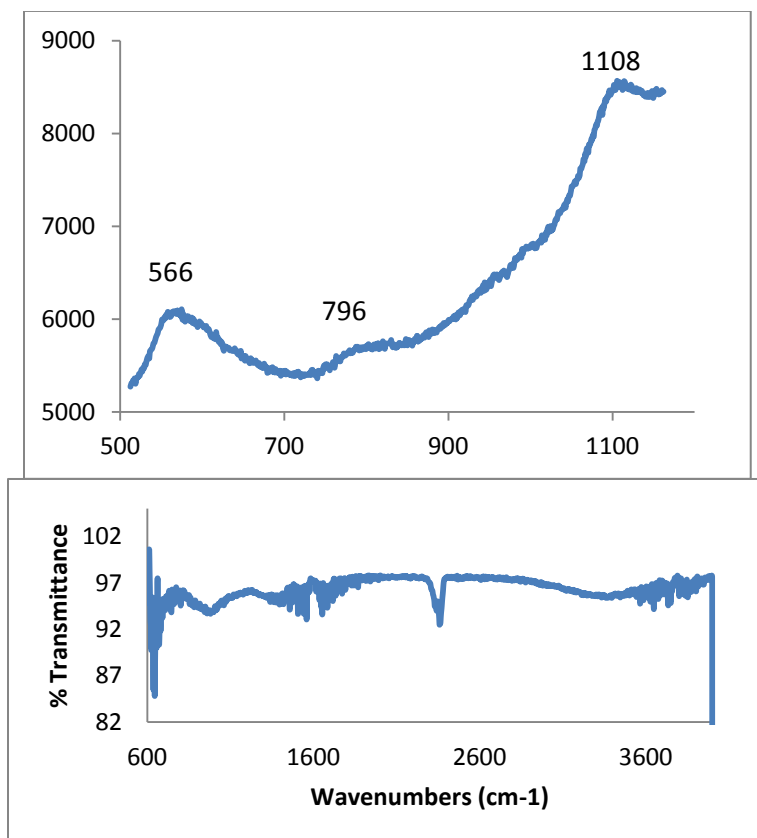


Figure 5.11 (Top) Raman and (Bottom) FTIR spectra of the amorphous sheets which result.

The result when using MgB_2 created a dramatic new nanostructure. Complete understanding of this novel nanostructure is needed, but initial experimentation revealed some critical details. For example, there was interest in varying the method to further understand the growth mechanism of the sheets. The most obvious variation is trying to use $\text{Mg}(\text{BH}_4)_2$ instead of MgB_2 . Another important variation was to remove the MCM-

41 from the reaction. The MCM-41, basically just porous silicon, in principal, gives a template which can be used to encourage the growth of nanowires and nanotubes.

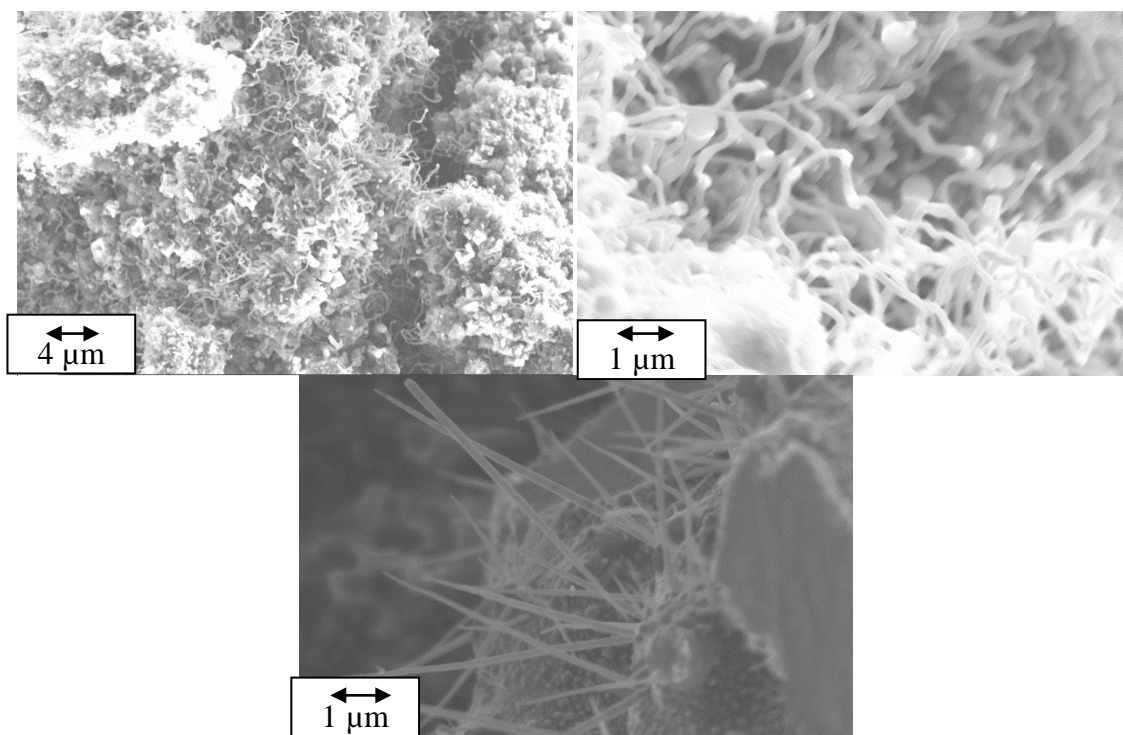


Figure 5.12 (Top left and right) Low and high magnification (respectively) images of nanostructures which result from the IL method using MgB_2 with no MCM-41. They appear to be some sort of nanofiber with a distorted morphology. (Bottom) Nanostructures found in product of IL method using $\text{Mg}(\text{BH}_4)_2$ with methane and hydrogen sulfide.

Obviously, the result from this experiment is not benefiting from templating, at least in a direct manner, because they're sheets and not fibers. Removing the MCM-41 has successfully encouraged the growth of boron nanotubes [Patel et al., to be published], so there is precedent its removal can cause desirable changes. The final variation that was attempted was to add ammonia (at 20 sccms) to the process which successfully grew the sheets. Ammonia is known to have a dramatic influence on the IL method, and therefore, it was assumed that it could have an exciting affect on the growth of the sheets. The aforementioned variations were attempted and the results are shown in Figure 5.12.

Figure 5.12 shows the nanostructures which result when using the IL method with no MCM-41 and with MgB_2 , methane and hydrogen sulfide. The material seems to be long, distorted nanofibers, which grow at a fairly high yield. The diameters of these structures are roughly 100 nm and they have lengths well into the microns. In contrast, when using $\text{Mg}(\text{BH}_4)_2$, hydrogen sulfide, and methane in the IL method, long straight nanofibers seem to result. They have diameters ranging from 50 nm to 100 nm and large aspect ratios. EDX analysis revealed these materials are composed of pure carbon. Carbon materials can be easily analyzed using Raman spectroscopy. The Raman spectra of both types of nanowires are shown in Figure 5.13. This shows that both of these variations create MWCNTs, though they are morphologically different. Sulfur is a known promoter of CNT growth, so these results are not entirely surprising. The final variation was to use the IL method with MgB_2 and the following dopant gases: ammonia (20 sccm), methane (20 sccm), and hydrogen sulfide (10 sccm). This alteration, which uses all of the available dopant gases with MgB_2 , results in no observable nanostructures. The significance of these experiments is no modification results in the folded sheets which were observed previously, and they also demonstrate the IL method can create pure carbon nanotubes easily.

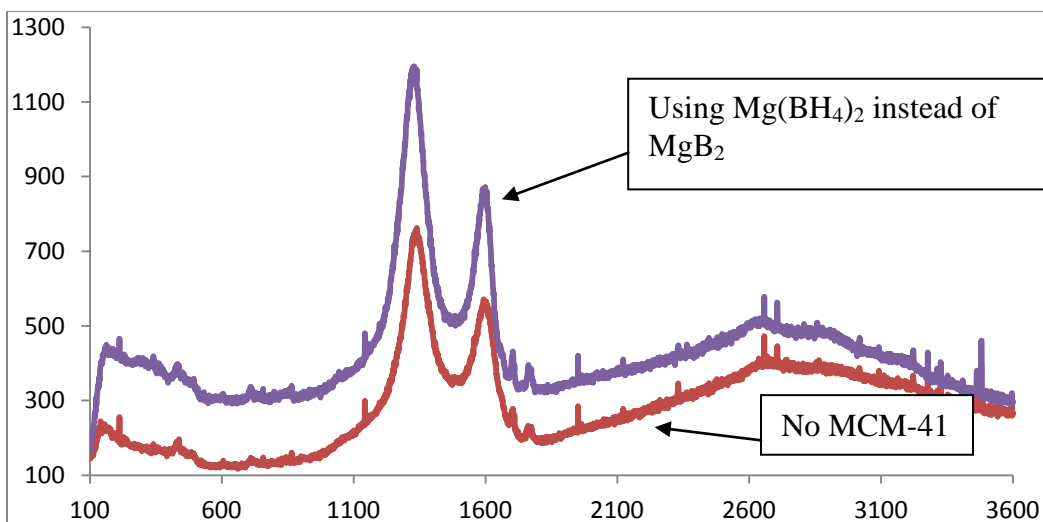


Figure 5.13 Raman spectra of the products which result when performing the IL experiment with MgB_2 (no MCM-41) and $\text{Mg}(\text{BH}_4)_2$ with flowing methane (20 sccm) and hydrogen sulfide (10 sccm). They both appear to be MWCNTs with a moderate amount of defects.

In closing, use of methane and hydrogen sulfide in the IL method can cause the creation of a novel nanostructure, the thin folded sheets. These sheets are amorphous in structure, and are primarily composed of boron, carbon, and a small amount of sulfur. They are several square microns in area and are very thin, easily below 5 nm and possibly even as thin as 1 nm. The growth mechanism most likely is based on a VLS mechanism and follows an onion or flower model (discussed in [Appendix A](#)), where reactant gases diffuse into a liquid catalyst particle until super saturation is achieved. At this point, the sheets grow from the material. The sheets can be observed in stacking patterns, meaning that once a sheet is formed, another can be formed right away, unlike in the growth of nanowires and nanotubes, where generally a catalyst particle can only grow one structure. In the case of pyramid stacked sheets, the first sheet which grows is small, but as the catalyst particle it grew from ripens, subsequent sheets which grow become larger in area.

The existence of the folds is difficult to explain, especially as the sheets are amorphous, which would imply they're brittle. Much more in depth analysis will be required to explain the folds. These sheets can be easily removed from the other products of the reaction, which make them the most straight forward for further analysis and possible scale up, if they find some useful application. An exhaustive search of phase diagrams shows that boron and carbon normally in these ratios splits in boron carbide and graphite, which shows that this is not only a new nanostructure, but a new material all together. The sulfur may act to stabilize the amorphous phase.

The variations attempted on the method which grew the folded sheets did not result in novel nanostructures. Using $\text{Mg}(\text{BH}_4)_2$ instead of MgB_2 , results in thick, straight MWCNTs while removing the MCM-41 results in thick, highly curved and distorted MWCNTs. The addition of ammonia results in no nanostructures at all. Therefore, while the MCM-41 does not actually act as a template, it must participate in some way in the reaction to encourage the growth of the sheets. Also, the $\text{Mg}(\text{BH}_4)_2$ cannot be used to replace the MgB_2 in the process. (At this point, one should realize that MgB_2 and $\text{Mg}(\text{BH}_4)_2$ are in no way interchangeable as there is no known variation of the IL method where both catalyst/reactants give the same material.) Hydrogen sulfide and methane as a combination have contributed greatly to the IL family of reactions, as they not only result in a novel nanomaterial, but also allow the creation of CNTs with the correct precursors.

Further experimentation will reveal how the CNTs diameters, quality, and yield can be improved. More interestingly, the critical growth parameters of the sheets should be identified, and their electrical properties should be characterized. The novel sheets are

not entirely unique, as there are methods which may create similar materials, as discussed in the next section. This raises the tantalizing prospect of creating heterostructures with the two types of sheets.

5.3 Boron Nitride Amorphous Nanoflakes Doped with Sulfur

Boron nitride nanotubes (BNNTs), display a number of fascinating properties, especially for electrical applications. This is because unlike CNTs, the electrical properties of BNNTs are not dependent on chirality, meaning each BNNT has a very similar conductivity and band gap. BNNTs have a high bandgap, near 5.2 eV, making them inherently useful for applications such as UV-blue light optics. To be useful for more applications, they must be able to be doped. Doping would allow one to carefully control the electrical properties of the BNNTs, making them useful for transistor applications, and it would also enable the narrowing of the wide bandgap of BNNTs, greatly increasing their utility.

Doping of BNNTs was attempted but not by using the IL method. This is because the IL method can frankly only make pure BNNTs in a convoluted manner ([Section 4.4](#)), among other reasons discussed in [Chapter 1](#). An alternative method was employed which used no metal catalyst, as described in [Section 1.4](#). This method was considered desirable as it would result in BNNTs with no metal impurities, which would be useful for electromagnetic characterization. Doping proved to be highly difficult; however, there was success in a surprising, but qualified, manner in one case.

The original method used to grow BNNTs was derived from literature [85], and before any attempt to dope proceeded, the method described in the literature was

repeated. The first step of the process involves mixing an aqueous solution of boric acid and melamine (molar ratio 2:1) to create melamine diborate. The melamine diborate is then calcined in air at 500° C for 3 hours, and then placed into the carbon crucible of the reaction vessel. The melamine diborate is then subjected to flowing N₂ (at a rate of 60 sccm, the set up used could not emulate the gas flow rate from literature, 1 l/min) at 800° C for 1 hour, which creates an intermediate product, B₄N₃O₂H. The reaction chamber was then quickly heated to 1700° C, and a white vapor was observed in the reaction vessel. The method used to create BNNTs and dope them required extremely high reaction temperatures, in some cases, up to 2200° C, and so could not be performed in the reaction furnace used for the IL experiments. A model of the reaction vessel and an actual picture are shown in Figure 5.14.

After two hours, the reaction vessel was allowed to cool. As the vessel cooled, a white substance coalesced on the interior quartz walls of the reaction vessel. This product was collected in addition to the material which was found in the carbon crucible, i.e, the material which did not evaporate. The product found in the crucible was morphologically similar to nanorods (see Figure 5.15), but the material which evaporated and was found on the interior of the reaction vessel was much thinner and could have been nanotubes (Figure 5.16). For future experiments, the material on the wall of the reactor was only studied because it was assumed to be the location of the nanostructures of interest.

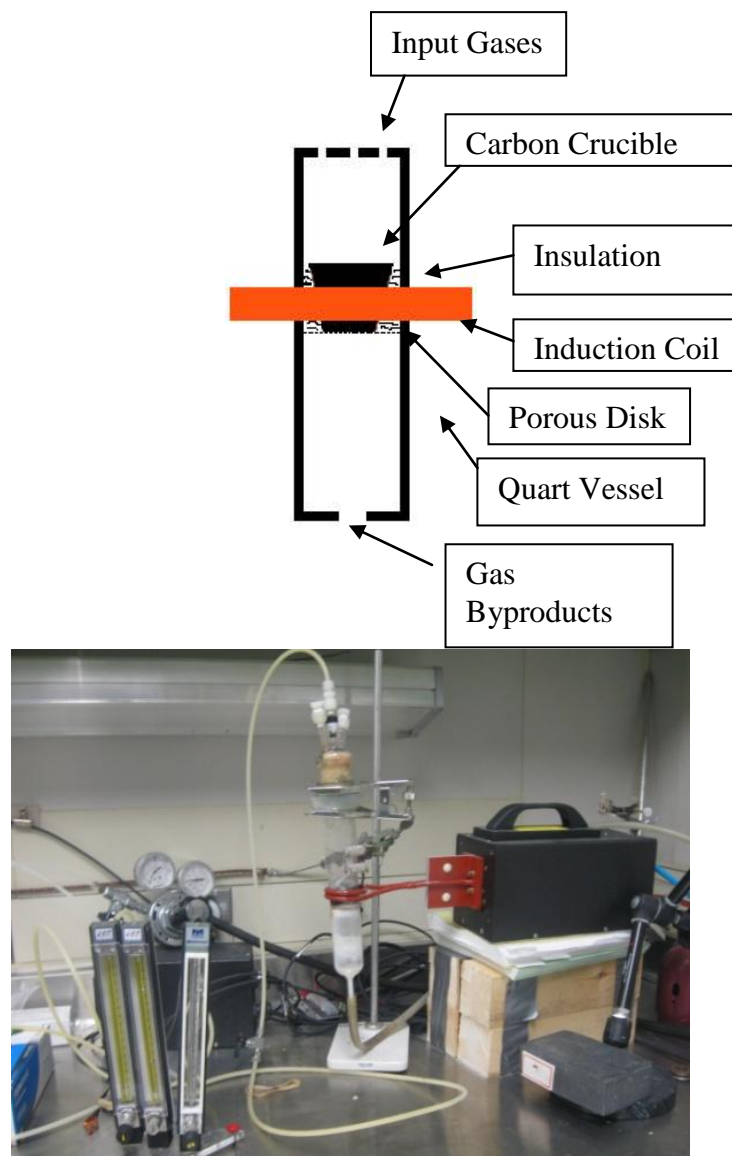


Figure 5.14 (Top) Model of the CVD set up used for these experiments. (Bottom) Picture of CVD set up used for the high temperature reactions needed for the doping of BNNTs. A carbon crucible was heated with an Ameritherm Induction heater. The crucible was sheathed in layers of yttria stabilized zirconia felt and was held up by a porous disk of quartz. The entire reaction chamber was made of quartz.

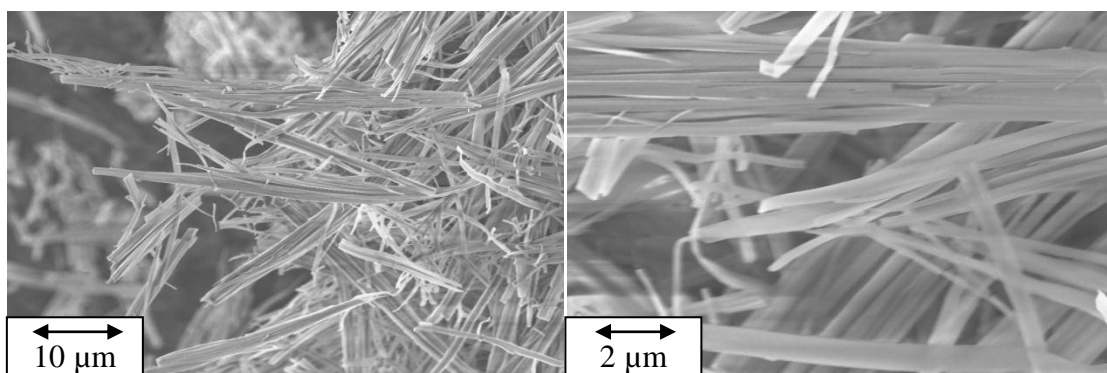


Figure 5.15 SEM images of the material found in the carbon crucible when trying to recreate the original conditions described in literature. The material appears to be thick nanorods, 100 nm to 500 nm in diameter and microns in length.

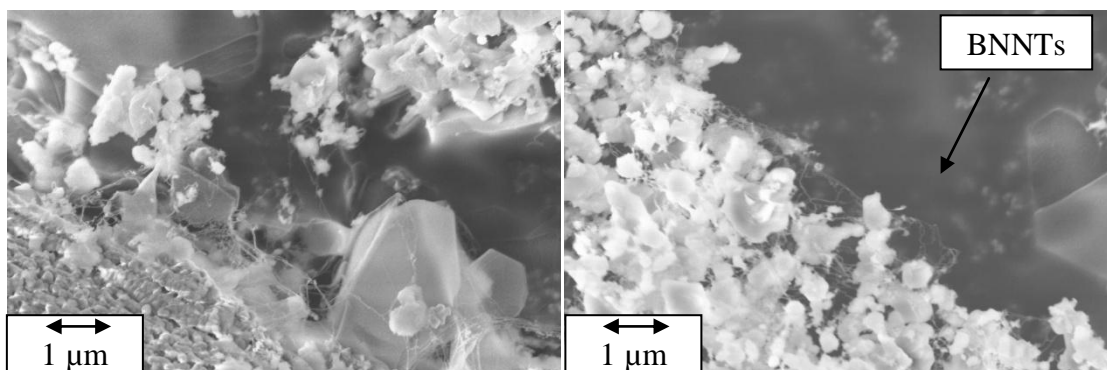


Figure 5.16 SEM images of the material found on the sidewalls of the reaction vessel. The thin fibrous material was presumed to be boron nitride nanotubes.

Satisfied that the material found on the walls of the reaction contained the boron nitride nanotubes as described in literature, attempts to dope the material were conducted. Several dopants were chosen. Chlorine was considered a viable dopant because fluorine has been used to successfully dope boron nitride structures in the past [86,87], but was considered too dangerous to work with. Manganese was chosen as another possibly exciting dopant, as manganese doped boron nitride structures could have some use as dilute magnetic semiconductors [88,89]. Carbon was also considered, because it had the likeliest chance of success and carbon doping is a known way to increase conductivity of BNNTs, see [Section 1.7](#). Finally, altering the stoichiometric ratio of nitrogen and boron

was seen as a possibly viable method of doping, as recent modeling work shows this might be a way of obtaining better conductivity and possible ferromagnetism, making them useful for spintronic applications [90]. Sulfur was also deemed interesting, but will be discussed later.

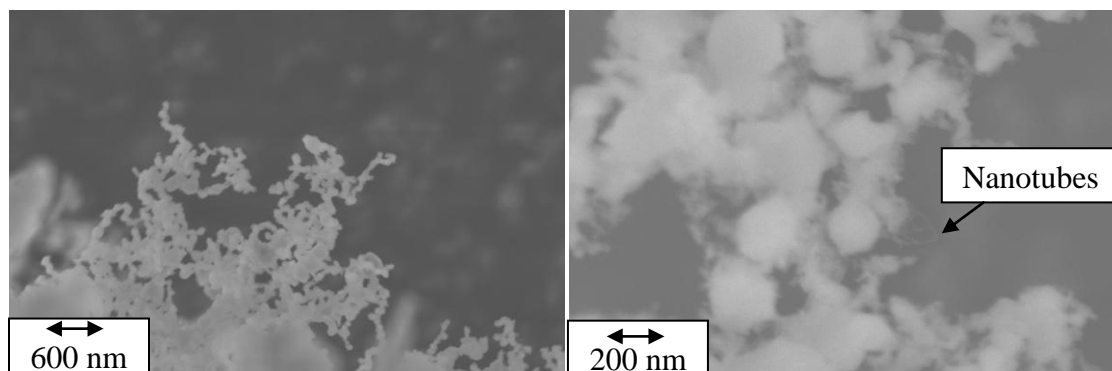


Figure 5.17 (Left) SEM image of possible nanostructure which resulted from manganese doping of BNNTs. The material appears to be a damaged nanostructure. (Right) SEM image showing the results of the carbon doping experiment, where methane was added to the experiment. The result seemed similar to product obtained from simply repeating the literature process. The thin fibrous material could be some sort of doped nanotube, but this could not be confirmed.

Chlorine doping was attempted by introducing BCl_3 at a rate of 10 sccm into the reaction. This failed to produce any sort of discernible nanostructure at sufficient yield for further investigation. Likewise, an attempt to dope with manganese also failed. The process used was to modify the process described in the literature by adding in a small amount of manganese to the carbon crucible and heating to 2200°C , well past the evaporative point of manganese, which also failed to produce high quality nanostructures at an acceptable yield. A few possible nanostructures were found, but they were highly distorted (see Figure 5.17, left). Carbon doping was attempted by adding in methane to the process at a rate of 40 sccm. This seemed to result in nanotubes much like the ones which were present with the original literature process, however, further experimentation was suspended (see Figure 5.17, right). This is because there was carbon contamination

in the TEM, and therefore, determining the presence of any carbon doping would have been extremely difficult. Altering the ratio of boron to nitrogen in a BNNT would also be a method to create doped structures. Creating a BNNT with a non-stoichiometric ratio of boron to nitrogen was attempted by either depriving the reaction of nitrogen or providing excess. The former, which would result in a boron rich structure, was attempted by switching the gas flow to pure argon, after the $B_4N_3O_2H$ formed. This variation resulted in very little observable vapor and subsequent product, which had no interesting nanostructures. An attempt to create a nitrogen rich structure was made by adding ammonia to the reaction. The ammonia was added before the run up to $1700^\circ C$ in the amount of 60 sccm. The addition of ammonia greatly increased the amount of visible white vapor in the reaction chamber and product which was found on the interior walls of the reaction vessel.

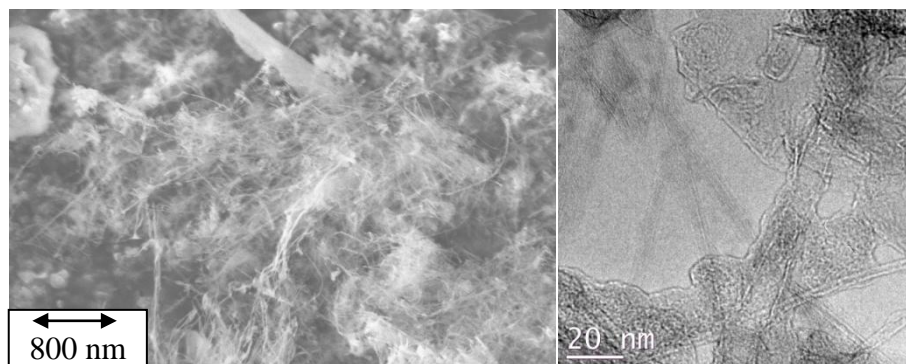


Figure 5.18 (Left) SEM image of result from adding ammonia to the original literature process used to grow BNNTs. These nanotubes did not have excess nitrogen as hoped, but the addition of ammonia did increase the yield and quality of the BNNTs dramatically. The nanotubes are roughly 10 nm in diameter and microns in length. The thin fibrous nature is similar to the material found with no doping, but in the case of the addition of ammonia, the material is much more abundant. (Right) TEM image confirming these structures are nanotubes.

The result from the addition of ammonia was startling (see Figure 5.18). A much greater amount of product was obtained from this variation of the experiment and the proportion of nanotubes increased dramatically. This sample was considered interesting enough for analysis under TEM. The TEM did show the nanotubes were long and thin, however, spectroscopic analysis did not show that the material had a non-stoichiometric ratio of nitrogen to boron. While only a small difference from the normal 1:1 ratio would be enough to cause dramatic changes in the electrical properties, this difference could not be observed with available equipment; only a large difference would be noticeable. Therefore, it was assumed these materials are similar to stoichiometric BNNTs. While the doping of BNNTs has proven difficult, this series of experiments does show that the more available nitrogen is in the system, the more likely nanotubes will result. For example, in the experiment where there is no nitrogen gas at all, only argon, there are no nanotubes. When there is a moderate amount of nitrogen, in the case where no doping was attempted, a small amount of nanotubes was found in the product. Finally, if there is a significant amount of nitrogen available, in the case where ammonia was introduced into the reaction, then a large number of nanotubes result. The final dopant attempted was sulfur, as that has a history of doping boron nitride well.

Numerous papers describe sulfur doped boron nitride [91,92] and there are some models indicating sulfur doped boron nitride nanotubes are stable and have interesting properties [93]. Therefore, sulfur doped BNNTs were considered a very interesting material for investigation ([Sections 5.1](#) and [5.2](#) provided further evidence sulfur could form an important reactant with boron and nitrogen nanostructures). The literature process was altered by allowing the crucible to cool down to room temperature after the

creation of the $B_4N_3O_2H$ intermediate. The intermediate was weighed, found to be 0.36 g in mass, and an equal amount of sulfur was added to the intermediate. This mixture was mortar and pestled and placed back in the carbon crucible of the CVD chamber. Since ammonia seemed to increase the yield of nanostructures, ammonia was flowed in at 60 sccm in addition to the nitrogen. The crucible was then heated to $1700^\circ C$ rapidly and held for 2 hours. This is well past sulfur's evaporation point of $444.6^\circ C$ at atmospheric pressure. The reaction chamber, after heating, was filled with evaporated sulfur and presumably some of the white vapor present in the other reactions. The material on the side walls of the reactor was collected and examined under SEM. (Note, unfortunately flow rates in the experiment were difficult to control. While this never actually changed the final product, the final yield was found to vary from experiment to experiment when attempting repeatability. This was especially the case for the sulfur doping experiments.)

The SEM revealed that the product of the sulfur doping resulted in a wide variety of nanostructures, but primarily nanorods were found (see Figure 5.19). These nanorods were roughly 100-500 nm in diameter and several microns long. Nanowires were also found in the material, however, they were extremely rare in the sample. A nanoribbon like material that had a highly ordered morphology was also discovered, but it was also extremely hard to find in the sample. Overall, the SEM was extremely promising, so TEM analysis was performed.

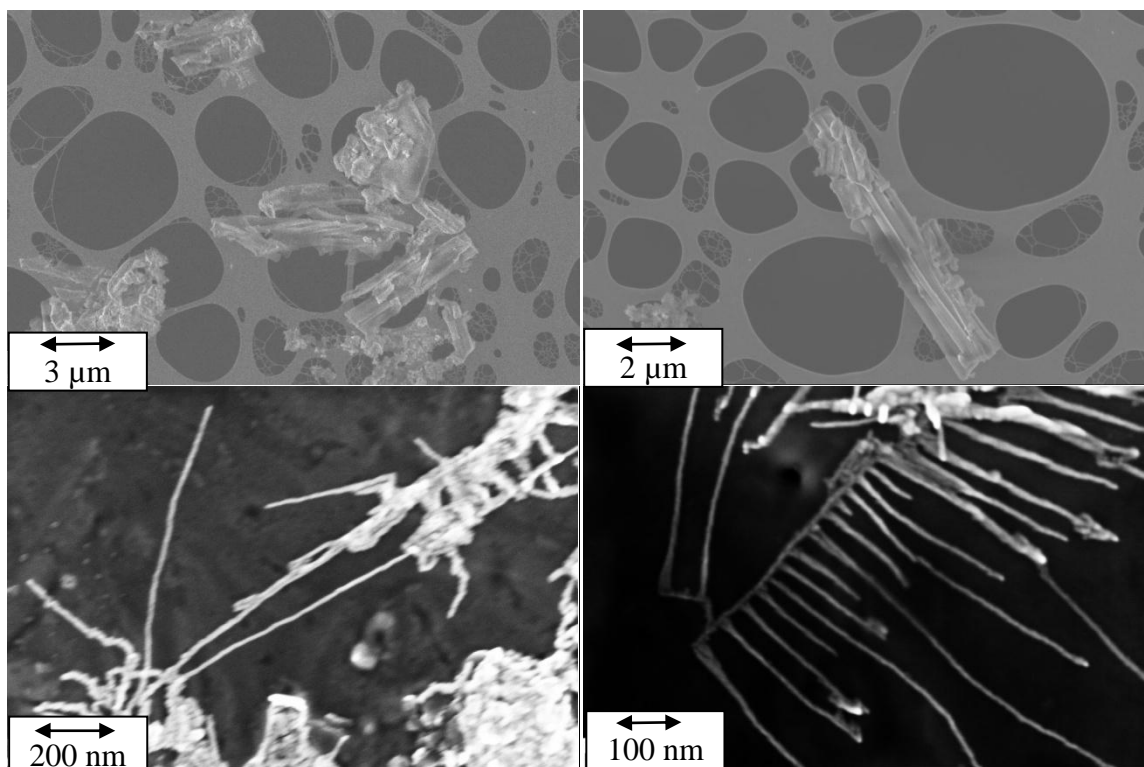


Figure 5.19 (Top left and right) Nanorods found in the sulfur doping experiment. The rods appear to be 100 nm to 500 nm in diameter and several microns in length. (Bottom left) Nanowires found in the product of the sulfur doping experiment. The nanowires are roughly 20 nm in diameter and have large aspect ratios. These were difficult to find in the sample. (Bottom right) Interesting branching nanoribbon, an extremely rare find in the sample. It is most likely two-dimensional in shape, though it could be a branched nanowire. Each ‘branch’ seems to be 10 nm wide with a distance of 50-100 nm between each branch. The branches have a large aspect ratio.

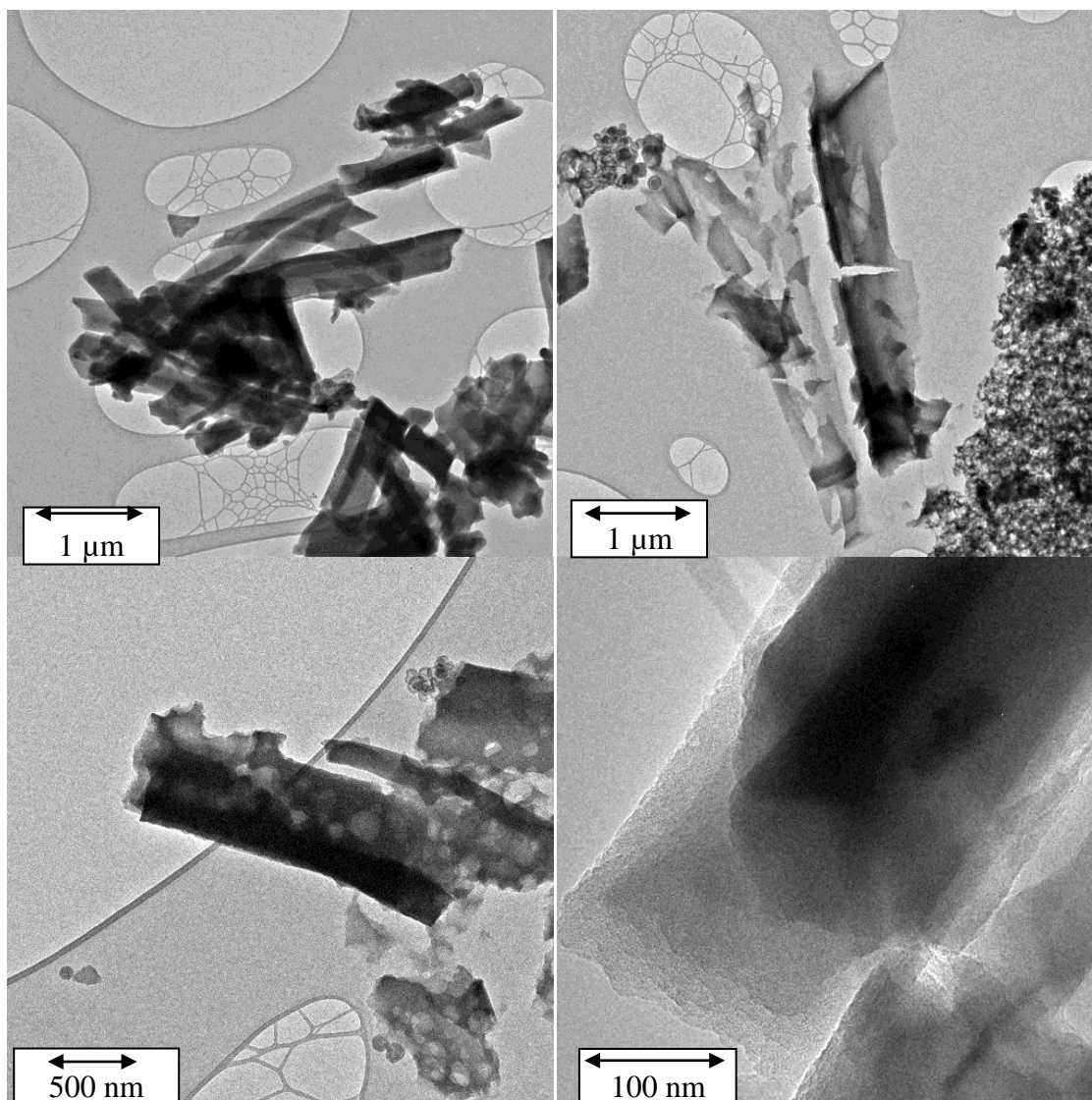


Figure 5.20 (Top left) Nanorods scattered about the TEM grid, confirming results from SEM analysis. (Top right) Nanoplatelets that were found throughout the entire sample. (Bottom left) Nanoplatelets flaked from a nanorod. (Bottom right) High magnification image of flakes stacked on top of each other.

The TEM confirmed some of the results of the SEM analysis (see Figures 5.20 and 5.21). The material was primarily nanorods. The smaller nanowires and nanoribbons discovered using the SEM could not be found on the TEM despite an exhaustive search. However, clearly there was a large presence of nanoplatelets which were not discernible using the SEM alone. The nanoplatelets were produced,

intriguingly, through a flaking method; the nanorods would spontaneously break off flakes after a period of time. (Presumably, the nanoribbon was also made this way, but for whatever reason, the flaking produced a regular structure.) While graphene and its boron nitride analog can be manufactured through intense ultrasonification of graphite and hexagonal boron nitride, respectively, this is the first reported method of spontaneous flaking from nanorods as a means of creating nanoplatelets. The only agitation, if it is even required to produce the platelets, is that which occurs when dropping the sample on the TEM stub.

The nanorods and nanoplatelets are both seemingly amorphous, as confirmed through fast fourier transform analysis as well as small area electron diffraction. Due to carbon contamination of the TEM, an accurate measurement of the thickness of the platelets could not be determined, but they appear to be very thin and have areas measured in the microns. The yield for the nanorods and nanoplatelets is quite high; the entire sample basically consists of those structures. The nanoribbon which was found in the SEM but not the TEM can be presumed to be related in structure to the nanoplatelets, but the formation of that morphology seems to be extremely rare, though since it was found it is certainly a stable structure. EDX analysis revealed the material is primarily boron-carbon with possible sulfur, magnesium, and silicon impurities. EELS only detected boron, carbon and sulfur. Due to carbon contamination, the exact ratio of boron to carbon could not be determined.

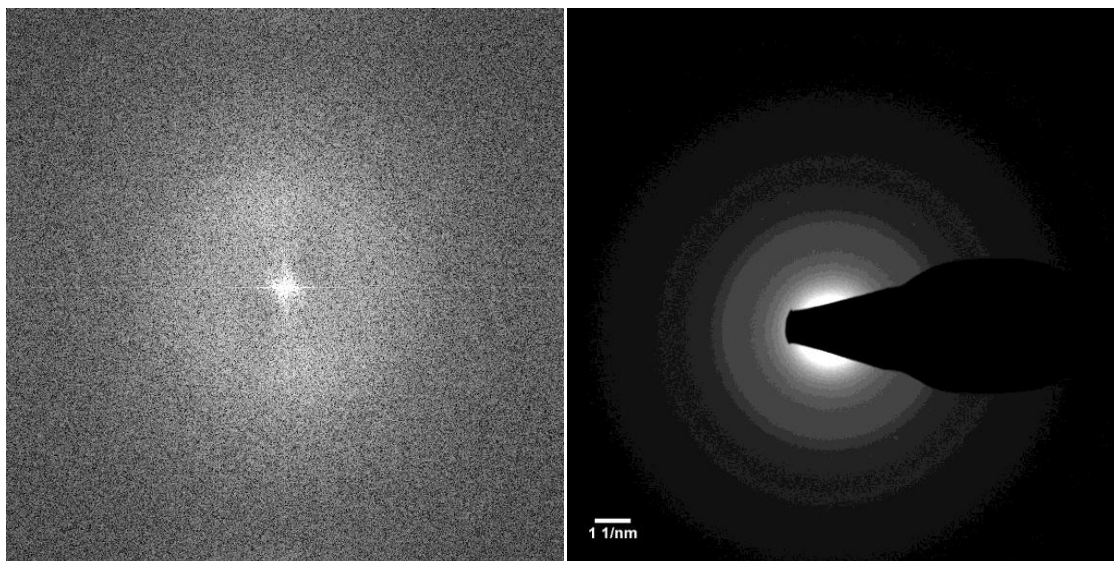


Figure 5.21 (Left) Fast Fourier transform of flakes indicating amorphous structure. (Right) Small area electron diffraction of flakes confirming amorphous structure.

Raman analysis was performed on the sample as well. The Raman spectrum from the sulfur doping experiment surprisingly indicated there was no peak at or even near 1369cm^{-1} , which is the peak expected for multiwalled boron nitride nanotubes and hexagonal boron nitride. Only a very small bump was noticed between 1124 and 1138cm^{-1} . This signal, while weak, is repeatable and was confirmed with outside assistance using a Raman spectroscope with 785nm laser. The Raman spectrum indicates the material is not particularly Raman active and seems to fluoresce strongly. This might indicate the material is acting in a metallic fashion. The normal B-N bonds which cause the peak at 1369cm^{-1} are obviously not present. The Raman spectrum of both normal BNNTs and the product from the sulfur doping experiments is given in Figure 5.22. Figure 5.23 gives a close up view of the only Raman activity found for the sulfur doping experiment.

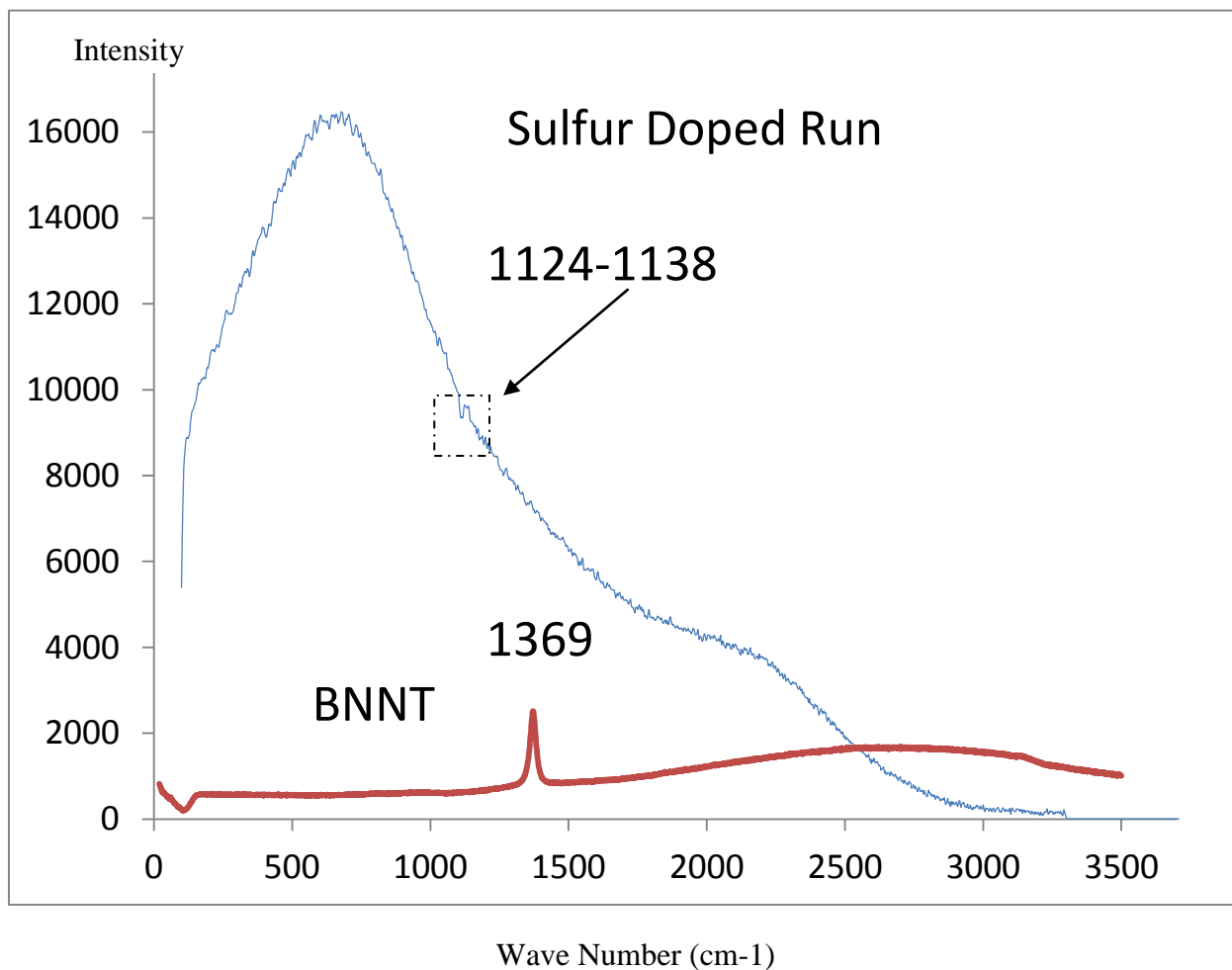


Figure 5.22 Raman signal of the experimental run with sulfur vs. boron nitride nanotubes. Note that the 1369 cm⁻¹ is completely eliminated and there is a very small amount of Raman activity near 1124-1138 cm⁻¹. This small peak is repeatable and was confirmed through independent analysis using another Raman instrument. For convenience and better analysis, the small area in the dashed box was plotted separately in Figure 5.23.

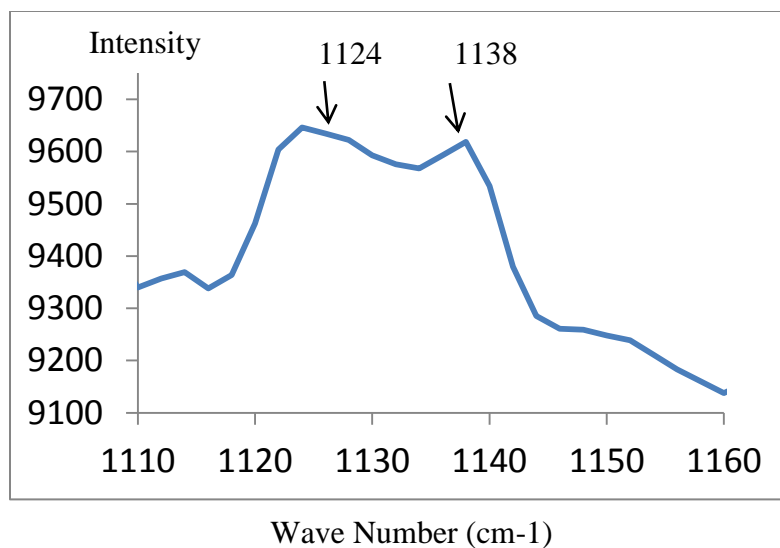


Figure 5.23 Much closer look at the Raman spectrum identified in the product of the S doped experimental run, clearly showing a very small doublet peak.

In closing, the attempts to create a doped BNNT structure were basically unsuccessful in the most direct terms. (Table 5.1 summarizes the results of these experiments.) No confirmation was made of a boron nitride nanotube which was doped well. The doping of BNNTs is most likely extremely difficult due to the high stability of the B-N bonds and the sensitivity of the nanostructure to the breaking of these bonds. Ironically, one of the positive aspects of BNNTs is that they have low defect rates, but the resistance to defects may also lead to the difficulty of doping. (Doping is just a defect that happens to be desired for the application). The manganese doping may have created some sort of doped, yet heavily damaged structure, but this was considered ultimately uninteresting. Carbon doping may have been effective, but that would have been difficult to confirm with the experimental tools available. In fact, only fluorine and carbon have been shown to be effective dopants of BNNTs up until this point in literature, see references [86,87]. The research conducted has been productive, however. The importance of free nitrogen to the yield of BNNTs in these types of experiments has been

proven, as the experiments with the addition of ammonia have shown. This could be considered an improvement to the process already known in literature. Even more excitingly, the addition of sulfur seemed to have a dramatic affect on the reaction, yielding unexpected results. A wide variety of nanostructures were synthesized such as: nanorods, nanoribbons, nanowires, and nanoplatelets. These seem to be very novel materials with a variety of chemical bonds locked in the amorphous phase. This is evident in the TEM analysis. The material is not Raman active, and clearly is very different than traditional BNNTs and h-boron nitride, further indicating it is a novel material. Depending on the electrical properties of the material, it could find some use in electronic applications. (The Raman signal might hint the material is conducting, because it seems to have a Raman signal like a metal except for the identified small peak.) Unfortunately, the nanowires and ribbons were not found despite a thorough search using the TEM, but they do possess an interesting morphology which needs further examination. The nanoplatelets and rods, on the other hand, were ubiquitous in the sample, found easily, and examined thoroughly. The conclusion chapter of this dissertation discusses possible uses of these materials.

Table 5.1 Summary of the Experiments Attempted in this Section. Only when Sulfur is Added to the Reaction is There a Truly Exciting Product

Dopant attempted	How literature process was modified	Result
Boron	Replaced N ₂ with argon to create N deficient environment	No nanostructures
Nitrogen	Added ammonia at a flow rate of 60 sccm	High yield of BNNTs
Carbon	Added methane in the amount of 40 sccm	Unknown if doping occurred
Chlorine	Added low flow 10 sccm of BCl ₃	No nanostructures
Manganese	Tried to evaporate added manganese in reaction chamber by increasing reaction temperature to 2100° C	Damaged nanostructures
Sulfur	Added sulfur to the reaction intermediate before heating to 1700° C	Amorphous boron nitride flakes

CHAPTER 6

ONE-STEP CVD SYNTHESIS OF A BORON NITRIDE NANOTUBE-IRON COMPOSITE

6.1 Introduction to Nanotube Composites

Boron nitride nanotube (BNNT) and carbon nanotube (CNT) composites are an exciting class of novel materials because of their very attractive mechanical properties. Pure BNNTs also have superior thermal, chemical, and toxicity characteristics compared to their carbon analogs in addition to having experimentally-determined mechanical strengths rivaling those of CNTs (see [Section 1.5](#)).

Composites containing CNTs are well known, but work still continues to fabricate and tailor improved composites of CNTs with polymers and metals [94, 95]. Pure and functionalized CNTs also continue to elicit enormous attention due to their remarkable electronic, optical and mechanical properties [96-100]. Because of their remarkably high mechanical strengths at the nanoscale level [101-104], a tremendous amount of work has been dedicated to investigating structural applications of CNT composites. Metal-CNT composites are extremely exciting because they can replace pure metals in a variety of applications. The most interesting of these metal-CNT composites resulted from mixing catalyst precursors with a metal matrix, and subsequently growing carbon nanotubes directly into the matrix [105,106]. This process is highly efficient, as it eliminates a number of steps associated with rival processes, ensuring an even distribution of nanotubes throughout the composite as well as providing strong bonding between the nanotubes and the metal with little damage to the nanotubes or the composite. Nanotube infiltration by this method was shown to increase mechanical strength by 45% relative to control samples of the neat metals at relatively small loadings. This substantial increase

is due entirely to the high strength of the carbon nanotubes. BNNTs also possess similar strength and some properties that are superior compared to CNTs, and have therefore garnered growing interest in recent years [107]. They are chemical cousins of carbon nanotubes, forming a rolled graphite-like structure composed of alternating nitrogen and boron atoms which gives them properties as remarkable as those of CNTs. For example, they possess mechanical strength similar to CNTs and electronic properties which, unlike CNTs, are independent of tube chirality, thus making them more desirable for electronic applications requiring insulating and semiconducting properties [108-111]. There are many other important advantages of BNNTs in comparison to their carbon analogs. CNTs burn in oxygen at a relatively low temperature, as opposed to BNNTs, which are stable in air up to 1000° C [111]. If isotopically-enriched boron is used, BNNTs will form a useful shield against radiation. BNNTs could also perform better under compressive loading than carbon nanotubes. BNNTs are less toxic than CNTs, which have been shown in a number of studies to be cytotoxic [112, 113]. Composites made from BNNTs could thus be used more safely for biological applications than CNTs. A process to fabricate BNNT-metal composites is therefore highly desirable because of these unique properties of the BNNTs.

One of the best approaches to metal-nanotube composites is that used by Goyal et al. [105, 106], which creates a strong composite by evenly distributing CNTs throughout the bulk of the metal matrix and using them to firmly anchor the metal particles in the composite. This prevents the movement of the metal particles, strengthening the composite material. Here, a related chemical vapor deposition (CVD) process is described that can be used to grow BNNTs into a metal matrix to form a high strength

metal-nanotube composite. The process involves the use of iron boride which has been previously demonstrated to catalyze the synthesis of BNNTs [114]. Iron is a well known catalyst for ammonia decomposition and it facilitates the growth of BNNTs at a lower temperature. Nitrogen from the decomposition of ammonia reacts to form the BNNTs, which grow out from the iron particle. The iron particles, therefore, provide an ideal matrix for the formation of the iron-nanotube composite. As nanotubes grow from different iron particles, they can eventually grow into a neighboring iron particle to form bridges across metal particles to increase the mechanical strength of the composite material.

As discussed later, the iron-boride catalyst is pressed into a pellet and then exposed to ammonia to form a composite structure comprising of micron-sized iron fused together by BNNTs. An ideally nanostructured BNNT-Fe composite, the first of its kind to the best of our knowledge, is thus formed. BNNTs have been used to improve the mechanical properties of materials such as glass, providing an increase in strength of 90% and an increase in fracture toughness up to 35%, using only a 4 weight % loading of BNNTs [115]. BNNTs, however, have never been mixed with a metal to form a composite before this work was conducted, and also have never been directly grown into a matrix to deliberately improve the mechanical properties of the composite formed.

6.2 Synthesis of BNNT-Fe Composites

The iron boride catalyst was made using a solution process which is described in references [113, 116-118] and [Section 1.4](#). Briefly, 0.1 mol dm⁻³ aq. FeSO₄ (500 ml) was added dropwise to 1 mol dm⁻³ aq. KBH₄ (500 ml) over 30 min with strong agitation at room temperature. The powder product of Fe–B was dried in argon after being washed in turn with distilled water, ethanol and acetone. A slow rate of addition is critical to prevent excessive oxidation. The reaction is relatively straightforward and scalable. Since the process is performed in an aqueous medium, significant oxidation of the catalyst occurs. According to UV-Vis spectroscopy and energy dispersive x-ray (EDX) analyses, the iron boride catalyst is roughly 59-65% iron, 4-5% boron, and the rest is oxygen with a slight potassium impurity by mass. The large amount of oxide present is reduced by the hydrogen produced by the decomposition of ammonia during the CVD reaction. The control of the iron boride catalyst particle size is critical for optimal growth of the BNNTs. Approximately, 30 minutes of dropwise addition of FeSO₄ solution to KBH₄ solution is needed to produce iron boride of optimal particle size to function as the catalyst.

Different mixtures of pure iron powder and iron-boride catalyst were then created together and pressed into pellets. Roughly, 3 grams of total material was used for each pellet, and the pellets had the following amounts by weight of iron-boride catalyst: 0% (control), 0.1%, 1%, 10%, 50%, and 100%. The mixtures were ground using a mortar and pestle in acetone to form a very fine, easily flowable powder. The pellets were then pressed using a 13 mm KBr pellet die set with loads of 9,000 kg. The density of the pellets in comparison to the density of pure iron (7.87 g/cc) were 72-74% for the 0%, 1%,

and 10% catalyst-loaded pellets. The 50% catalyst-loaded pellet had a density of 60% of pure iron and the 100% catalyst-loaded pellet had a density of 50% of pure iron.

In an attempt to increase the density of the iron boride catalyst pellets, catalyst particles were heat-treated with hydrogen at temperatures of 500°C and 1000°C, and with carbon monoxide at a temperature of 1000°C. Also, the 100% catalyst-loaded pellets were pressed using cold isostatic press (CIP) compression at 207 MPa and 1,380 MPa in an attempt to further increase the density.

An induction heater from Ameritherm Inc was used as the heating source, with a quartz tube reactor as the reaction vessel. The heated container used was a graphite crucible where the various samples were placed. The reactor was flushed with argon (at a flow rate of 160 sccm, standard cubic centimeters per minute) for 30 minutes, and then the pellet was slowly heated to 1100°C over the course of 30 minutes under flowing argon. Afterwards, the argon flow was switched to nitrogen flowing at approximately 160 sccm and ammonia at 8 sccm. The reaction was stopped after 3 hours and the material was allowed to cool for 2 hours in an argon atmosphere. The catalyst loadings of the samples used were as mentioned above. Some samples containing 100% catalyst were gas-treated, and some samples were reacted for 10 minutes with an ammonia flow rate of 32 sccm for faster reaction. Long CVD reaction times were found to deform the pellets, therefore shorter reaction times were preferably used.

6.3 Results and Discussion of BNNT-Fe Composites

The samples with catalyst loading $\geq 50\%$ exhibited a high degree of porosity after pressing. Gas treatment and cold isostatic pressing of the pellet did not seem to alleviate the problem. The pellets which were reacted slowly exhibited inhomogeneities, possibly as a result of damage to the metal matrix and growth of amorphous boron nitride. However, the pellet which had 100% catalyst and was reacted rapidly appeared to be fairly homogeneous and only showed slight deformation, possibly from uneven heating during synthesis. This indicates that a fast reaction would be ideal for a scaled up industrial process. Figure 6.1 shows optical microscopic images of a pellet composed of only the iron boride catalyst before and after the CVD reaction. The most striking feature is the high porosity of the starting green pellet and the reacted pellet indicating that porosity is introduced during pellet preparation and does not change after the CVD reaction.

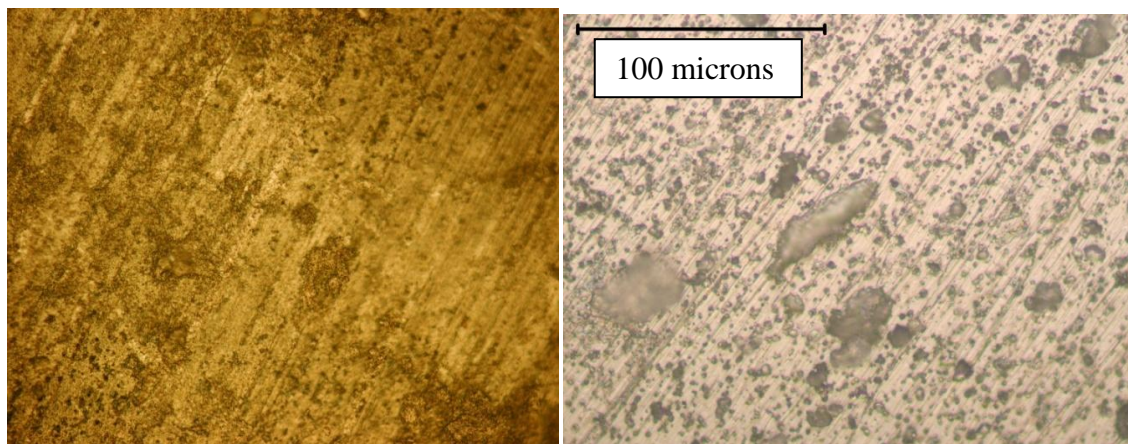


Figure 6.1 Optical images at 500X of: (Left) A pellet before CVD reaction, and (Right) after CVD reaction.

In order to confirm the presence of boron nitride, Raman, FTIR and EDX measurements were performed. Raman spectroscopy revealed a line near 1370 cm^{-1} indicating the presence of boron nitride. The dominant feature of the Raman spectra is a

peak at 1366 cm^{-1} which corresponds to the E_{2g} mode of h-BN in agreement with prior work [119]. FTIR spectroscopy showing lines peaking at 1384 cm^{-1} and 804 cm^{-1} also indicated the presence of boron nitride [120]. As a final confirmation, EDX analyses were performed on the samples prepared. Boron was too light to be detected by EDX; however, nitrogen, iron and traces of a potassium impurity were found.

The X-ray diffraction (XRD) pattern from the composite revealed the presence of iron, Fe_2B (iron boride), and Fe_3N (iron nitride) indicating that the reaction with ammonia transforms Fe_2B into pure Fe while growing the BNNTs. The oxide formed on the catalyst particle is completely reduced since iron oxides are not observed in the XRD pattern from the composite. The XRD line intensities from the BNNTs are most likely too weak in comparison to those from the iron-containing components to be observed.

A Rockwell hardness testing set-up was used to determine the hardness of the samples. Before CVD treatment all of the samples were very soft, almost like a plastic and possessing similar hardness. After the CVD treatment, all of the samples became much harder. In the case of pure iron, one would expect that sintering and nitride formation would be responsible for the increase in hardness. However, for the samples prepared with catalyst, the deposition of BNNTs would also contribute to the increase in hardness. BNNTs are mechanically very strong in the axial direction so that their in-situ formation would lead to enhancement in mechanical properties, such as hardness. Due to high oxygen impurity content and difficulty in pressing the precursor nanopowders, dense pellets were difficult to prepare with higher catalyst loadings. The pellets with low catalyst loading were actually softer than the control pellets. This is most likely because iron mixed with the catalyst covered the catalyst particles when pressed, precluding the

occurrence of a CVD reaction. Moreover, the catalyst lowered the density of the pure material, ultimately resulting in a softer material.

The pellet loaded with 100% catalyst is much harder than the control pellet. Attempts to cut open the pellets loaded with 50% and 100% catalyst were extremely difficult. They each destroyed a diamond saw blade, providing evidence that the inside of the pellets is harder than the measured surface hardness. The pellet with 50% catalyst came out severely deformed, probably due to the mismatch during the reaction between the catalyst and pure iron. This made the material made using 100% catalyst more attractive for further investigation. However, while the pellets made with 100% and 50% catalyst were very hard, each with a HRC level of 48, the pellet which was reacted rapidly was the least deformed. Remarkably, while far harder than the control pellet, the pellet originally composed of the pure catalyst material was far less dense and more porous. The results of the hardness tests are shown in Table 6.1. One should note that according to the American Society of Mechanical Engineers (ASME) standards, porous pellets should not be used for hardness testing, although in the present case it is probably acceptable since the hardness results were found to be highly reproducible (see, American Society for Testing and Materials, ASTM E18-05-e1).

Attempts to improve the density of the material were unsuccessful. Since there was significant oxide on the catalyst, hydrogen and carbon monoxide treatment was thought to be an effective reduction method to eliminate the oxygen. By first reducing the oxide on the catalyst particles, then pressing the pellet, and finally running the CVD reaction one would expect to obtain a higher density pellet. Unfortunately, the gas treatment also eliminated the higher hardness after the CVD reaction. The hydrogen-

treated pellet at 500° C is far softer than the control sample, and gas treatments at 1000° C provided pellets that are even softer. The samples treated at 1000° C were so soft that accurate hardness measurements could only be made in the HRB scale. This is probably because the catalyst before treatment is thermally very sensitive, and thus is easily damaged even by moderate heat treatment. Cold isostatic pressing at both pressures also did not improve the density significantly, so further experimentation was not conducted on the pellets pressed in this manner. Table 6.2 shows results of the hardness measurements on pellets of the gas-treated catalyst particles. Knoop microhardness measurements were performed and converted into HRC values because the Knoop method avoids the larger pores in the material and determines the hardness without the much larger pores, although avoiding the pores altogether is not possible. At the smaller scale, the HRC value was found to be 65.

Table 6.1 Hardness of Pellets with Varying Amounts of Catalyst

% Catalyst	HRC	%Density of Fe@TMD
0	32	75
1	30	72
10	24	74
50	48	62
100	48	50

Table 6.2 Hardness of Gas-Treated Pellets

Treatment Gas and Temp (°C)	Hardness	% Density of Fe @TMD
H ₂ , 500	24 HRC	55
H ₂ 1000	76 HRB	54
CO 1000	60 HRB	53

Measurement of the bulk modulus was performed using the non-intrusive ultrasound method by use of equation 6.1 below:

$$c = \sqrt{\frac{C}{\rho}} \quad (6.1)$$

where C is the bulk modulus and ρ is the density.

Ultrasound sensors and receivers were placed on opposite ends of the flat part of the pellets, creating what is known colloquially as a pitch-catch system. The speed of sound was recorded and equation 6.1 was applied. The pellet with no catalyst was compared with the pellet that was reacted rapidly and had 100% catalyst. Despite superior hardness, the catalyst-treated pellet possessed a much lower modulus of elasticity and specific elasticity than the control pellet. Most likely, this difference comes from the high porosity of the 100% catalyst-loaded pellet. This is very interesting and implies that the material is highly resistant to thermal shock. The results of the ultrasound measurements and calculations of the bulk moduli are shown in Table 6.3.

Table 6.3 Ultrasound Measurements from 0% Catalyst and 100% Catalyst Pellets. The Density is in g/cc, the Velocity is in mm/ μ m, the Bulk Modulus is in GPa, and the Specific Modulus is in kN•m/kg units

Pellet	Velocity	Density	Specific Moduli	Bulk Moduli
Pressed Fe	5.9	7.7126	34.8	268.4756
Cast Fe	4.6	7.3978	21.2	156.5375
0% Catalyst	5.49	5.8238	30.14	175.5299
100% Catalyst	4.66	3.935	21.72	85.4509

The control pellet and the pellet reacted rapidly with 100% catalyst were compared using stress-strain measurements. The specimens were tested in a MTS Servo-Hydraulic Test Device to obtain material properties characteristics, following STANAG

4443. Each sample was loaded in compression at a constant strain rate at ambient temperature conditions. The plots of compressive specific stress-strain curves at strain rates of .025/sec were obtained as shown in Figure 6.2. Table 6.4 shows results derived from this data. The two major differences between the samples are the porosity and the addition of BNNTs, which are in competition with each other. Specific values are used to normalize the effect of porosity to some degree, and in the case of the hardness tests, the higher porosity was more than cancelled out by the addition of BNNTs.

The stress-strain curves corroborated evidence from the hardness and ultrasound measurements indicating that the Fe-BNNT composite exhibited mechanical properties that were distinct from that of the Fe control sample. The yield strength was difficult to determine exactly for the experimental sample because of its complicated behavior, but it was assumed to range from point #2 to point #3 in Figure 6.2. The Fe-BNNT composite possessed a yield strength 18% to 28% lower than the control sample. This is most likely because of the porosity in the Fe-BNNT control sample. Additionally, the elastic modulus of the control sample was 31% higher than that of the experimental sample. This indicates that the Fe-BNNT composite possesses lower stiffness and strength than the pure Fe sample. This behavior was also partly observed in the ultrasound measurements, where the bulk modulus of the control sample was 51% greater than that of the experimental sample. When comparing mechanical properties, one should recall that the experimental sample was also much lighter than the control because of its porosity, which is why a specific stress-strain curve is reported here. This curve shows that the experimental sample has a specific yield strength which is 8.5%-24% greater than that of the control sample.

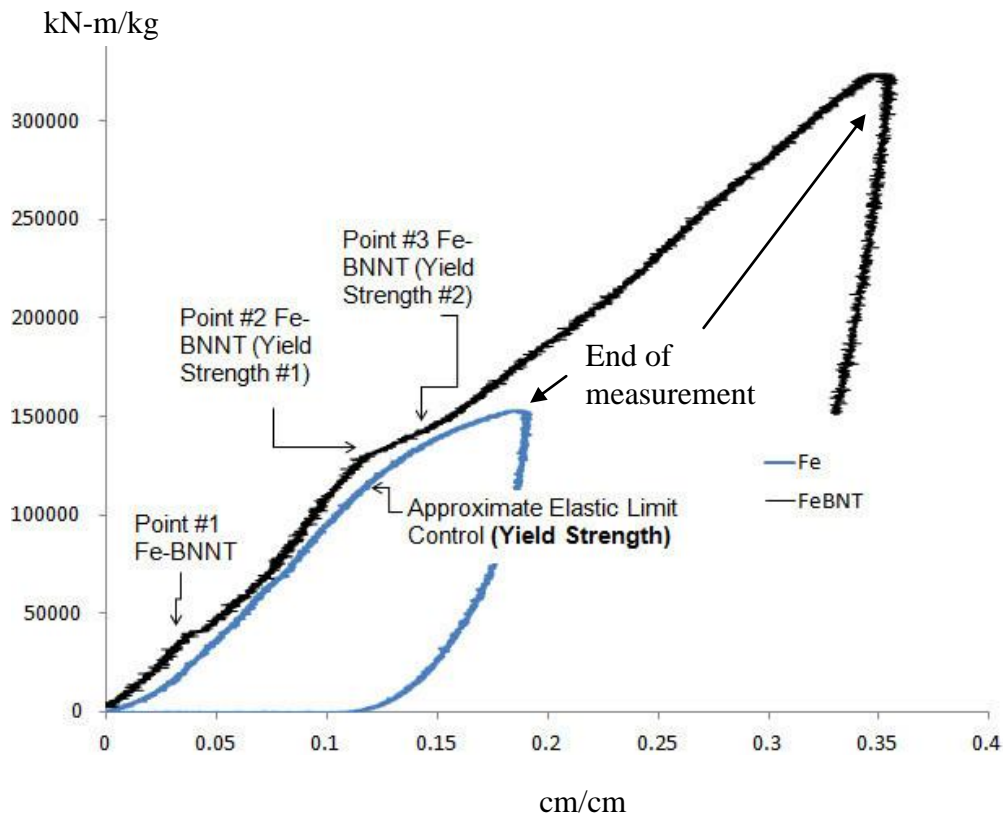


Figure 6.2 Specific stress-strain curves of Fe-BNNT composite (black) and pure Fe (blue). The y-axis units are given in kN-m/kg, which is equivalent to MPa/(g/cc). This is the stress divided by density. This unit takes into account both strength and density. The indicated points are where the yield strengths are assumed to be. The points where the experiments end are also marked. Note that this is not a material property but simply where the experiment ceased.

Table 6.4 Mechanical Properties Obtained from the Stress-Strain Curve

Elastic Modulus, GPa	Yield Strength, MPa		Specific Yield Strength (kN-m/kg)
Fe	690	690	117
Fe-BNNT	459	497-566	127-145
% Difference	-33%	-18%_-28%	+8.5%_+24%

Important Points on Specific Stress Strain Curve for

Fe-BNNT (kN-m/kg)

Point #1	Point #2	Point #3
37	127	145

The control sample showed excellent mechanical properties compared to that of regular pure iron, because it was heavily nitrated and sintered. The experimental sample exhibits rather interesting properties as well. This abnormal behavior has been observed before in a ceramic composite system [121]. From Figure 6.2, one can observe that the Fe-BNNT sample rarely exhibits non-linear stress-strain behavior; however, instead there are regions where the linear behavior changes non-linearly due to the complex properties of the material. The regions where these changes occur are indicated in Table 4. Up until point 1 in Figure 6.2, the experimental data is linear but experiences a sudden non-linearity followed by a return to its original linear behavior. Most likely, large pores dictate the behavior of the material as in reference 28 and a speculative explanation would be required to account for this. Up until point 1, the largest pores are strained heavily, until the pellet is densified suddenly, followed by large pores dictating the behavior of the material until point 2, where the material is densified again. Finally, at point 3, while there are still large pores present, the biggest pores have been eliminated, and the material once again exhibits linear behavior until it fails due to the growth of cracks. Failure of the BNNTs is unlikely because of their expected remarkable strength, therefore, most likely Fe-Fe or BNNT-Fe connections represent the failure points. However, despite porosity and initial flaws essentially dictating the mechanical properties of the composite sample, its specific strength and hardness are far higher than that of the control specimen. This suggests that if a process to eliminate porosity was found, the BNNT-Fe composites would have much higher values of strength than those measured here.

Scanning electron microscope (SEM) images taken from the BNNT-Fe

composites are shown in Figures 6.3-6.5. The SEM image in Figure 6.3 (left) shows BNNTs grown on the surface of a pellet with 100% catalyst. The BNNTs in the image can be seen forming inter-particle bridges in bundles with diameters ranging from 20 to 100 nm. Figure 6.3 (right) is an image of the fractured inside surface of a composite pellet showing the nanoscale adhesion of the BNNTs to the iron particles as a result of the *in situ* process used here to synthesize the composite.

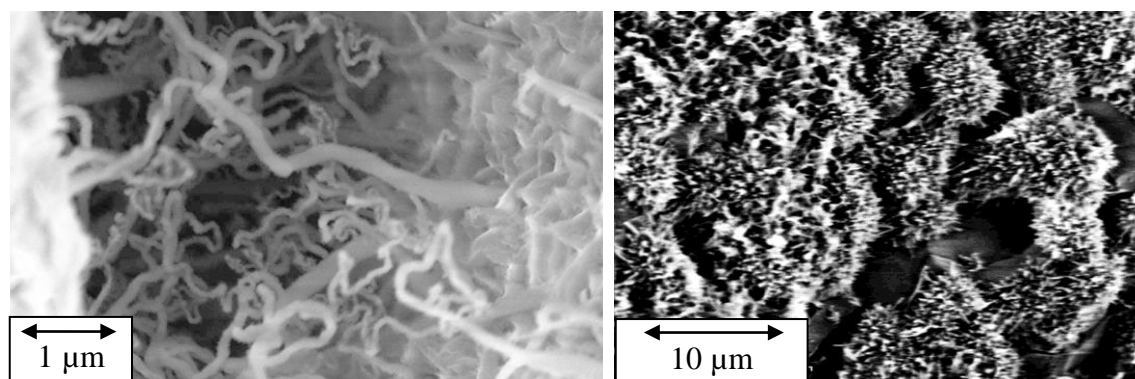


Figure 6.3 SEM images of: (Left) The surface of a BNNT-iron composite pellet, and (Right) interior of a cracked BNNT-iron composite pellet.

An obvious feature of the interior of the pellet is its high porosity. One cause of this is the large change in density when the iron oxide is reduced by hydrogen after the reaction of ammonia with boron. This leaves pores throughout the inside of the material, thus weakening it. If the pores could be eliminated, the composite would become significantly stronger and tougher. The inside of the pellet is covered with BNNTs which are directly connected to iron particles, suggesting that the BNNTs bond well with the Fe particles.

Bridging of BNNTs across the Fe particles is evident from the SEM images in Figures 6.4 and 6.5. In particular, a bundle of nanotubes is seen joining two separate particles while under tension and necking in Figure 6.5. This is an example of structural reinforcement, and provides proof that the BNNTs can neck and undergo great

elongation before breaking, unlike bulk ceramics. One should note that the distribution of BNNTs was more uniform in the interior than on the surface of the pellets.

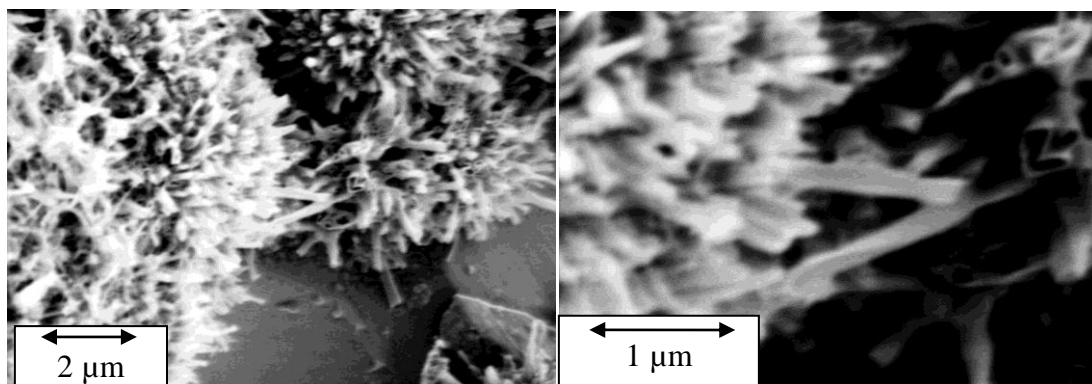


Figure 6.4 SEM images of: (Left) Interior of a cracked BNNT-Fe pellet showing BNNTs bridging from particle to particle, and (Right) a closer view of two particles joined by BNNTs.

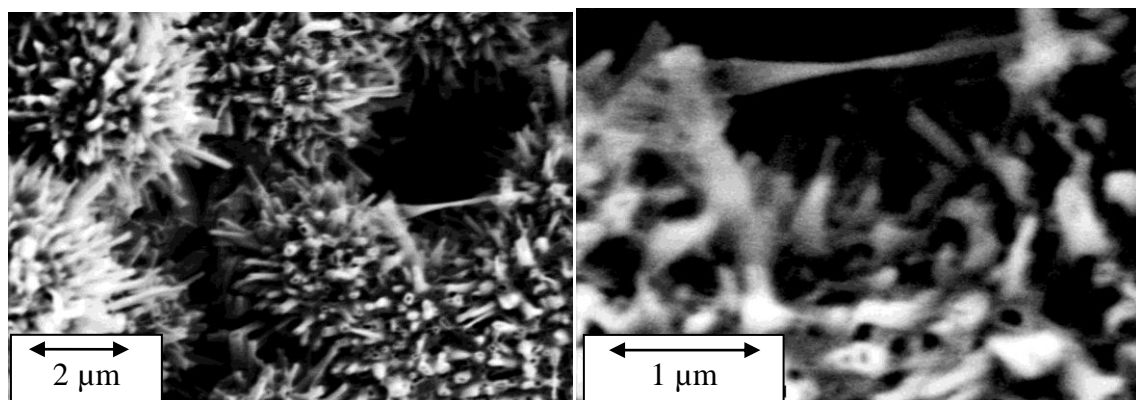


Figure 6.5 SEM images showing: (Left) Overview of BNNT-Fe composite with multitude of BNNTs, and (Right) closer view of two iron particles bridged by a stretched BNNT bundle in the composite.

Transmission electron microscopy (TEM) and selected area electron diffraction were used to provide a more detailed characterization of the BNNT-Fe composites. Figure 6.6 (Left) is a TEM image showing an approximately 5 nm diameter, ten-walled BNNT bridging two iron particles in the BNNT-Fe composite. The nanotube dimensions from the image are in basic agreement with that of previous work [114].

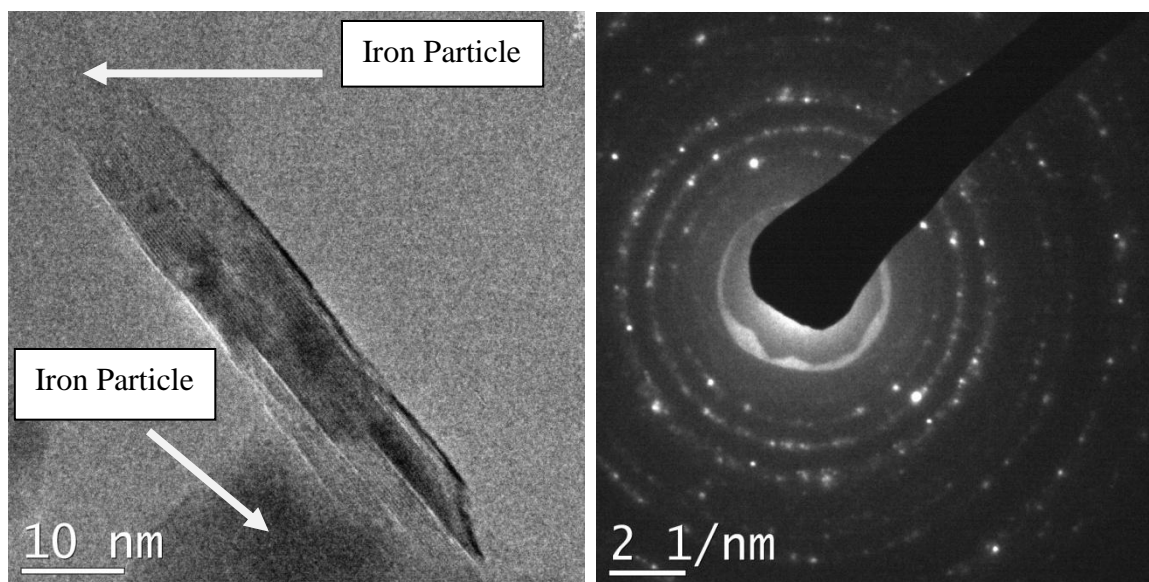


Figure 6.6 (Left)TEM image of a multiwall BNNT with ten walls joining two iron particles in the BNNT-Fe composite; and (b) Selected area electron diffraction taken from the BNNT-Fe composite. The spacings and assignments of the different phases in the composite are given in Table 6.5.

Table 6.5 Spacings Observed from Electron Diffraction Pattern and Phase Assignments

Spacing (nm)	Phase Assignment
0.34	BNNT and Fe BCC
0.29	Fe BCC
0.25	Unknown
0.21	BNNT
0.16	BNNT
0.14	Fe BCC
0.12	BNNT

The electron diffraction pattern, Figure 6.6 (Right) with calculated spacings from the reflections shown in Table 6.5 provides evidence for the presence of BNNTs, Fe BCC, and an unknown phase with one line which did not correspond to any of the expected phases [122, 123]. The unknown spacing of 0.25 nm can be tentatively assigned to a weakly bonded Fe-BNNT phase that might have formed during synthesis.

No evidence for iron boride and iron nitride was found in the selected area of the electron diffraction pattern, although these phases were detected in the XRD patterns which cover a much larger area of the sample.

The *in situ* growth of BNNTs directly into an iron matrix discussed in this paper provides a BNNT-metal nanocomposite with a number of benefits. If the nanotubes were grown first and added to the metal powder, they would have to be grown separately from the catalyst, mixed intimately with an iron matrix (an extremely difficult process) and then pressed without damaging the nanotubes – a process that would also be difficult. The process described here removes a number of steps by directly growing the nanotubes in one-step in the pellet. Since boron nitride nanotubes can be grown using an iron boride catalyst, the iron from the catalyst forms the matrix, thereby providing a novel and facile route to a metal-BNNT composite with high yield strength.

The electron microscope images indicate that the composite formed is an ideally nanostructured material, with nanoscale basic constituents that are distributed in an interconnected network. Its mechanical properties can be improved by further compression using an isostatic press. Additionally, the BNNTs provide a thermally and chemically stable barrier protecting the iron matrix, making the material extremely strong and resistant to chemical and thermal attack in harsh environments. Moreover, since BNNTs are biologically non-cytotoxic to some cell types, the Fe-BNNT composite would be ideal for use in certain medical applications.

CHAPTER 7

CONCLUSIONS

7.1 Review of Critical Results

The IL method has been able to synthesize a remarkable variety of nanostructures, some novel, some well known. Simply by altering which dopant gases are used, very different materials can be created. Several alternative methods of nanosynthesis were discussed, but they are highly related to the IL method. The novel nanostructures created through the IL method have not been characterized, but if they possess properties which are desirable in composites, the method discussed in [Chapter 6](#) should be amenable, especially because the catalyst is the same type of metal boride precursor used in the IL method. The method discussed in [Section 5.3](#) is also different from the IL method but creates sulfur doped boron nitride nanostructures, which are elementally and morphologically similar to the materials made through the IL method, especially the boron flakes and sheets. The greatest strength of the IL method and its related techniques is that a wide variety of materials can be synthesized using a similar process, which raises the exciting possibility of synthesizing devices. By varying growth mechanisms, not only could discontinuous nanostructures be created in a linear fashion, a method to create branching structures such as y junctions could also be realized, see [Section 1.7](#). Before discussing the implications of this, a quick review of the utilized catalyst precursors and some of the novel growth mechanisms which were discovered in this dissertation is required.

7.2 Purpose of the Various Catalyst Precursors in the Reaction

One obvious distinction of the IL method is that two of its catalyst precursors, MCM-41 and nano-NiB, are exciting nanomaterials in of themselves. The strength of the method may come from its use of these two nanocatalyst precursors, which presumably contributes greatly to the reactivity of the method. The $\text{MgB}_2/\text{Mg}(\text{BH}_4)_2$ and the NiB play obvious roles in the IL reaction, as they are catalysts and sources of boron. Since the MgB_2 and $\text{Mg}(\text{BH}_4)_2$ result in different materials in every case, this shows that the magnesium-boron source plays a critical role in the reaction. There is a possibility the hydrogen is playing some role in the reactions, though hydrogen is introduced in the IL method with all of the dopant gases. Perhaps having it initially attached to the borohydride results in a different product or the sheer quantity of hydrogen causes a difference in the reaction conditions. (The former is most likely the case, as the latter seems unlikely considering the large difference in structures obtained when using different magnesium-boron sources). The two precursors are also used at different temperatures, which could also help to explain the differences between IL reactions which use the two.

Originally, large particle sized NiB was used but nano-NiB seems to result in a higher quality and yield product. FeB seemed to work effectively as well, but NiB always resulted in a higher yield. (These variations were done with the original IL method only with no dopant gases.). The MCM-41 presents a more interesting case than the other reaction precursors. The MCM-41 was assumed to act as a template in the original, undoped reaction, which would allow the growth of boron nanotubes. However, recent evidence indicates the IL method, with no MCM-41, no dopant gases, and MgB_2

shows the growth of boron nanotubes mixed with boron nanowires. When using the same reaction conditions except with MCM-41, only boron nanowires were found.

In another fascinating twist, when performing the IL method with hydrogen sulfide, methane, and MgB_2 , boron-carbon-sulfur sheets result. Surprisingly, when the MCM-41 is removed, carbon nanotubes result. The MCM-41 therefore must participate in the reaction as more than a template. In fact, it doesn't function as a template at all because sheets grow in its presence using certain doping gases, not nanofibrous materials. Also, frequently in the IL reactions, materials larger than the pore size of the MCM-41 result, which also provides evidence it is not acting as a template.

7.3 Novel Growth Mechanisms and other Insights

Every material synthesized from the IL method was presumed to grow through a simple VLS method. This would explain the presence of the catalyst in the nanowire/nanotube tips, and the speed of the reaction. The growth of the boron sulfur sheets presents an interesting deviation, though it can be explained through an onion/flower method discussed in [Appendix A](#), where the growth of graphene on nano-iron particles is investigated. The appendix chapter on graphene itself also brings up other surprises, as a process fully expected to grow MWCNTs actually resulted in the growth of graphene/graphitic nanoplatelets. Understanding why this occurs could reveal deep insights into the seemingly intractable issue of the interaction of carbon gases, carbon nanomaterials, and catalyst.

The other novel growth mechanism which was uncovered was with the sulfur doped boron nitride structures. Here, flakes seemed to result from the growth of nanorods

which subsequently shed nanoflakes after a period of time. When the flaking actually occurs is debatable, although the flakes can mostly be found next to the nanorods from which they originated, which should be a useful hint.

The IL method may have some affinity to create materials with a hexagonal crystal structure, as BNNTs, MgB_2 , and CNTs all have a hexagonal type structure. Why this is true is unknown. It could simply be a matter of coincidence, as the IL method has a predilection to create nanomaterials, and hexagonal materials have a tendency of forming nanomaterials. While the IL method does show it can create several novel nanostructures, the most exciting possibility lies in its ability to make heterostructures.

7.4 Review of Nanoflakes and Nanofiber Heterostructures

The IL method has successfully demonstrated the ability to grow boron nanoflakes and folded sheets composed of boron, carbon, and sulfur. A related method was used to grow amorphous boron, nitride, and sulfur sheets. An obvious question would be if the boron-carbon-sulfur sheets of [Section 5.2](#) are ‘related’ to the boron-nitride-sulfur sheets of [Section 5.3](#). While the growth mechanism of both is different, they have the following in common: they both are amorphous, have somewhat similar elemental composition, their thicknesses are similar, and they both have similar Raman signatures. Even more excitingly, since they’re both already amorphous, they should have no problem joining with the following: boron nanosheets, boron nitride nanosheets, each other, graphene, or other similarly two-dimensional nanostructures. The IL and related methods have successfully introduced three of these structures, and other techniques can create the other materials (since the IL method can grow CNTs, growth of graphene should also be

possible through some modification). The number of hybrid nanomaterials which could be synthesized is staggering. A possible device is given in Figure 7.1. This, in theory, could be 1 atom thick device. (Ultimately, thickness depends on how thin the materials made through the IL process can be made.) In comparison to traditional electronic devices, due to its extremely small size, the one shown in Figure 7.1 would be much faster, more energy efficient, and could possibly exploit novel quantum effects.

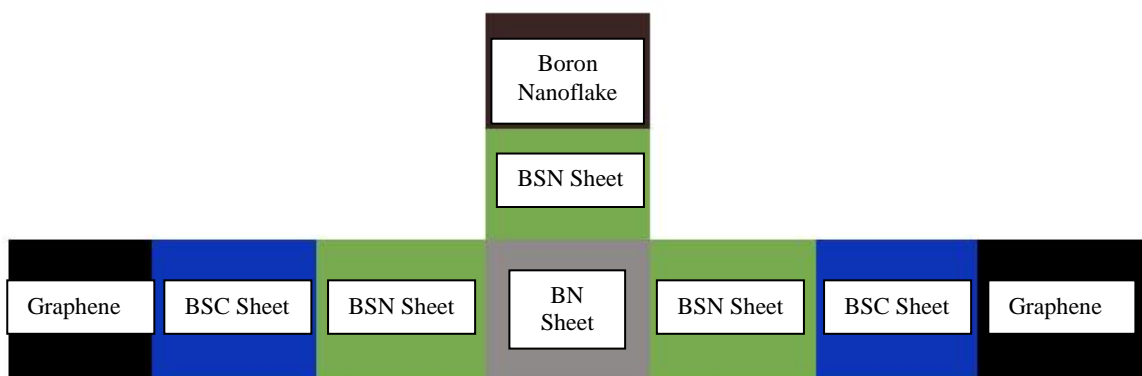


Figure 7.1 An example of an atomically thin, complicated device possible through the IL method.

The IL method not only introduced a method to create a number of nanoflakes, a great variety of nanowires/nanotubes/nanorods can be synthesized using the process and they too could be joined together to form novel devices. Especially of interest would be joining axial nanostructures with radial nanostructures. The flake materials could easily be joined with the nanofibrous materials as shown in the Figure 7.2. Wires and flakes don't necessarily have to be joined together in such a linear fashion, as graphene could be joined to a carbon covered boron nanowire (the type discussed in [Chapter 3](#)), or a boron nitride nanoflake could be joined to a MgO covered in BNNT. A facile arrangement is given in Figure 7.3, where graphene is used to join a carbon covered BNT nanowire. The nanowire itself could be part of a larger scale heterostructure.



Figure 7.2 Nanowire of sections of material which could be created through the IL method. Graphene could easily be joined with CNTs.

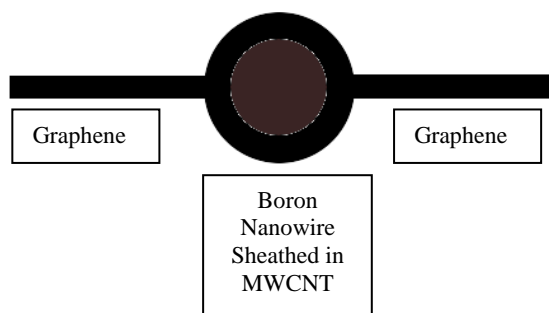


Figure 7.3 Graphene joined to a boron nanowire covered in a CNT. This structure could have interesting electrical properties as well. Morphologically, a boron nitride sheet could form around a boron nitride covered MgO nanowire in the same manner.

7.5 Review of Composites

[Chapter 6](#) successfully demonstrated an easily scaled up method of creating composites with nanomaterials. If a material synthesized through the IL method is desired in a nanocomposite, it can be synthesized readily. The variation of the IL method used depends on which nanomaterials are desired. The scaled up method has only been demonstrated using CNTs and BNNTs. The CNT method used a catalyst very different than the one used for the IL method. The BNNTs used a FeB catalyst made in the same way the NiB precursor was synthesized, suggesting that methods to scale up the IL method should be feasible. (Trying to create a manganese boride catalyst actually

resulted in an unexpected nanostructure, see [Appendix B](#).) The composites demonstrated far greater strengths than composite materials made through comparable techniques, indicating the in situ growth techniques used are a superior method of creating these types of composites. The graphene composites did not possess greater strength than their corresponding control samples, which may show that NTs may be superior for enhancement of metals. Speculatively, this could be due to nanoflakes not effectively bridging the sample as nanotubes do. The main obstacle for commercialization of the composites is they lack sufficient density. The density of the composites must be increased before they can be considered useful. As of now, while fairly strong, especially for their low weight, the high porosity of the currently synthesized composites precludes most possible applications. These techniques are not limited to applications where great mechanical properties are required, but in any situation where nanostructures are needed in a bulk composite. The advantages of the demonstrated techniques are: low cost, even dispersion through the matrix material, strong bonding between the nanomaterial and the matrix, and trivial scalability.

7.6 Challenges to Overcome in the IL Method and Future Experiments

While this chapter raises a number of exciting possibilities, there remain a large number of difficult obstacles to overcome. Only a very irregular, large hybrid nanostructure was demonstrated using intermittent doping. This suggests that simply varying reaction conditions from one to another may not actually make hybrid structures in a reliable fashion. Therefore, intermediate steps might be needed. Also, branching was never demonstrated, though in principal, it should be possible by altering the growth

mechanism. None of the basic parameters such as reaction temperature/pressure, flow rate, etc. were varied, therefore, their effect on the IL method and its variations are currently unknown.

The most obvious next step is to analyze the electrical properties of the materials created, and decide which one(s) are of greatest interest. Then, apply a DOE to the synthesis process which created them. This would allow one to quickly determine the critical parameters and the affect they have on the final product. The IL method creates a large number of possible structures, and determining which ones are of greatest interest is impossible without characterization.

To explore the entire IL method would be prohibitively expensive and time consuming, therefore, only the most exciting variation must be examined. Once the electrical properties of the materials are determined, useful heterostructures can be considered and created. Studying the interface between the discontinuous materials must be done when they are synthesized. First, interesting structures must be identified and created, however, once this is done, the interface should be analyzed as understanding how these materials join together would be scientifically exciting. Also, for practical applications, these joints could cause some problems for utilization of these heterostructures, or could even be exploited for novel device characteristics.

As previously stated, the most obvious experiment is to identify which novel materials were synthesized that have exciting properties. Then, perform a DOE identifying which process parameters are most critical for the synthesis of that material. Specifically, yield and quality should be targeted. Also, if hybrid heterostructures are considered of interest, attempts to synthesize them should be carried out. Realistically,

before the branching devices previously discussed can be synthesized, a sophisticated understanding of how to create branching structures and hybrid materials is needed, but the IL experiment does provide a proof of concept that something along these lines is possible. Only further experimentation into trying to create hybrid structures will reveal if it is feasible. Addition of plasma should also be attempted, as plasma chemical vapor deposition processes are known to have a number of advantages over traditional chemical vapor deposition. Attempting the reaction at different pressures could also allow the synthesis of novel materials or the known materials at greater yields. Ultimately, if this method does seem to hold promise in creating nanostructures of interest, lithography techniques could be used to create the novel structures. This would allow controlled synthesis of the desired materials/nanoheterostructures, which should be facile as the type of catalyst is basically the same for all of these materials.

Recall the nanoflakes of [Section 5.3](#) were made in a different manner than most of the other materials discussed. If the nanoflakes are desired to be joined with other materials possible through the IL method, it may be of use to determine a method of synthesizing them using the IL method. If the IL method eventually moves to lithography techniques, the flakes might be synthesized through heavy ion implantation of boron nitride. A large mix of products were synthesized with the flake material, better control of the growth mechanism could allow one to exclusively obtain one of the following as opposed to a mixture: nanoribbons, nanoflakes, nanorods, or nanowires.

Table 7.1 Summary of the Results of this Dissertation

Added Gas	Catalyst/Boron Source	Material Result
None	No Silicon, MgB ₂	Boron nanoflakes, nanowires and nanotubes
None	MgB ₂	Boron wires
None	Mg(BH ₄) ₂	Boron nanotubes and nanowires
Intermittent NH ₃	MgB ₂	MgO covered in BN Walls
Intermittent NH ₃	Mg(BH ₄) ₂	Boron-boron nitride heterojunctions, boron nitride nanowires, and boron nanowires
NH ₃ + H ₂ S	MgB ₂	Doped boron nanowire
NH ₃ + H ₂ S	Mg(BH ₄) ₂	MgB ₂ nanowires
CH ₄	MgB ₂	CNT covered boron nanowires
CH ₄	Mg(BH ₄) ₂	CNTs mixed withb nanowires
CH ₄ + H ₂ S	MgB ₂	Thin, amorphous sheets with folds composed of boron, carbon, and sulfur
CH ₄ + H ₂ S	Mg(BH ₄) ₂	CNTs
CH ₄ + H ₂ S	No Silicon, MgB ₂	CNTs
[Other Reaction]		Thin amorphous sheets of B-N and sulfur
[Other Reaction]		Nano-iron BNNT composite
[Other Reaction]		Graphene grown on nano-iron
[Other Reaction]		Amorphous and crystalline MnO _x nanowires

Modeling may prove a useful tool in the future, as it would help to characterize the materials described in this dissertation. Modeling could be performed on possible heterostructures before they are synthesized, ensuring they would have useful device characteristic. Computer simulations could also be performed on the growth conditions of the IL method. This would help to elucidate how the reaction parameters affect the final product. Modeling would cause a tremendous reduction in the number of experiments

necessary to fully understand the IL method and could help give a direction for future research. As of now, the IL method, related techniques, and processes to create composites *in situ* all seem to possess nearly unlimited potential. However, before the results of this dissertation (summarized for convenience in Table 7.1) can be exploited, a great number of intelligently performed experiments will be needed to know which materials are desired and the optimal techniques to create them.

REFERENCES

1. J. Liu and Z. Iqbal: Facile Synthesis of Pure Boron Nanotubes and Nanofibers. *Materials Research Society Symposium Proceedings*. **1307**, cc05 21-26 (2011).
2. J.J. Fu, Y.N. Lu, H. Xu, K. F. Huo, X. Z. Wang, L. Li, Z. Hu, and Y. Chen: The synthesis of boron nitride nanotubes by an extended vapour-liquid-solid method. *Nanotechnology*. **15**, 727 (2004).
3. R. Ma, Y. Bando, and T. Sato: CVD synthesis of boron nitride nanotubes without metal catalyst. *Chemical Physics Letters*. **337**, 61 (2001).
4. A. Goyal, D.A. Wiegand, F.J. Owens, and Z. Iqbal: Enhanced yield strength in iron nanocomposite with in situ grown single-wall carbon nanotubes. *Journal of Materials Research*. **21**, 522 (2005).
5. A. Goyal, D.A. Wiegand, F.J. Owens, and Z. Iqbal: Synthesis of carbide-free, high strength iron-carbon nanotube composite by in situ nanotube growth. *Chemical Physics Letters*. **442**, 365 (2007).
6. R. B. Patel, J. Liu, J. Eng, and Z. Iqbal: One-step CVD synthesis of a boron nitride nanotube-iron composite. *Journal of Materials Research*. **26**, 1332 (2011).
7. Foundation NANONET: *Nanorod, Nanowire*. Nanolectures 2010.
8. B. Wen, J.E. Sader, and J.J. Boland: Mechanical Properties of ZnO Nanowires. *Physical Review Letters*. **101**, 175502 (2008).
9. G. Stan, S. Krylyuk, A. V. Davydov, M. Vaudin, L. A. Bendersky and R. F. Cook: Surface effects on the elastic modulus of Te nanowires. *Applied Physics Letters*. **92**, 241908 (2008).
10. Y. Li, F. Qian and C. M. Lieber: Nanowire Electronic and Optoelectronic Devices. *Materials Today*. **9**, 10 (2006).
11. W. Auwarter, M. Muntwiler, M. Corso, T. Greber, and J. Osterwalder: *Ultrathin Hexagonal Boron Nitride (h-BN) films on metals*. University of Zurich, Physics Institute 2003 12/12/2003 [cited 2011 2/11/2011]; <http://www.physik.unizh.ch/groups/grouposterwalder/kospace/BNhome/BNhome.htm>
12. M. Prinsep: *Material World*. 2009 6/9/2009 [cited 2011 2/11/2011]; <http://sci.waikato.ac.nz/farm/curriculum/materialworld.html#allotropes>].
13. J. J. Fu, Y. N. Lu, H. Xu, K. F. Huo, X. Z. Wang, L. Li, Z. Hu and Y. Chen: The synthesis of boron nitride nanotubes by an extended vapour-liquid-solid method. *Nanotechnology*. **15**, 727 (2004).
14. Z. Hu, Y. Fan, and Y. Chen: Preparation and characterization of ultrafine amorphous alloy particles. *Applied Physics A*. **68**, 225 (1999).
15. Y. Chen: Chemical preparation and characterization of metal-metalloid ultrafine amorphous alloy particles. *Catalysis Today*. **44**, 3 (1998).
16. Z. Hu, Y. Fan, and Y. Chen: A study on the preparation and magnetic properties of Fe_{100-x}B_x ultrafine amorphous powders. *Materials Science and Engineering: B*. **25**, 193 (1994).
17. Z. Hu, Y. Wu, Y. Fan, Q. Yan, and Y. Chen: Chemical preparation and investigation of Fe- P-B ultrafine amorphous alloy particles. *Science in China Series B: Chemistry*. **40**, 261 (1997).

18. R. Ma, Y. Bando, and T. Sato: CVD synthesis of boron nitride nanotubes without metal catalysts. *Chemical Physics Letters*. **337**, 61 (2001).
19. D. Goldberg, Y. Bando, C. C. Tang, and C. Y. Zhi: Boron Nitride Nanotubes. *Advanced Materials*. **19**, 2413 (2007).
20. A. Krishnan, E. Dujardin, T. W. Ebbesen, P. N. Yianilos, M. M. J. Treacy: Young's modulus of single-walled nanotubes. *Physical Review B*. **58**, 14013 (1998).
21. M.M.J. Treacy, T.W. Ebbesen, and J.M. Gibson: Exceptionally high Young's modulus observed for individual carbon nanotubes. *Nature*. **381**, 678 (1996).
22. E.W. Wong, P.E. Sheehan, and C.M. Lieber: Nanobeam Mechanics: Elasticity, Strength, and Toughness of Nanorods and Nanotubes. *Science*. **277**, 1971 (1997).
23. J. Muster, M. Burghard, S. Roth, G. S. Duesberg, E. Hernández, and A. Rubio: Scanning force microscopy characterization of individual carbon nanotubes on electrode arrays. *Journal of Vacuum Science & Technology B: Microelectronics and Nanometer Structures*. **16**, 2796 (1998).
24. J.-P. Salvetat, G. A. D. Briggs, J.-M. Bonard, R. R. Bacsá, A. J. Kulik, T. Stockli, N. A. Burnham, L. Forro: Elastic and Shear Moduli of Single-Walled Carbon Nanotube Ropes. *Physical Review Letters*. **82**, 944 (1999).
25. M. R. Falvo, G. J. Clary, R. M. Taylor, V. Chi, F. P. Brooks Jr., S. Washburn, and R. Superfine: Bending and buckling of carbon nanotubes under large strain. *Nature*. **389**, 582 (1997).
26. S. Iijima, C. Brabec, A. Maiti, and J. Bernholc: Structural flexibility of carbon nanotubes. *The Journal of Chemical Physics*. **104**, 2089 (1996).
27. E. Hernandez, C. Goze, P. Bernier, A. Rubio: Elastic Properties of C and BxCyNz Composite Nanotubes. *Physical Review Letters*. **80**, 4502 (1998).
28. N.G. Chopra and A. Zettl: Measurement of the Elastic Modulus of a Multi-Wall Boron Nitride Nanotube. *Solid State Communications*. **105**, 297 (1997).
29. N.P. Bansal, J.B. Hurst, and S.R. Choi: Boron Nitride Nanotubes-Reinforced Glass Composites. *Journal of the American Ceramic Society*. **89**, 388 (2006).
30. J. C. Meyer, A. Chuvilin, G. Algara-Siller, J. Biskupek and U. Kaiser: Selective Sputtering and Atomic Resolution Imaging of Atomically Thin Boron Nitride Membranes. *Nano Letters*. **9**, 2683 (2009).
31. D. Pacilé, J. C. Meyer, Ç. Ö. Girit, and A. Zettl: The two-dimensional phase of boron nitride: Few-atomic-layer sheets and suspended membranes. *Applied Physics Letters*. **92**, 133107 (2008).
32. W.-Q. Han, L. Wu, Y. Zhu, K. Watanabe, and T. Taniguchi: Structure of chemically derived mono- and few-atomic-layer boron nitride sheets. *Applied Physics Letters*. **93**, 223103 (2008).
33. C.-H. Park and S.G. Louie: Energy Gaps and Stark Effect in Boron Nitride Nanoribbons. *Nano Letters*. **8**, 2200 (2008).
34. V. Barone, and J.E. Peralta: Magnetic Boron Nitride Nanoribbons with Tunable Electronic Properties. *Nano Letters*. **8**, 2210 (2008).
35. F. Zheng, G. Zhou, Z. Liu, J. Wu, W. Duan, B.-L. Gu, and S. B. Zhang: Half metallicity along the edge of zigzag boron nitride nanoribbons. *Physical Review B*. **78**, 205415 (2008).

36. A.J. Du, S.C. Smith, and G.Q. Lu: First-principle studies of electronic structure and C-doping effect in boron nitride nanoribbon. *Chemical Physics Letters*. **447**, 181 (2007).
37. J. C. Meyer, A. Chuvilin, G. Algara-Siller, J. Biskupek and U. Kaiser: Selective Sputtering and Atomic Resolution Imaging of Atomically Thin Boron Nitride Membranes. *Nano Letters*. **9**, 2683 (2009).
38. H. J. Ceragioli, A. C. Peterlevitz, J. C. R. Quispe, A. Larena, M. P. Pasquetto, M. A. Sampaio and V. Baranauskas: Synthesis and characterization of boron-doped carbon nanotubes. *Journal of Physics: Conference Series*, **100**, 052029 (2008).
39. A. Loiseau: Highly nitrogen and boron doped nanotubes: a route to synthesis and study of their properties by spatially resolved EELS. *American Physical Society Meeting*. (2005).
40. F.J. Owens: Boron and Nitrogen Doped Single Walled Carbon Nanotubes as Possible Dilute Magnetic Semiconductors. *Nano Express*. **2**, 447 (2007).
41. R.B. Sharma, D.J. Lateb, D.S. Joag, A. Govindaraj, C.N.R. Rao: Field emission properties of boron and nitrogen doped carbon nanotubes. *Chemical Physics Letters*. **428**, 102 (2006).
42. P. Redlich, J. Loeffler, P.M. Ajayan, J. Bill, F. Aldinger, M. Rühle: B-C-N nanotubes and boron doping of carbon nanotubes. *Chemical Physics Letters*. **260**, 465 (1996).
43. Z. Weng-Sieh, K. Cherrey, N.G. Chopra, X. Blase, Y. Miyamoto, A. Rubio, M.L. Cohen, R. Gronsky, S.G. Louie, A. Zettl: *Synthesis of B_xC_yN_z nanotubules*. *Physical Review B*. **51**, 11229 (1995).
44. D. Golberg, P. Dorozhkin, Y. Bando; M. Hasegawa; Z.-C. Dong: Semiconducting B-C-N nanotubes with few layers. *Chemical Physics Letters*. **362**, 353 (2002).
45. X. D. Bai, E. G. Wang, J. Yu, and H. Yang: Blue-violet photoluminescence from large-scale highly aligned boron carbonitride nanofibers. *Applied Physics Letters*. **77**, 67 (2000).
46. L. Liao, K. Liu, W. Wang, X. Bai, E. Wang, Y. Liu, J. Li, and C. Liu: Multiwall Boron Carbonitride/Carbon Nanotube Junction and Its Rectification Behavior. *Journal of the American Chemical Society Communications*. **129**, 9562 (2007).
47. J. D. Guo, C. Y. Zhi, X. D. Bai, and E. G. Wang: Boron carbonitride nanojunctions. *Applied Physics Letters*. **80**, 124 (2002).
48. R. Sharma, Z. Iqbal: In situ observations of carbon nanotube formation using environmental transmission electron microscopy. *Applied Physics Letters*, **84**, 990 (2004)
49. F. Danafara, A. Fakhru'l-Razi, M. A. M. Salleha, D. R. A. Biaka: Fluidized bed catalytic chemical vapor deposition synthesis of carbon nanotubes—A review. *Chemical Engineering Journal*, **155**, 37, (2009).
50. V. G. Dubrovskii, G.E. Cirlin, N. V. Sibirev, F. Jabeen, J. C. Harmand, P. Werner: New Mode of Vapor–Liquid–Solid Nanowire Growth. *Nano Letters*, **11**, 1247, (2011).
51. Wittke, J.H. *Microprobe-SEM*. 2008; Available from: <http://www4.nau.edu/microanalysis/Microprobe-SEM/Instrumentation.html>. Accessed 3/14/2013
52. Zaluzec, N.J. *XEDS*. Intro to AEM Lecture Notes 2010; Available from: <http://tpm.amc.anl.gov/Lectures/Zaluzec-4-XEDS.ppt.pdf>. Accessed 3/14/2013

53. Alexander, D. *Principles and Practice of Electron Diffraction*. 2010; Available from: http://cime.epfl.ch/files/content/sites/cime2/files/shared/Files/Teaching/MSE_603_2011_spring/Chapter%209-10%20-%20Diffraction.pdf. Accessed 3/14/2013
54. Krumeich, F. *Ewald Sphere of Diffraction*. 2012; Available from: <http://www.microscopy.ethz.ch/ED-Ewald.htm>. Accessed 3/11/2013
55. H. Tan, J. Verbeeck, A. Abakumov, G. Van Tendeloo: Oxidation state and chemical shift investigation in transition metal oxides by EELS. *Ultramicroscopy*, **116**, 24, (2012)
56. Muller, D. *Electron Energy Loss Spectroscopy*. Chemical Identification at the Nanoscale 2006; Available from: http://www.ccmr.cornell.edu/igert/modular/docs/4_Chemical_Identification_at_Nanoscale.pdf. Accessed 3/12/2013
57. Lios Technology: *Measuring Principle - Raman Effect*. 2013 Available from: <http://www.lios-tech.com/Menu/Technology/Measuring+Principle+-+Raman+Effect>. Accessed 3/14/2013
58. Andor Technology: *Raman Spectroscopy-An Introduction to Raman Spectroscopy*. 2013. Available from: <http://www.andor.com/learning-academy/raman-spectroscopy-an-introduction-to-raman-spectroscopy> Accessed 3/7/2013
59. University of Exeter: *Nonlinear Biophotonics-Surface Enhanced Raman Spectroscopy*. Biomedical Physics 2013 Available from: <http://emps.exeter.ac.uk/physics-astronomy/research/biomedical/research-interests/biophotonics/sers/>. Accessed 3/14/2013
60. A. P. Schuetze, W. Lewis, C. Brown, W. J. Geerts: A laboratory on the four-point probe technique. *American Association of Physics Teachers*, 72, 149, (2004).
61. Newport. *Introduction to FTIR Spectroscopy*. 2013 Available from: <http://www.newport.com/Introduction-to-FT-IR-Spectroscopy/405840/1033/content.aspx>. Accessed 3/14/2013
62. CALCE. *Material Hardness*. 2001; Available from: http://www.calce.umd.edu/TSFA/Hardness_ad_.htm. Accessed 3/14/2013
63. N.E.R. Center. *Compressive, Bearing, & Shear Properties*. 2012; Available from: <http://www.nd-ted.org/EducationResources/CommunityCollege/Materials/Mechanical/Compression.htm>. Accessed 3/14/2013
64. F. M. Dunnivant, J. W. Ginsbach. *Flame Atomic Absorbance and Emission Spectrometry and Inductively Coupled Plasma-Mass Spectrometry*, W. Laxson, M. Beck, N. Lien, K. Nicolaysen, M. F. Polivka, N. James, H. Main, P. DaRosa, Editor 2011, Whitman College: Walla Walla, WA.
65. Moeck, P. *X-ray Diffraction*. 2004; Available from: <http://web.pdx.edu/~pmoeck/phy381/Topic5a-XRD.pdf>. Accessed 3/14/2013
66. R. Ma, Y. Bando: Investigation on the Growth of Boron Carbide Nanowires. *Chemistry of Materials*. **14**, 4403 (2002).
67. D. Zhang, D.N. McIlroy, Y. Geng, M. G. Norton: Growth and characterization of boron carbide nanowires. *Journal of Materials Science Letters*. **18**, 349 (1999).
68. L. Hongxia, Z. Heming, S. Jiuxu, Z. Zhiyong: Electronic structures of an (8, 0) boron nitride/carbon nanotube heterojunction. *Journal of Semiconductors*. **31** (2010).

69. D. Golberg, Y. Bando, M. Mitome, K. Fushimi, C. Tang: Boron nitride nanotubes as nanocrucibles for morphology and phase transformations in encapsulated nanowires of the Mg–O system. *Acta Materialia*. **52**, 3295 (2004).
70. J. Szmids, A. Werbowy, L. Jarzebowski, T. Gebicki, I. Petrakova, A. Sokolowska, and A. Olszyna: Effect of annealing on the structure and electrical properties of sulfur-doped amorphous c-BN layers. *Journal of Materials Science*. **31**, 2609 (1996).
71. Y. Yokota, S. Tagawa, and T. Sugino: Planar field emitters fabricated by sulfur-doped boron nitride. *Journal of Vacuum Science & Technology B: Microelectronics and Nanometer Structures*. **17**, 642 (1999).
72. S. Sharma, P. Rani, A.S. Verma, and V.K. Jindal: Structural and electronic properties of sulphur-doped boron nitride nanotubes. *Solid State Communications*. **152**, 802 (2012).
73. C. J. Otten, O.R. Lourie, M.-F. Yu, J. M. Cowley, M. J. Dyer, R. S. Ruoff, and W. E. Buhro: Crystalline Boron Nanowires. *JACS Communications*. **2002**, 4564 (2002).
74. E. Y. Zarechnaya, L. Dubrovinsky, N. Dubrovinskaya, N. Miyajima, Y. Filinchuk, D. Chernyshov, and V. Dmitriev: Synthesis of an orthorhombic high pressure boron phase. *Science and Technology of Advanced Materials*. **9**, (2008).
75. J. Nagamatsu, N. Nakagawa, Takahiro Muranaka, Yuji Zenitani and Jun Akimitsu: Superconductivity at 39 K in magnesium diboride. *Letters to Nature*. **410**, 63 (2001).
76. Y. Zenitani and J. Akimitsu: Discovery of the new superconductor MgB₂ and its recent development. *JSAP International (Cutting Edge)*. **6**, (2002).
77. Y. Wu, B. Messer, and P. Yang: Superconducting MgB₂ Nanowires. *Advanced Materials*. **13**, 1487 (2001).
78. L. Ci, Z. Rao, Z. Zhou, D. Tang, X. Yan, Y. Liang, D. Liu, H. Yuan, W. Zhou, G. Wang, W. Liu, and S. Xie: Double wall carbon nanotubes promoted by sulfur in a floating iron catalyst CVD system. *Chemical Physics Letters*. **359**, 63 (2002).
79. M.S. Motta, A. Moiala, I.A. Kinloch, and A.H. Windle: The Role of Sulphur in the Synthesis of Carbon Nanotubes by Chemical Vapour Deposition at High Temperatures. *Journal of Nanoscience and Nanotechnology*. **8**, 2442 (2008).
80. G. G. Tibbetts, C.A. Bernardo, D. W. Gorkiewicz, and R. L. Alig: Role of sulfur in the production of carbon fibers in the vapor phase. *Carbon*. **32**, 569 (1994).
81. Hodkiewicz, J. *Characterizing Carbon Materials with Raman Spectroscopy*. 2010; Available from: <https://fscimage.thermoscientific.com/images/D19504~.pdf> Accessed 3/13/13
82. Schwartz, D. T. *Raman Spectroscopy: Introductory Tutorial*. Available from: <http://depts.washington.edu/ntuf/facility/docs/NTUF-Raman-Tutorial.pdf> Accessed 3/13/13
83. G. Liu, Q. Fang, W. Xu, H. Chen, C. Wang: Vibration assignment of carbon–sulfur bond in 2-thione-1,3-dithiole-4,5-dithiolate derivatives. *Spectrochimica Acta Part A: Molecular and Biomolecular Spectroscopy*. **60**, 541 (2004).
84. X. Q. Yan, W. J. Li, T. Goto, and M. W. Chen: Raman spectroscopy of pressure-induced amorphous boron carbide. *Applied Physics Letters*. **88**, 131905 (2006).
85. R. Ma, Y. Bando, and T. Sato: CVD synthesis of boron nitride nanotubes without metal catalyst. *Chemical Physics Letters*. **337**, 61 (2001).

86. Y. Xue, Q. Liu, G. He, K. Xu, L. Jiang, X. Hu, and J. Hu: Excellent electrical conductivity of the exfoliated and fluorinated hexagonal boron nitride nanosheets. *Nanoscale Research Letters*. **8**, (2013).
87. C. Tang, Y. Bando, Y. Huang, S. Yue, C. Gu, F. F. Xu, and D. Golberg: Fluorination and Electrical Conductivity of BN Nanotubes. *Journal of American Chemical Society*. **127**, 6552 (2005).
88. T. L. Mitran, A. Nicolaev, G. A. Nemnes, L. Ion, and S. Antohe: Magnetic behavior and clustering effects in Mn-doped boron nitride sheets. *Journal of Physics: Condensed Matter*. **24**, (2012).
89. G. A. Nemnes: Spin current switching and spin-filtering effects in Mn-doped boron nitride nanoribbons. *Journal of Nanomaterials*. **2012**, (2012).
90. H.S. Kang: Theoretical Study of Boron Nitride Nanotubes with Defects in Nitrogen-Rich Synthesis. *Journal of Physical Chemistry B*. **110**, 4621 (2006).
91. J. Szmidt, A. Werbowy, L. Jarzebowski, T. Gebicki, I. Petrakova, A. Sokolowska, and A. Olszyna: Effect of annealing on the structure and electrical properties of sulfur-doped amorphous c-BN layers. *Journal of Materials Science*. **31**, 2609 (1996).
92. Y. Yokota, S. Tagawa, T. Sugino: Planar field emitters fabricated by sulfur-doped boron nitride. *Journal of Vacuum Science & Technology B: Microelectronics and Nanometer Structures*. **17**, 642 (1999).
93. S. Sharma, P. Rani, A.S. Verma, V.K. Jindal: Structural and electronic properties of sulphur-doped boron nitride nanotubes. *Solid State Communications*. **152**, 802 (2012).
94. W.A. Curtin and B.W. Sheldon: CNT-reinforced ceramics and metals. *Mater. Today* **7**, 44 (2004).
95. Z. Iqbal and A. Goyal: Carbon nanotubes/nanofibers and carbon fibers in, *Functional Fillers for Plastics*, edited by M. Xanthos (WILEY-VCH Verlag, Berlin, Germany, 2005), p. 175.
96. G. Van Lier, C. Van Alsenoy, V. Van Doren, and P. Geerlings: Ab initio study of the elastic properties of single-walled carbon nanotubes and graphene. *Chem. Phys. Lett.* **326**, 181 (2000).
97. D. Sanchez-Portal, E. Artacho, J.M. Soler, A. Rubio, and P. Ordejon: Ab initio structural, elastic, and vibrational properties of carbon nanotubes. *Phys. Rev. B*. **59**, 12678 (1999).
98. E. Hernandez, C. Goze, P. Bernier, and A. Rubio: Elastic properties of C and B_xC_yN_z composite nanotubes. *Phys. Rev. Lett.* **80**, 4502 (1998).
99. J.P. Lu: Elastic properties of carbon nanotubes and nanoropes. *Phys. Rev. Lett.* **79**, 1297 (1997).
100. B.I. Yakobson, M.P. Campbell, C.J. Brabec, and J. Bernholc: High strain rate fracture and C-chain unraveling in carbon nanotubes. *Comp. Mater. Sci.* **8**, 341 (1997).
101. M.M.J. Treacy, T.W. Ebbesen, and J.M. Gibson: Exceptionally high Young's modulus observed for individual carbon nanotubes. *Nature* **381**, 678 (2002).
102. E.W. Wong, P.E. Sheehan, and C.M. Lieber: Nanobeam mechanics: Elasticity, strength, and toughness of nanorods and nanotubes. *Science* **277**, 1971 (1997).
103. J.P. Salvetat, J.M. Bonard, N.H. Thomson, A.J. Kulik, L. Forró, W. Benoit, and L. Zuppiroli: Mechanical properties of carbon nanotubes. *Appl. Phys. A*. **69**, 255 (1999).

104. A. Krishnan, E. Dujardin, T.W. Ebbesen, P.N. Yianilos, and M.M.J. Treacy: Young's modulus of single-walled nanotubes. *Phys. Rev. B.* **58**, 14013 (1998).
105. A. Goyal, D. A. Weigand, F.J. Owens and Z. Iqbal: Enhanced yield strength in iron nanocomposite with in situ grown single-wall carbon nanotubes. *J. Mater. Res.*, **21**, 2, (2006).
106. A. Goyal, D. Wiegand, F.J. Owens, and Z. Iqbal: Synthesis of carbide-free, high strength iron-carbon nanotube composite by in situ nanotube growth. *Chemical Physics Letters Volume*, **442**, 365 (2007).
107. N. G. Chopra and A. Zettl: Measurement of the Elastic Modulus of a Multi-Wall Boron Nitride Nanotubes. *S. S. communications*, **105**, 297 (1998).
108. J. H. Lee: A Study on a Boron-Nitride Nanotube as a Gigahertz Oscillator. *Journal of the Korean Physical Society*, **49**, 1 (2006).
109. O. R. Lourie, C. R. Jones, B. M. Bartlett, P. C. Gibbons, R. S. Ruoff, and W. E. Buhro: CVD Growth of Boron Nitride Nanotubes. *Chem. Mater.*, **12**, 1808 (2000).
110. R. Ma, Y. Bando, T. Sato: CVD Synthesis of Boron Nitride Nanotubes without metal catalysts. *Chemical Physics Letters*. **337**, 61 (2001).
111. D. Golberg, Y. Bando, K. Kurashima, T. Sato: Synthesis and characterization of ropes made of BN multiwalled nanotubes. *Scripta Materialia*. **44**, 1561, (2001).
112. X. Chen, P. Wu, M. Rousseas, D. Okawa, Z. Gartner, A. Zettl, and C. R. Bertozzi: Boron Nitride Nanotubes Are Noncytotoxic and Can Be Functionalized for Interaction with Proteins and Cells. *J. Am. Chem. Soc.* **131** (2009) p. 890.
113. C.W. Lam, J. McCluskey, R. L. Hunter: Pulmonary toxicity of single-wall carbon nanotubes in mice 7 and 90 days after intratracheal instillation. *Toxicological Sciences*. **77**, 126 (2004).
114. J. J. Fu, Y. N. Lu, H. Xu, K. F. Huo, X. Z. Wang, L. Li, Z. Hu, and Y. Chen: The synthesis of boron nitride nanotubes by an extended vapour-liquid-solid method. *Nanotechnology*. **15**, 727, (2004).
115. S. R. Choi, N. P. Bansal, A. Garg: Mechanical and microstructural characterization of boron nitride nanotubes-reinforced SOFC seal glass composite. *Materials Science and Engineering: A Volumes*. **460-461**, 509, (2007).
116. Hu Z, Fan Y, Chen F and Chen Y: Amorphous iron-boron powders prepared by chemical reduction of mixed-metal cation solutions: dependence of composition upon reaction temperature. *J. Chem. Soc.: Chem. Commun.* 247 (1995).
117. Hu Z, Fan Y and Chen Y: Preparation and characterization of ultrafine amorphous alloy particles. *Appl. Phys. A*. **68**, 225, (1999).
118. J. Jiang, I. D'ezsi, U. Gonser and X. Lin: A study of the Preparation Conditions of Fe-B Powders Produced by Chemical Reduction. *J. Non-Cryst. Solid*, 124 (1991).
119. R. Arenal, A. C. Ferrari, S. Reich, L. Wirtz, J. Y. Mevellec, S. Lefrant, A. Rubio, and A. Loiseau: Raman Spectroscopy of Single-Wall Boron Nitride Nanotubes. *Nano Letters*. **6**, 1812, (2006).
120. Z. W. Gan, X. X. Ding, Z. X. Huang, X. T. Huang, C. Cheng, C. Tang, S.R. Qi: Growth of Boron Nitride Nanotube Film in Situ. *Appl. Phys. A*. **81**, (2005).
121. S. Sen, E. Schofield, J. S. O'Dell, L. Deka, and S. Pillay: The Development of a Multifunctional Composite Material for Use in Human Space Exploration Beyond Low-Earth Orbit. *JOM*, **61**, 23.

122. M. W. Smith, K. C. J, C. Park, J .Kim, P. T. Lillehei, R. Crooks, and J. S. Harrison: Very long single- and few-walled boron, nitride nanotubes via the pressurized vapor/condenser method. *Nanotechnology*. 20. (2009).
123. W. Zhong, G. Overney, and D. Tomanek: Structural Properties of Fe Crystals. *Physical Review B*. **47**, (1993).

APPENDIX A

NOVEL SYNTHESIS ROUTE OF GRAPHENE USING IRON NANOPARTICLES

A.1 Summary

Graphene is currently one of the most heavily researched materials, for extremely good reasons. It displays a number of characteristics which are unique and could be exploited for industrial applications. One drawback of graphene is its high cost of fabrication. A number of methods are available currently; however, few are viable for large scale production of high quality graphene. The research done here entails a novel growth mechanism for graphene using a chemical vapor deposition (CVD) process. The catalyst is a commercially available iron powder. This process is easily scalable, flexible, and produces a large volume of high quality graphene sheets. The material produced was examined using Raman spectroscopy and electron microscopy. This is the first reported method of using nanoparticles to synthesize graphene using a CVD process. This is unique as one would normally expect multiwalled carbon nanotubes to result from the growth conditions, which necessitates the description of a novel growth mechanism.

A.2 Introduction

Graphene has attracted significant interest over the years since its Nobel worthy discovery in 2003 [1, 2]. The number of interesting properties possessed by graphene is fantastic: it is incredibly strong, can support ballistic fermions, displays chiral quantum effects, is a zero band gap semiconductor, and can support conduction without charge carriers [3]. Due to its remarkable properties, graphene would find use in a number of

industrial applications. However, a significant hindrance in the commercialization of graphene is that the scaled up production of the material is not straightforward. Graphene can be synthesized using mechanical exfoliation, reduction of graphite oxide layers, and epitaxial growth on SiC wafers. These methods have flaws and advantages naturally; however, for large-scale bulk production they are ultimately limited. Graphene can also be synthesized using chemical vapor deposition processes, usually using a copper or nickel substrate [3]. These specific CVD methods tend to prohibit economically viable manufacturing because they must usually be performed on a foil or thin film. If the graphene could be grown using easily manufactured catalyst particles, the cost of graphene could fall precipitously, perhaps coming in line with multi walled nanotubes. Nickel particles were previously used to grow graphene, but there are some possible improvements that could be made to the method. The process used micron (generally $<30\ \mu\text{m}$) sized particles, which have a low surface area, negatively impacting yield, though it will make larger area graphene sheets [4]. Additionally, copper and nickel are the material of choice normally to grow graphene [5-8], although iron is particularly useful for the growth of carbon nanostructures, and iron film has been shown to grow graphene [9, 10]. For commercial purposes, if iron is used, a number of structural applications become possible. This is because iron is naturally very strong, especially when it has a particle size in the nano-regime [11], and easily joins carbon structures [12-15]. (Carbon is highly soluble in iron, as opposed to nickel and copper, which makes the formation of few layered graphene with it difficult, however, this also possibly makes bonding between graphene and iron much stronger).

The growth of graphene onto nanoparticles seems unlikely, as normally, if particles of this type are used, amorphous carbon or nanotubes result [12-16]. Theoretically, there are two possible paths for the formation of graphene onto nanoparticles. One is a ‘flower’ based model, and the other is a ‘wall’ based model. The flower based model would involve layers of carbon encircling iron catalysts, and once a critical point in the deposition was reached, they would fold out. (In this case, the catalysts are like the ovule in the flower, while the petals are the graphene sheets.) A wall based model would have them growing vertically, on top of an iron particle, essentially giving the iron particle ‘fins’. A wall based model would create graphene with dimensions limited by the circumference of the nanoparticles, while a flower based model would create graphene limited by the surface area of the particle(s). Determination of the likely model of growth was a goal of the researchers. (Note: Evaluation of thickness was difficult with available experimental equipment, therefore the term ‘graphene’ here can relate to single layered sheets to those containing up to 10-15 layers, commonly referred to as graphitic nanoplatelets.)

A.3 Experimental

Graphene was grown by chemical vapor deposition (CVD) infiltration onto iron catalyst powders (20 nm and 100 nm, see Figure A.1) purchased from American Elements. The iron nanopowder was placed in a 2.5 cm diameter quartz tube in a 3-zone high temperature furnace controlled externally by a three point microprocessor temperature controller (Applied Systems Inc). A mechanical pump was used to provide a vacuum for the system at 10^{-3} Torr, and the reactor was then back-filled with argon to atmospheric

pressure before beginning the deposition experiment. Argon (Matheson, 99.999 % ultra-high purity) was the inert carrier gas, and carbon monoxide (Matheson, 99.9 % research grade) and acetylene (Matheson, 99.6 %) were used as the carbon sources. Carbon monoxide gas was added to prevent the formation of metal carbides as discussed by Goyal et al. [14].

The quartz reaction tube of the CVD system (Figure A.1, Bottom) was pumped down to 10^{-3} torr, backfilled with pure argon, and heated to 800 °C at the rates of 10 °C and 33 °C per minute (33 °C is the maximum heating rate of the CVD system used). As soon as the temperature approached 800 °C, the gas flow was switched to acetylene, carbon monoxide, and argon with flow rates of 6, 100 and 300 sccm (standard cubic centimeters per minute) at ambient pressure, respectively. The power was shut down after 30 minutes of reaction time. The system was then allowed to cool under flowing argon. The powder was noticeably darkened by graphene deposition. This was the basic method based on processes used successfully to grow nanotubes [12-14, 16], but was varied to elucidate which reaction gases were critical. Each gas was removed in a run once. Two runs were done with methane in lieu of acetylene, due to their similar chemistry (since methane decomposes at a high temperature the reaction was done both at 800° C and 985° C). In the case of the most promising run, the product from the CVD reaction was purified using 2 M nitric acid. The variations of the method are given in Table A.1.

Use of chemical vapor infiltration was considered a possibility to create nano iron-graphene composites in the same vane as the following references [12-14, 16]. Essentially, graphene is grown directly into a metal pellet containing the catalyst. The hope was that the graphene would join metal nanoparticles, effectively creating a material

with superior mechanical properties in comparison to neat metals. However, this method failed to produce materials of hardness greater than that of pristine, graphene-less samples. Why this is true is open to speculation, but possibly graphene may not reinforce metals as readily as carbon nanotubes due to differences in geometry or how they bound to metals. Additionally, if the flower model is true, reinforcement is extremely unlikely, as the graphene once formed would rarely ever dissolve into the iron, creating the bonding needed for mechanical enhancement. The wall model would be more likely to reinforce the metal, since the graphene is growing directly from a particle and is already joined to it.

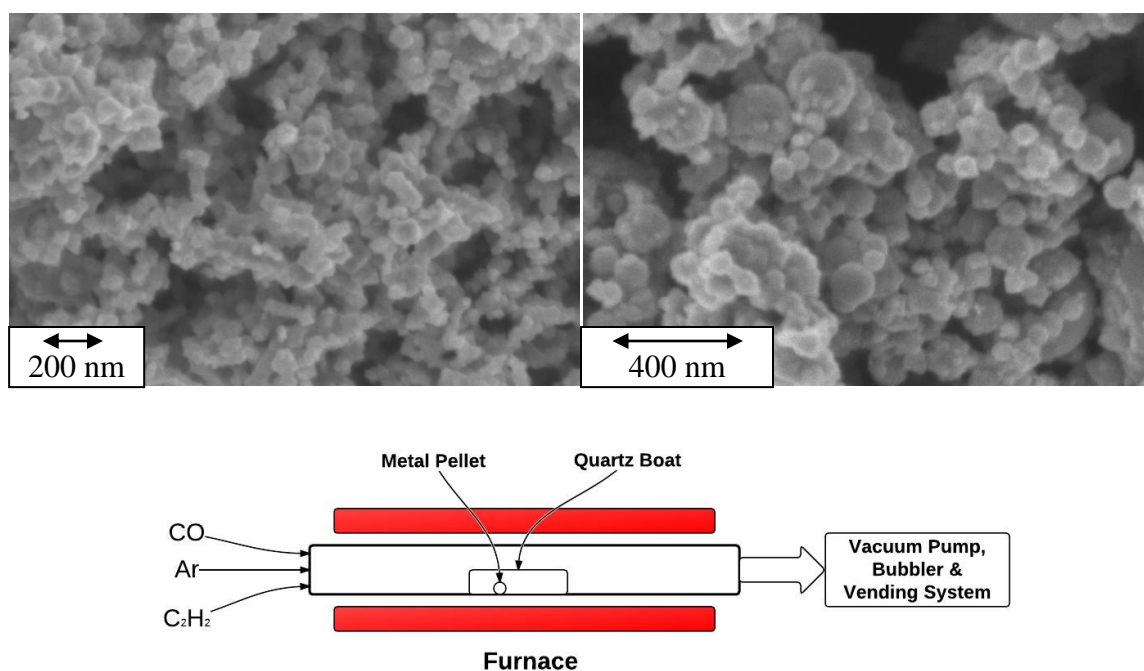


Figure A.1 (Top Left) 20 nm iron purchased from American Elements. (Top Right) 100 nm iron purchased from same source. (Bottom) Diagram of chemical vapor deposition set up used in experiments.

Table A.1 Table Detailing which Experimental Runs were Performed

	Particle Size of Catalyst	Heating Rate	Argon (300 sccm)	Acetylene (6 sccm)	Carbon Monoxide (100 sccm)
A	20 nm	10° C	X	X	X
B	100 nm	10° C	X	X	X
C	20 nm	33° C		X	X
D	20 nm	33° C	X		X
E	20 nm	33° C	X	X	
F	20 nm	33° C	X	X	X
G	Sample F Purified with 6 M Nitric Acid				
H (@ 800° C and 985° C)	20 nm	33° C	X	(Methane 6 sccm)	X

Scanning Electron Microscopy (SEM): SEM images were obtained with a VP-1530 Carl Zeiss LEO (Peabody, MA) field emission scanning electron microscope. The samples were mounted on aluminum stubs using double-sided carbon tape.

Raman Spectroscopy: Raman spectra were obtained using a confocal Horiba-Jobin Yvon LabRam micro-Raman spectrometer with a 20 mW HeNe laser source emitting at a wavelength of 632.8 nm focused to a spot size of 10 μm with a 10x lens. The Raman conditions for Sample A, B, and F follow: D2 Filter, 300 μm hole, 200 μm slit, 2x60 sec acquisition time. The Raman conditions for Sample C, D, E, G, and H follow: D0.3 Filter, 300 μm hole, 200 μm slit, 2x15 sec acquisition time. All spectra given in the Appendix use units cm^{-1} .

Transmission Electron Microscopy (TEM): A CM-20 FEG S/TEM was used to study the sample either under bright field TEM imaging or EELS analysis in STEM mode. TEM microscopy was performed on the product using 20 nm catalyst with argon, acetylene, and carbon monoxide before and after purification. The samples were prepared using light sonication in ultra pure methanol, and placing one 1 μ L drop on a 300 mesh lacey carbon grid sitting on a filter paper. The TEM grid was then placed in a vacuum oven to dry.

A.4 Results

The Raman spectrum of graphene and graphite are well known. The characteristic features are the D band, the G band, and the harmonics of those bands. The D band is a measure of the disorder in graphite materials. The G band arises from the SP^2 orbital bonding of the material. Raman and SEM were performed to initially investigate which growth conditions were promising (Figure A.2). Sample A shows a very high intensity D band (1330 cm^{-1}), and a 2D band (2661 cm^{-1}) which is of greater intensity than the G band (1582 cm^{-1}). This is a characteristic sign of the formation of graphene. From the Raman and SEM images, it seems to be a mixture of few layered graphene [17]. There is an occasional nanotube present in the mixture of materials as well.

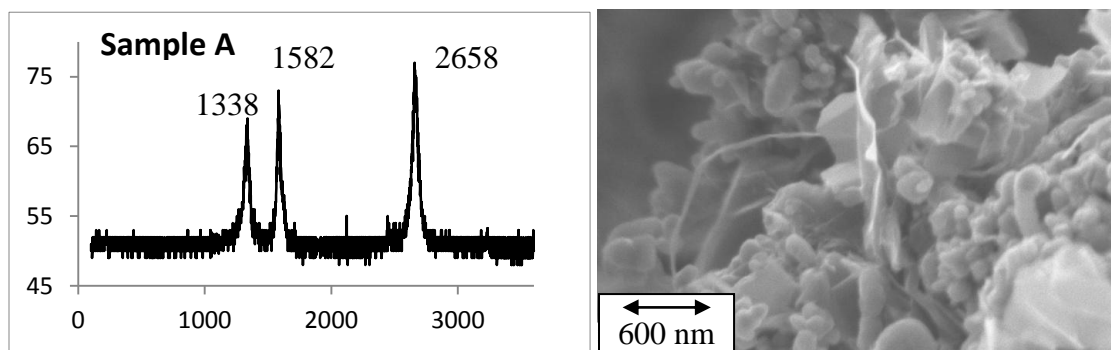


Figure A.2 (Left) Raman spectrum of Sample A, x units in cm^{-1} and y axis is intensity. (Right) Graphene growing on catalyst in Sample A.

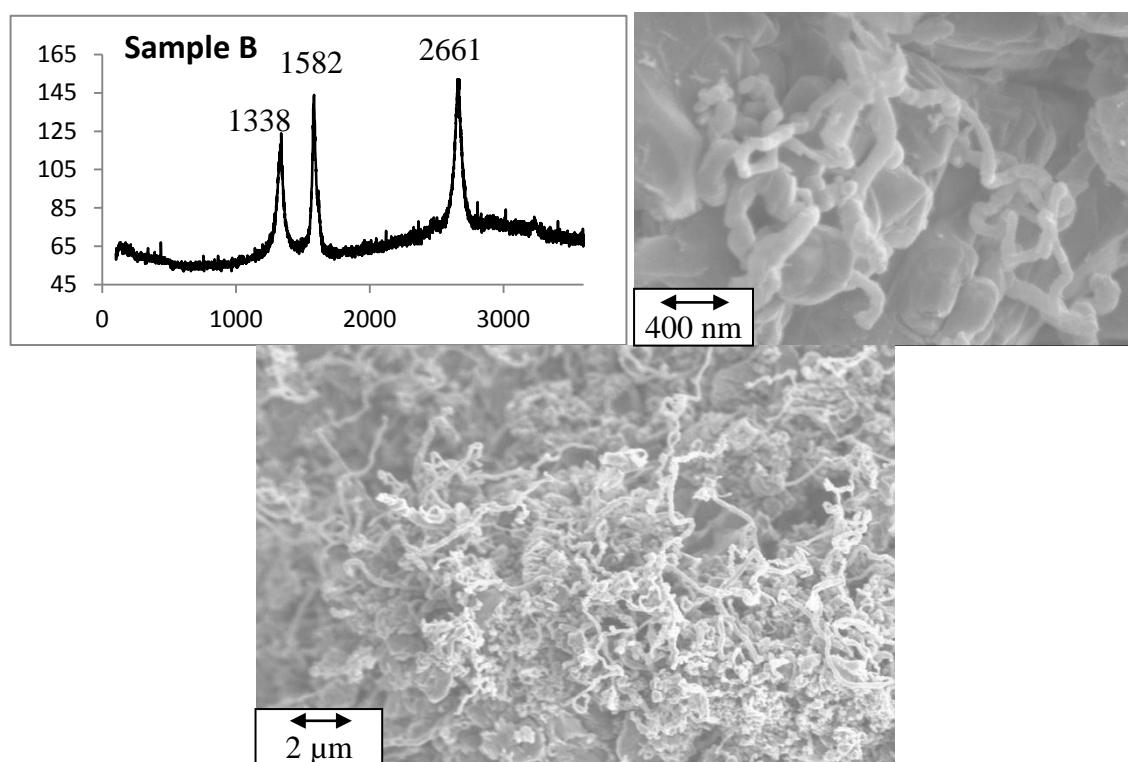


Figure A.3 (Top Left) Raman of Sample B x units in cm^{-1} and y axis is intensity. (Top Right) SEM image of Sample B, showing a number of nanotubes populating an area. (Bottom) Nanotubes and graphene covering a large area of Sample B.

Sample B, which uses the 100 nm catalyst, gives interesting results as well (Figure A.3). The D band is at 1338 cm^{-1} , like in Sample A, but the G band is shifted slightly down, to 1580 cm^{-1} . The 2D band is also at 2661 cm^{-1} , instead of 2658 cm^{-1} . This is within the error of the machine. A large degree of inelastic background scattering

and some light fluorescence is also evident. There is a high ratio between the D and G band in the spectrum, indicating a great number of defects. Additionally, there is a strong enhancement in the 2D band which shows the production of graphene. SEM analysis indicated that there was not as a ubiquitous coverage of the metal catalyst as in the case of the 20 nm catalyst, therefore, further experiments with the 100 nm catalyst were suspended. Graphene was found, however, not nearly in the amount that was found when examining Sample A. Instead, more multiwalled carbon nanotubes were present. This indicates the larger particle sized catalyst was not as useful for the growth of graphene.

Samples C-F were done with the 20 nm catalyst using a faster heating rate (Raman spectra given in Figure A.4). This was because some ripening was noticed when examining the 20 nm catalyst at a lower heating rate, and the 100 nm catalyst seemed to have a lower amount of graphene in the SEM. This leads to the conclusion that a faster heating rate with the smallest initial catalyst would give the best results, as that would minimize the particle size of the catalyst used, presumably improving graphene growth. Sample C was grown under these conditions and without argon, to show the affect argon has on the system. Argon seems to not play a critical role as the catalyst still easily grew the graphene. The Raman spectrum shows some growth of graphene, as the 2D band is higher than what would be expected for pure graphite. However, the 2D band is not nearly as pronounced as in Sample E or F. This might hint that the argon encourages the growth of fewer layered graphene. Additionally, the D band is very small; the measured ratio of D/G for Sample C is smaller than that of any other material in the study, which shows the disorder in the material is extremely low. This may hint that the presence of argon, for whatever reason, induces defects into the graphene structure. The 3200 cm^{-1}

peak, the 2G peak, is also evident in the sample, another indication of the quality of the material. SEM analysis of Sample C was indistinguishable from that of Sample F (Figure A.5).

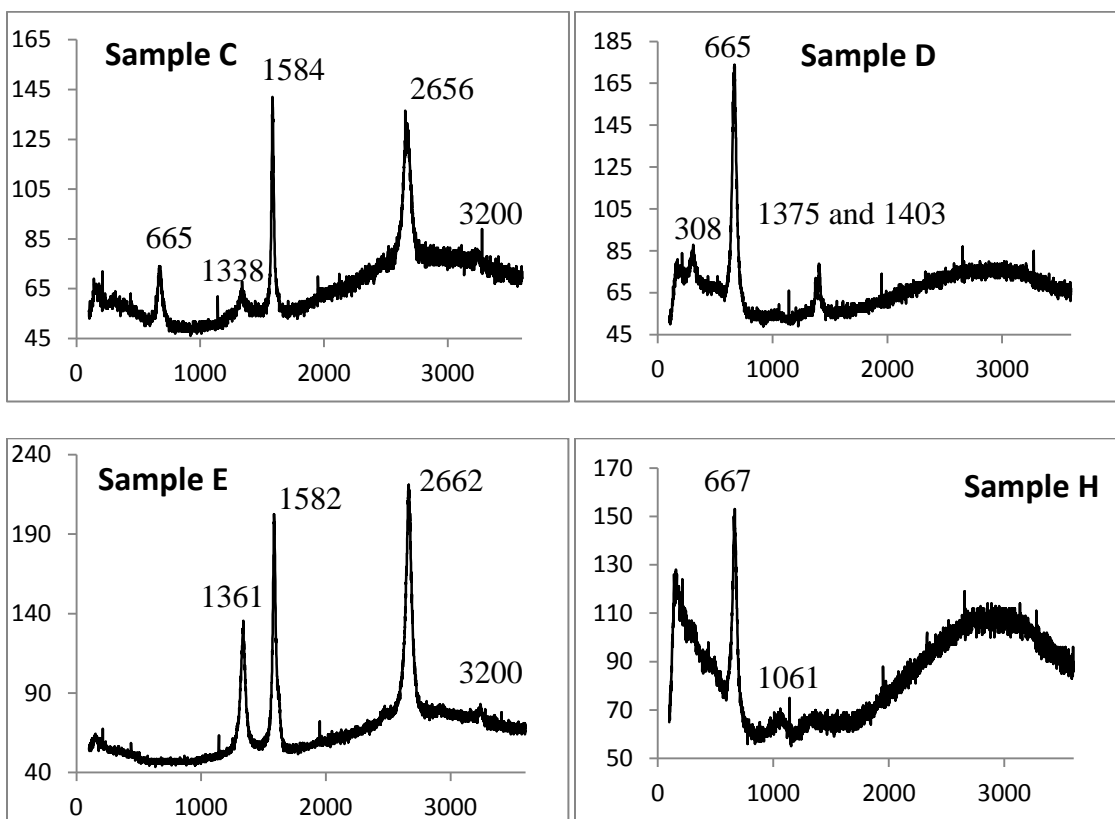


Figure A.4 (Top Left) Raman Spectrum of Sample C, x units in cm^{-1} and y axis is intensity. (Top Right) Raman Spectrum of Sample D. (Bottom Left) Raman Spectrum of Sample E. (Bottom Right) Raman Spectrum of Sample H.

Sample D was performed with a fast heating rate using the 20 nm catalyst, and no acetylene was used. This sample indicated very little growth of graphene on the catalyst when analyzed using SEM, and even visually, the catalyst did not darken like the other materials in the study. Also, the Raman spectrum gives no indication of the growth of graphene. However, the material did change somewhat. There is a strong line at 665 cm^{-1} , a weak broad peak at 308 cm^{-1} , and a twin peak at 1375 cm^{-1} and 1403 cm^{-1} . These might correspond to the formation of some sort of iron carbide; however, it does not seem

to correlate with graphene. This indicates acetylene is the key gas for the growth of graphene in the system, as shown in [9, 10].

Sample E was done without carbon monoxide. While the ratio of the G/2D band demonstrates the growth of graphene, the product does not have as much few layered graphene as Sample F. The D/G ratio is acceptable, however, it can be considered to be high considering the measured D/G ratio for other materials in this study. The high defect rate for Sample E, coupled with the low defect rate of Sample C, might hint that a high carbon monoxide/argon ratio results in a less defective structure. The 2G peak is also visible in the Raman spectrum of this sample. SEM images were indistinguishable from Sample F (Figure A.5).

Sample H was performed with methane as opposed to acetylene. This was to test whether a similar carbon containing gas, except with less carbon per mol of gas would give fewer layers. The methane results indicate that there is no graphene growth present. There is a strong peak at 667 cm^{-1} , comparable to the peak shown when no acetylene was used, like in Sample D, but other than that, there are no common peaks present. Using a higher temperature did not change the results significantly. SEM analysis also did not show the growth of any nanostructures.

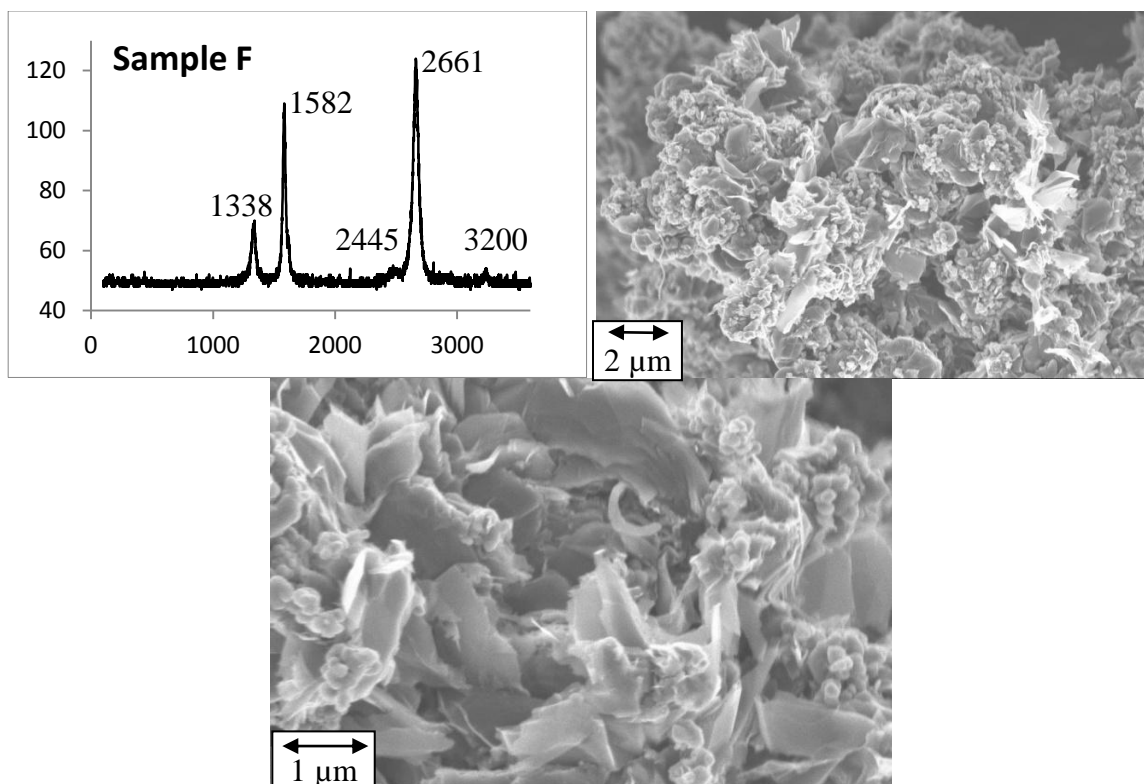


Figure A.5 (Top Left) Raman spectra from Sample F, x units in cm^{-1} and y axis is intensity, this is the highest quality graphene made in the study. (Top Right) SEM image of Sample F, note the growth of a large number of graphene sheets on the surface of the particles. (Bottom) Zoomed in image showing an area with a particularly dense concentration of graphene sheets.

Sample F was arguably the best sample in the study (Figure A.5). This sample showed a wide coverage of graphene, and the lowest ratio between G/2D, indicating the growth of the most few layered graphene. Additionally, the D/G ratio was the second lowest in the study, only surpassed by Sample C. There is a visible, strong 2G peak. While not critical, the presence of carbon monoxide and argon may help to grow higher quality graphene, or they may simply act as diluents, indicating a lower concentration of acetylene flow results in a product with fewer layers. Future experiments will need to look into gas flow rates and different types of carrier gases. The SEM analysis was also highly encouraging, showing a great deal of graphene growing on the surface of the

catalyst. Sample F was purified with nitric acid, to demonstrate that the metal can be removed, leaving pure graphene, which is Sample G (Figure A.6).

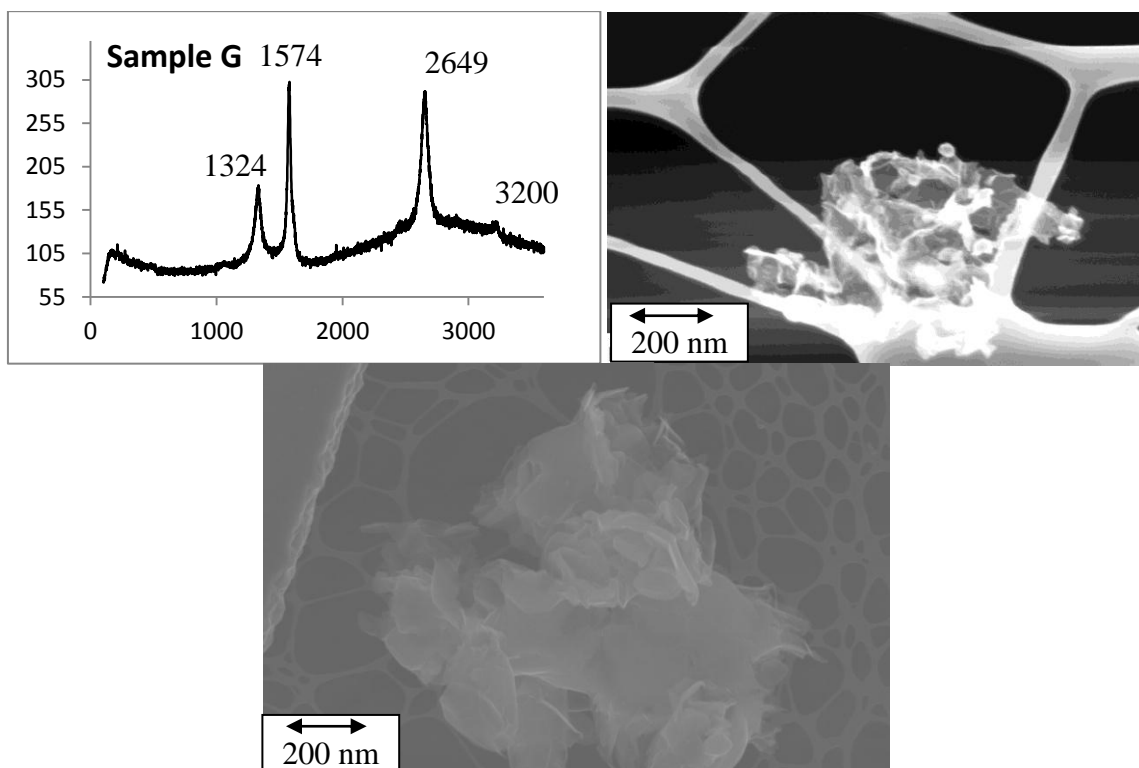


Figure A.6 (Top Left) Raman spectrum of Sample G, x units in cm^{-1} and y axis is intensity. (Top Right) SEM image of product of Sample G placed on TEM grid, note that it is so thin that the grid can easily be seen underneath. (Bottom) Large area of graphene sheets found on the TEM grid.

To summarize the results (done so in Table A.2), the least defective sample was Sample C, followed by Sample F. Additionally, Sample F showed the highest growth of fewer layered graphene. Sample F was deemed the most attractive material for further study, which is why Sample G was created from it. The purpose of Sample G was to show that the graphene could be isolated through the use of nitric acid. While the Raman results are not as impressive before the separation, further refining of the entire process might result in a much more consistent product. Another interesting note is that there is no shoulder in the 2D peak that would be expected if the material was pure graphite, and

there is a significant enhancement in the 2D peak, another indication of the growth of graphene. Figure A.6 shows the SEM done on Sample G after it was deposited on a lacey carbon TEM grid. The material is mostly very thin flakes, thin enough to appear translucent under SEM. A large number of flakes result, though separating the layers is difficult. Some folds are evident, indicating there may be some defects in the graphene structure. While the SEM and Raman analysis are revealing, ultimately, high quality TEM was required to fully understand the material.

Table A.2 Table Summarizing Results of Raman Intensity Ratios for the Samples in the Study. ‘Not Available’ Indicates no Graphene was Grown. Sample F Seemed to be the Highest Quality Material Available. D/G Ratio Could be an Indication of the Amount of Defects in the Graphene, and G/2D Ratio Could be an Indication of the Number Layers

Sample	D/G	G/2D
A	0.81	0.84
B	0.77	1.05
C	0.16	1.47
D	Not Available	
E	0.56	1.06
F	0.37	0.79
G	0.46	1.26
H	Not Available	

Transmission electron micrography was performed on Sample F. Sample F shows clear indications of the growth of graphene. Note in Figure A.7, the presence of facets and folds. Diffraction analysis shows that it is indeed few layered graphene, because the layer spacing is $\approx 3.4 \text{ \AA}$ and six fold symmetry is evident. In Figure A.7, an

image of the ‘interface’ between an iron catalyst and the graphene is given. The existence of the interface is critical to determine the growth mechanism of the graphene. Whether the graphene is actually bonded to the iron, or is just on top or below it is unclear from the image. A ‘wall’ model graphene would have a number of interfaces, while a flower model graphene would have very few if any (only resulting after the initial growth of the graphene). A high degree of order is evident in the image, so atomic spacings can be resolved. STEM imaging was performed, combined with EELS/EDX analysis. This revealed that the darkest spots in the STEM image were clusters of iron catalyst, which had carbon surrounding them. Towards the end of each of the layered carbon clusters, graphene sheets could be found. The catalyst is darkened in the image due to Z contrast. As one moves away from the catalyst, the growth of more single layers is evident. A low magnification image also lends credence to the flower model of growth. The carbon seems to surround clusters of iron particles, and after a critical point is reached, the layer opens up to form few layered or single layered graphene. A high magnification image of the zoomed in graphene is also given in Figure A.7.

After purification, some damage was noted in the graphene, which seems to have more folds, and the presence of iron was completely eliminated, according to EELS and EDX. The graphene does seem to have a tendency to not separate out into individual layers, but functionalization or better processing could eliminate that issue. Unfortunately, equipment constraints eliminated the possibility of measuring the thickness of the structure, but the material is obviously thin. Additionally, variations on the synthesis parameters would presumably lead to better control of layer number. The TEM images of Sample G are given in Figure A.8.

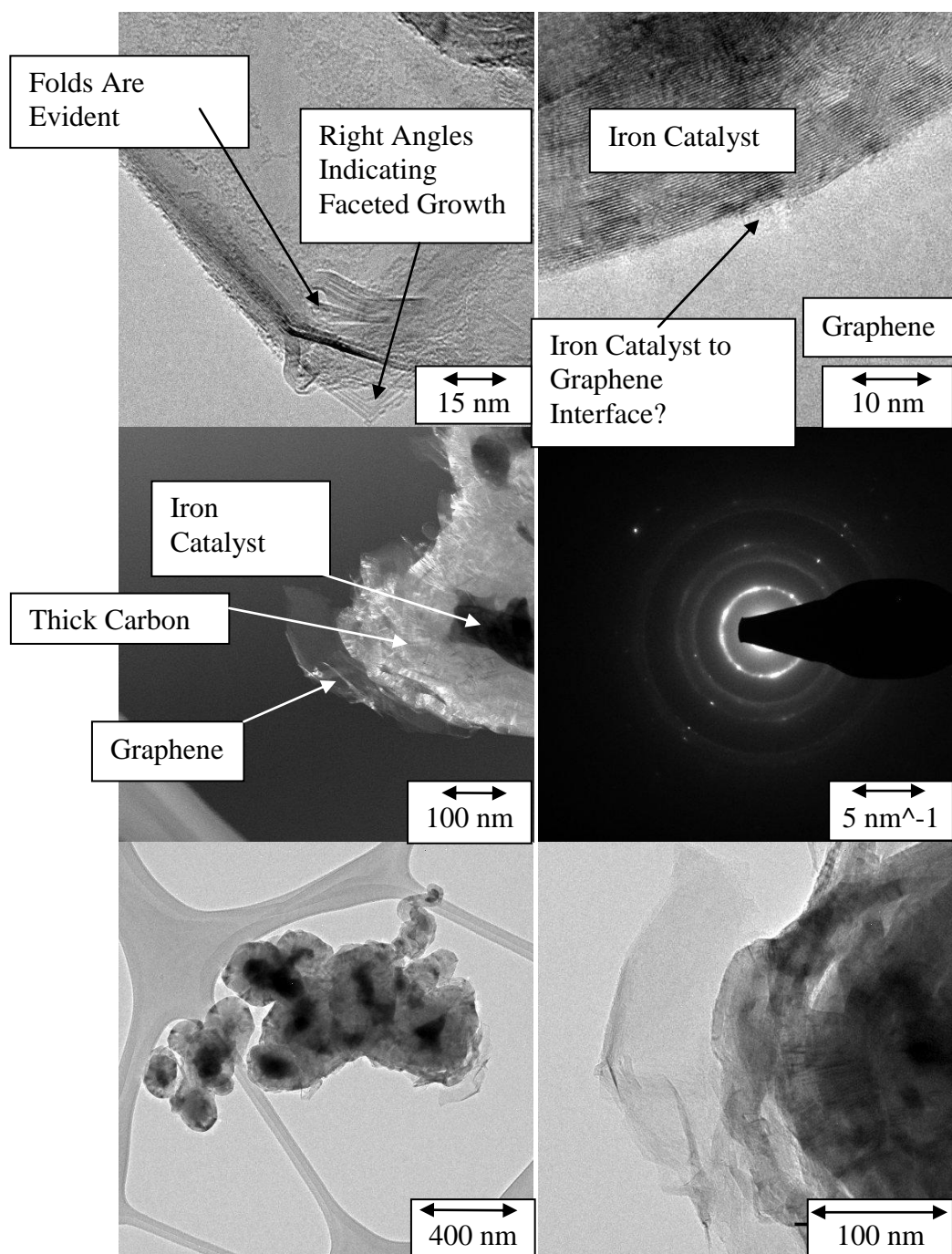


Figure A.7 (Top Left) TEM image showing clearly faceted growth, which is an indication of the growth of graphene. (Top Right) TEM image showing the catalyst-iron interface. Whether there is an actual connection, or if the iron particle is simply on top of the graphene or vice versa, is unclear. (Mid Left) STEM image of the sample. Note the contrast can be used to find the iron catalyst and also examine the relative thickness of the graphene. (Mid Right) Diffraction pattern showing 0.34 nm spacing and possible 6 fold symmetry indicative of layered carbon formation. (Bottom Left) Lower magnification TEM image of graphene growing on the 20 nm particle. (Bottom Right) Graphene growing from nanoparticles.

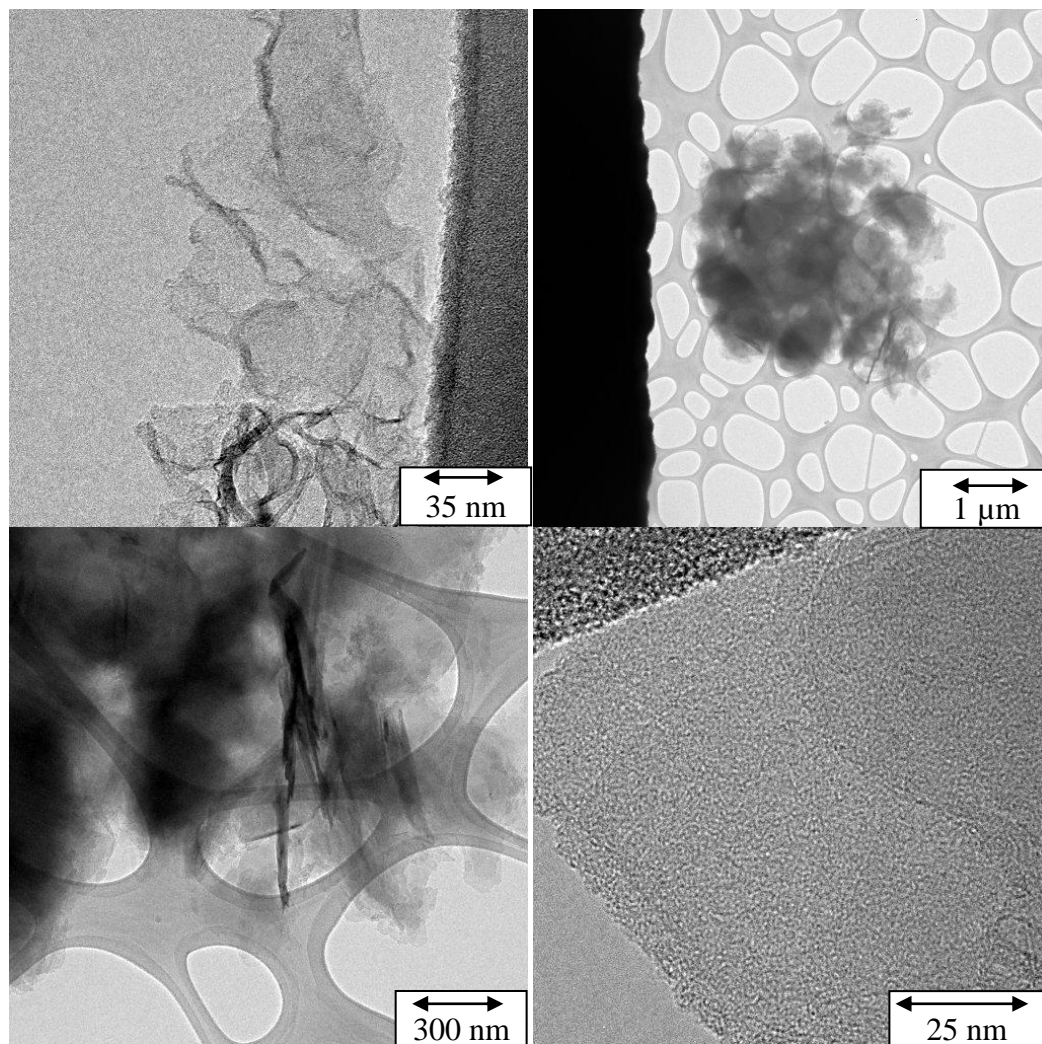


Figure A.8 (Top Left) Graphene with presumably very few layers forming a stack. (Top Right) Lower magnification TEM image of Sample G on TEM Grid. (Bottom Left) Higher magnification image showing that the graphene seems to agglomerate using the deposition methods discussed. (Bottom Right) High magnification of a particularly thin area of graphene which does not have many agglomerates.

A.5 Discussion

The experimental gases used were chosen based on processes designed to grow carbon nanotubes, however, this was obviously a different product. Therefore, an attempt was made to determine which reaction gases were actually critical for the experiment, which is why each one was removed. While the carbon monoxide and argon can be removed

without severely affecting the final product, the removal of acetylene eliminated the growth of any carbon nanomaterial. Acetylene is the crucial ingredient to induce the growth of the graphene. This was considered interesting, and seemed to indicate that a mixture of carbon and hydrogen with catalyst employed in this study could cause the growth of graphene. However, this was disproven. Replacing the acetylene with methane resulted in no carbon structures. Indeed, the only critical parameters for the growth of the graphene was a fast heating rate, which presumably reduced ripening, smaller initial particles, and the presence of acetylene, corroborating what was found in literature [10]. (While the argon and carbon monoxide did not severely impact the growth of graphene, they may have an effect on the ultimate amount of defects in the structure.)

The growth mechanism of the material is highly difficult to explain. Normally, in this scenario, one would expect the growth of multi walled carbon nanotubes [13, 15], not the growth of graphene. One possible mechanism of growth could be several of the iron catalysts are simultaneously surrounded by carbon layers which fold out. This is opposed to VLS models of carbon nanotube growth, where carbon would layer around each individual catalyst particle. Since a large number of particles are surrounded by graphene, the layers are under tension and have a tendency of opening up, forming flat, graphitic plates. This falls in line with the flower based model of growth which was discussed earlier. The wall method of growth seems unlikely, as one would expect the graphene which grew in that method to have dimensions restricted by the size of the catalyst particle. In the wall model, because they would only grow on one particle at a time, at least one dimension of the sheet would be restricted to the circumference of the particle which is approximately 63 nm on average for the 20 nm catalyst and 314 nm for

the 100 nm catalyst, and this does not seem to be the case. Additional evidence for the flower model is the image in Figure A.7 (Mid Left), which seems to be the material going through the bulb phase. The folds found in various images, if real, further reinforce the flower model. The formation of graphene with folds in it would be more believable in a flower model than a wall model. Finally, the graphene infiltration failed to produce high strength composites. This would hint at the flower based model as the correct model. The interface, if real, found in Figure A.7 could be explained by the graphene forming initially through the flower model, and then diffusing into the iron later. A pictorial explanation of the flower model is given in Figure A.9.

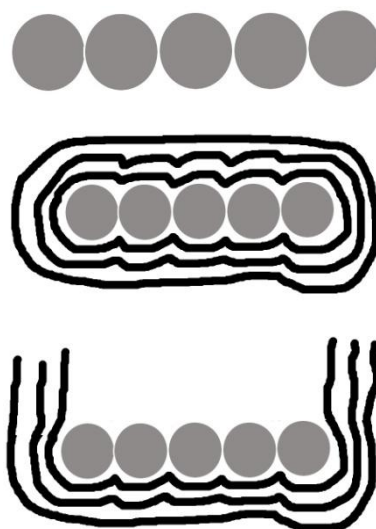


Figure A.9 Presumably, the flower model is the most accurate model to describe the growth conditions. (Top) Representative iron catalyst particles before growth, analogous to free standing ‘ovules.’ While only one flat layer is shown, any number of nanoparticles could simultaneously be surrounded by carbon layers which would eventually form graphene. (Middle) Iron catalyst surrounded by graphene layers, analogous to flower bulb. (Bottom) In this part of the image, the carbon layers are opening up to form graphene, analogous to a blooming flower petal. An arbitrary location was chosen as to where the carbon layer splits to form graphene in the image, although the split could happen anywhere in the layer.

This, according to the authors’ best knowledge, is the first successful synthesis of graphene using nanoparticles. This was also performed without using the traditional

metals for graphene growth, nickel and copper. This method has not been properly optimized using a design of experiments; however, it seems to be flexible as the presence of argon and/or carbon monoxide does not seem to strongly affect the growth of graphene, though it seems to be beneficial. One interesting note, the less acetylene used by concentration, the thinner the graphene that results in a given run. The runs which seem to 'dilute' the acetylene more seem to give better results. Acetylene is extremely critical, and cannot be replaced by carbon monoxide or methane.

This procedure should be easily scaled, unlike most methods of graphene production. The proper CVD parameters must be found before this can be done. The 100 nm catalyst does give some positive results, but they are not as dramatic as that of the 20 nm catalyst, and since the cost of each is relatively similar, most future work will focus on the 20 nm catalyst. The importance of a small particle size for a catalyst is shown by examining the effect of heating rate. When a fast heating rate is used, which can be assumed to lessen ripening, there is a considerably greater coverage of graphene which seems to be of a higher quality than that of the other methods. The general take away would be a small catalyst, reacted with acetylene, will result in the growth of graphene.

This novel growth mechanism is basically unexplored, and by varying a number of parameters it is possible that a method to create single layer graphene could be found. Additionally, yields could go up substantially, and a better method to purify the graphene should be investigated. This process is promising in that it could lead to a fairly efficient method of manufacturing graphene. High strength pellets could be possible, even if the flower model is the true model, using the method pioneered by Goyal et. al [12]. Post processing of the infiltrated pellet could be performed to cause bonding between the

graphene and iron particles, creating a possible enhancement in mechanical properties. Layer number determination was difficult, and better techniques should be employed in the future so that layer number can be determined accurately. Indeed, there are a number of promising future experiments possible through the method, due to the ease and the availability of reactants.

A.6 Conclusions

Graphene is an extremely exciting material, exhibiting properties which are entirely unique. While scientifically interesting, the cost of the material must be brought down considerably, while maintaining a high purity and low defect rate. The ability to grow graphene using a low temperature chemical vapor deposition process, using a commercially available catalyst nanopowder portends well for the economic viability of large scale graphene production. This implies that the large scale production of graphene can be performed easily, in a process that is cost competitive with multiwalled carbon nanotubes. The growth mechanism must also be examined. The fundamentals of the flower method of growth could reveal deep insights into the formation of graphene and other carbon nanostructures. Another interesting issue would be to determine why graphene grew primarily in these experiments, and not other carbon based materials such as carbon nanotubes. This was simply an initial set of experiments, a much more thorough study will be needed to fully understand the growth mechanism, and how best to exploit it.

APPENDIX B

RAPID SYNTHESIS AND CHARACTERIZATION OF AMORPHOUS MANGANESE OXIDE NANOWIRES/NANOFIBERS AT ROOM TEMPERATURE

B.1 Summary

Largely amorphous MnO_x nanowires/nanofibers consisting of curved one-dimensional structures have been synthesized. These nanostructures have the potential for use in exciting electrochemical applications [18-21], especially for energy storage. A relatively facile synthesis process is reported for producing mesoporous aggregates of this nanostructured material. This method is adapted from one used to synthesize nanoscale metal borides [22-25]. The ease with which the synthesis can be conducted portends well for process scale-up and use of the material as the cathode in lithium-ion batteries. X-ray diffraction, scanning and transmission electron microscopy, and Raman and inductively coupled plasma-atomic emission spectroscopy were performed to reveal critical details about the morphology, structure and composition of this material.

B.2 Introduction

Shrinking electronic devices and increasing costs of energy will necessitate more advanced methods of energy storage and manipulation in the future, especially for hand-held electronics, such as cell phones, tablet computers etc. This can be facilitated through the creation of novel materials with superior properties in comparison to those currently in use. Manganese oxide (MnO_x) nanowires offer an exciting opportunity for a number of applications related to these needs. Amorphous MnO_x has been reported to have an excellent specific charge storage capacity of between 160 and 350 mAh/g, and

can therefore function as a secondary lithium battery cathode, despite in some cases the presence of water and alkali metal ions within the amorphous structure [18]. If higher conductivity is required, the material can be readily prepared as a composite with carbon black or carbon nanotubes [19]. A nanostructured cathode would dramatically increase surface area, resulting in an improvement in electrochemical storage properties. Due to its high surface area, manganese oxide nanowires can function as cathodes [18], capacitors [20], and supercapacitors [21]. They are especially of interest as a more efficient and environmentally-friendly alternative for LiCoO_2 cathodes in lithium ion batteries. MnO_x is relatively simple to handle and manufacture in comparison to other materials normally used in batteries. Numerous methods of synthesis have been previously reported which result in high quality amorphous MnO_x nanowires [19]. However, each method involves elevated temperatures or long processing times. The process reported here is remarkably facile, involving no catalyst or templates, and can be performed at room temperature in about an hour. This suggests that MnO_x nanowires/nanofibers produced can be fabricated cost-effectively into lithium ion battery cathodes for large scale energy storage and production applications.

B.3 Experimental Details

The process to grow the nanowires was adapted from the method to grow iron boride detailed in the following references [22-25]. An aqueous solution of manganese sulfate (0.01 M, 500 mL) was added drop-wise using a pipette into an aqueous solution of potassium borohydride (0.1 M, 500 mL) over the course of 30 minutes. Gases were evolved from the reaction and the solution turned noticeably reddish brown. The

suspension was then filtered, and washed with water, ethanol, and acetone. The filtered solid was quickly placed in a desiccator under vacuum to dry overnight. The dried product had a dark, rusty color. When imaged in a scanning electron microscope, the solids displayed the morphology of nanowires and nanofibers in the form of large bundles. Attempts to use ultrasound to break apart the bundles caused severe damage to the nanowire/nanofiber structure as indicated by electron microscope imaging of the sonicated samples (see Figure B.3). Elemental analysis revealed a large degree of hydration, which was mostly removed by calcining the material at 500°C for 1 hour.

Scanning Electron Microscopy (SEM): SEM images were obtained with a VP-1530 Carl Zeiss LEO (Peabody, MA) field emission scanning electron microscope. The samples were mounted on aluminum stubs using double-sided carbon tape. Energy dispersive x-ray (EDX) analysis was performed in conjunction with SEM imaging.

Raman Spectroscopy: Raman spectra were obtained using a confocal Horiba-Jobin Yvon LabRam micro-Raman spectrometer with a 20 mW HeNe laser source emitting at a wavelength of 632.8 nm focused to a spot size of 10 μm with a 10x lens. The Raman conditions used follow: no filter, 300 μm hole, 200 μm slit, 2x15 sec acquisition time. All spectra given in the paper use units cm^{-1} .

Transmission Electron Microscopy (TEM): TEM was performed using a FEI CM-20FEG S/TEM equipped with a Gatan Enfina PEELS and a Oxford Max-80 SDD EDS systems. The samples were dispersed in ultra pure methanol, and a 1 μL drop of the solution was placed on a lacey carbon grid sitting on a filter paper. The TEM grid was then placed in a vacuum oven to dry at 80° C. EDX and electron energy loss spectroscopy (EELS) analysis were performed in conjunction with STEM analysis.

X-ray diffraction (XRD): The XRD was performed with a Rigaku Miniflex II on a zero background holder.

Chemical Analysis, ICP-AES (Inductively Coupled Plasma-atomic emission spectroscopy): A Thermo Scientific ICP was used for chemical analysis. An aliquot weighing 0.0102 g was dissolved in a mixture of 3 ml hydrochloric acid and 3 ml nitric acid. The solution was made up to 100 ml in a volumetric flask and a blank with only the acids was also prepared. Solutions diluted 25 times were used for determination of manganese whereas undiluted solutions were used for sulfur analysis. No manganese was found in the blank solution but sulfur is present in significant amounts in the blank, which is subtracted out. Manganese and sulfur were determined radially with excitation at 257 nm and at 180.7 nm, respectively.

B.4 Results and Discussion

Both EDX and EELS analyses confirmed the presence of manganese, oxygen, and sulfur in the samples. According to the ICP-AES chemical analysis (see Table B.1), discounting for measurable materials, the base left is 52.5%, which is assumed to be oxygen and water in the form of hydrates. Oxygen without hydration couldn't account for the large amount of unaccounted for material without creating a non-stoichiometric material. The assumption of the formation of hydrates is reasonable because manganese oxides can form them easily. Based on a roughly 2:1:1 ratio of oxygen to manganese to water, the following chemical reaction can be written for the synthesis:

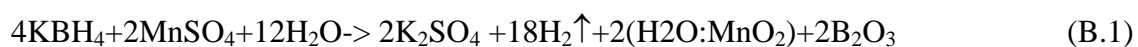
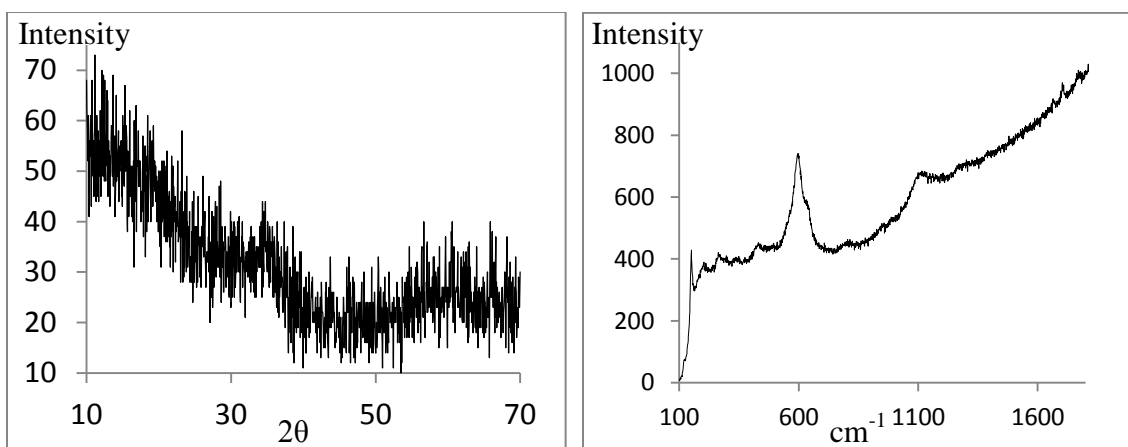


Table B.1 ICP Analysis for Product of Reaction Before and After Calcining at 500° C

Element (wt%)	Before Calcining	After Calcining
Mn	38.5%	45.6%
S	0.8%	0.8%
K	0.6%	0.9%
B	7.6%	9.2%
Base (Assume H ₂ O and O)	52.5%	43.5%

**Figure B.1** X-ray diffraction (left panel) and Raman (right panel) of the nanowire/nanofiber samples. X-axis in degrees and cm^{-1} respectively. See text for discussion.

This hydrolysis and reduction reaction would account for the loss of some of the boron as boric oxide which would dissolve in water and hydrogen would be evolved as gas. Similarly K_2SO_4 formed would dissolve in water and be removed during filtration. The small amounts of sulfur detected in the ICP analysis would come from unreacted MnSO_4 . The MnO_2 seems to be significantly hydrated as was found in a similar

experiment done previously [18]. The calcining process removed a significant amount of the base material, which can be assumed to be the structural water molecules of the hydrate.

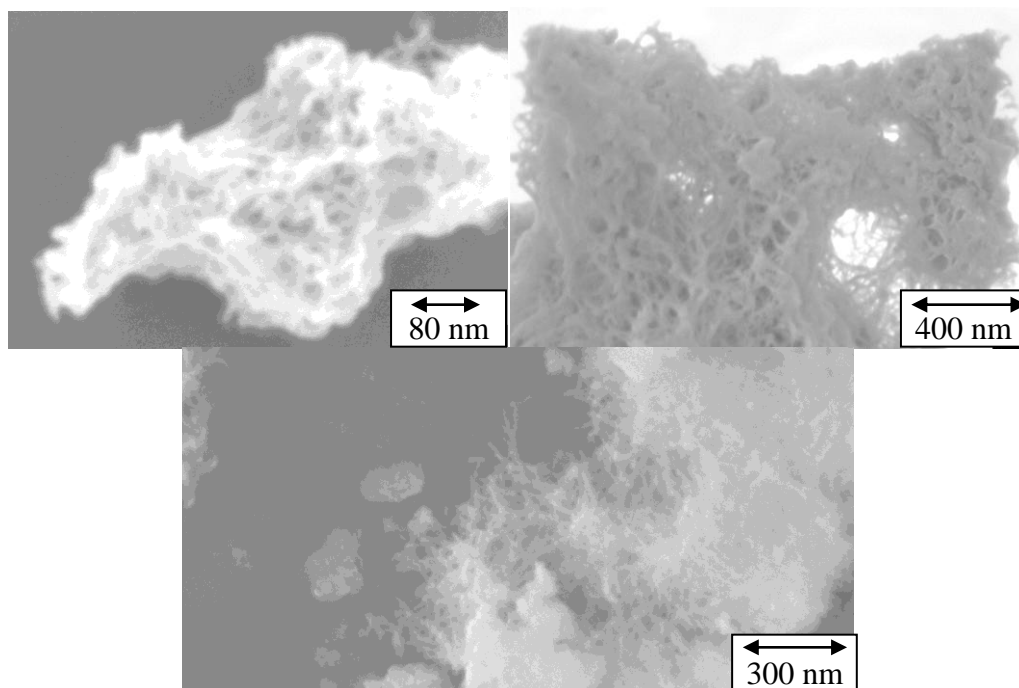


Figure B.2 SEM images of the samples showing agglomerated nanowire/ nanofiber morphologies.

The XRD and Raman data from the samples prepared before calcining are shown in Figure B.1. The XRD data reveal a relatively narrow line near 35° superimposed on a broad scattering band. There is a second broad scattering feature at about 60° . The XRD data can therefore be interpreted as arising from nanocrystallites embedded in an amorphous matrix. This is consistent with the Raman spectrum which shows a sharp lattice mode near 150 cm^{-1} associated with the crystallites, and two relatively broad Mn-O stretching modes near 600 cm^{-1} in agreement with the data of Sun et al. [26]. The broad features at 1200 and 1350 cm^{-1} correspond to second order scattering from the fundamental Mn-O lines. SEM images of the material shown in Figure B.2 indicate bundled, curved nanowires or nanofibers. The nanowires/nanofibers are typically <10

nm in diameter and bundle into agglomerated, mesoporous structures with expected high surface area similar to that described in reference [20].

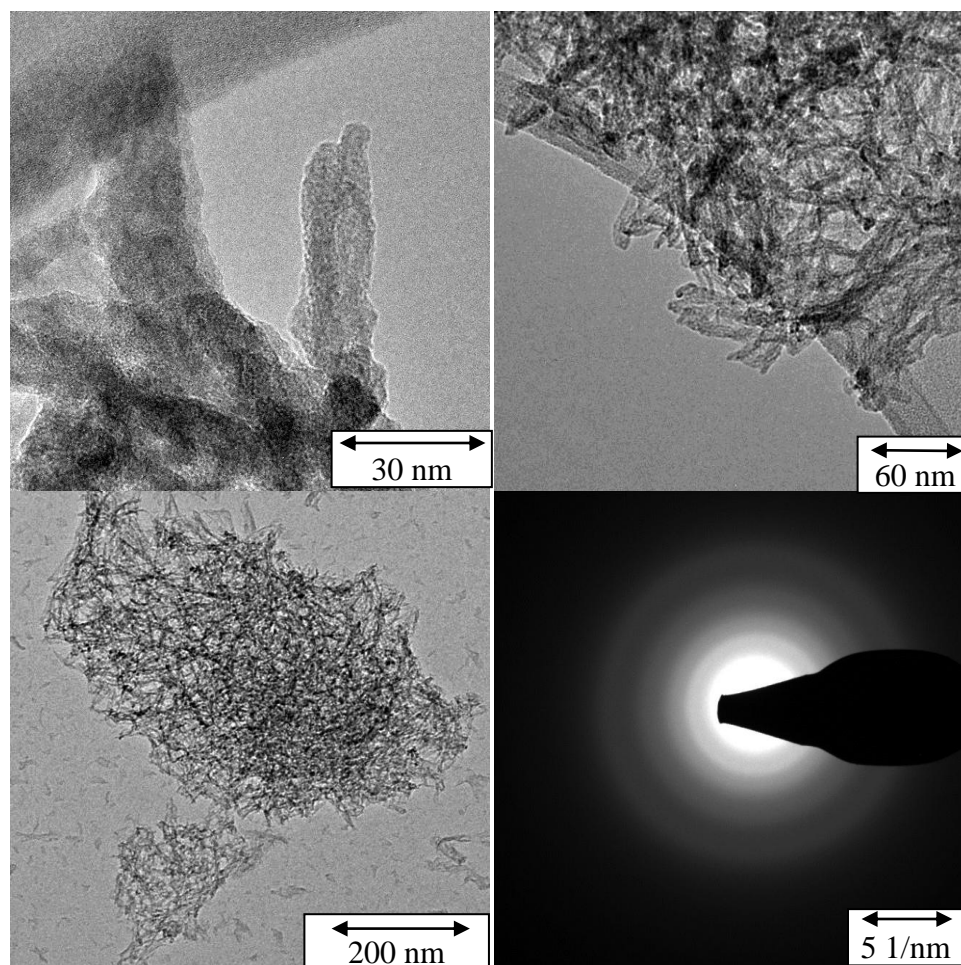


Figure B.3 TEM images and electron diffraction of the $\text{H}_2\text{O}:\text{MnO}_x$ nanowires/nanofibers before calcining: (Top Left) Higher resolution image of a nanowire protruding from a bundle. (Top Right) Lower magnification image of a bundle of nanowires/nanofibers. (Bottom Left) Nanowires/nanofibers after sonication showing that the sidewalls are extensively damaged. (Bottom Right) Typical selected area electron diffraction from the sample showing that the sample is largely amorphous.

The TEM images of the nanowires/nanofibers shown in Figure B.3 do not provide any new details. This is because breaking the agglomerates was found to be extremely difficult. Even after intense ultrasonication, the bundles were largely unbroken but the sidewalls of the individual nanowires/nanofibers appeared to have been damaged.

Therefore, TEM images were restricted to the nanowires/nanofibers protruding out of the agglomerates. These images revealed that the nanostructures are not straight, are relatively short, and are about 10 nm in diameter. The electron diffraction pattern is amorphous in contrast to XRD and Raman data, which suggest that nanocrystals are embedded in an amorphous matrix. TEM EELS/EDX analysis confirmed the nanowires were composed of Mn and O. Hydrogen could not be measured using EELS, but inference from the ICP measurements indicates that the nanowires are hydrated. The material which was not nanowires most likely is the location of the other elements from the ICP analysis, and some $\text{H}_2\text{O}:\text{MnO}_x$ as well. More detailed TEM analysis would require the synthesis of less agglomerated nanowires/nanofibers, perhaps using suitable surfactants.

SEM, XRD, and Raman analysis were also performed on the material after calcining at 500°C (Figure B.4) for 1 hour. Calcining changed the color of the material from rust red to brownish black. This process should remove a significant amount of the hydrate present and presumably alter the structure of the material. However, SEM analysis indicates the presence of nanowires, showing they survive the calcining process. XRD indicates the calcining process creates a crystalline material with sharp peaks at the following: 33° , 38° , 42° , 56° , and 66.5° , showing the amorphous component of the material is removed. Finally, the Raman signal does show changes to the character of the double peak near 600 cm^{-1} , where the second peak rises in intensity, but overall the spectrum appears unaltered. Therefore, the calcining process does not significantly alter morphology or bond character, but does seem to induce crystallization of the amorphous component of the material. This also means that water can leave and enter the structure

without causing any appreciable damage. The XRD pattern of the calcined material has a strong match to braunite, but since no silicon in the sample it cannot match with this material. The lack of silicon was doubled checked by rerunning ICP to confirm the material cannot be braunite.

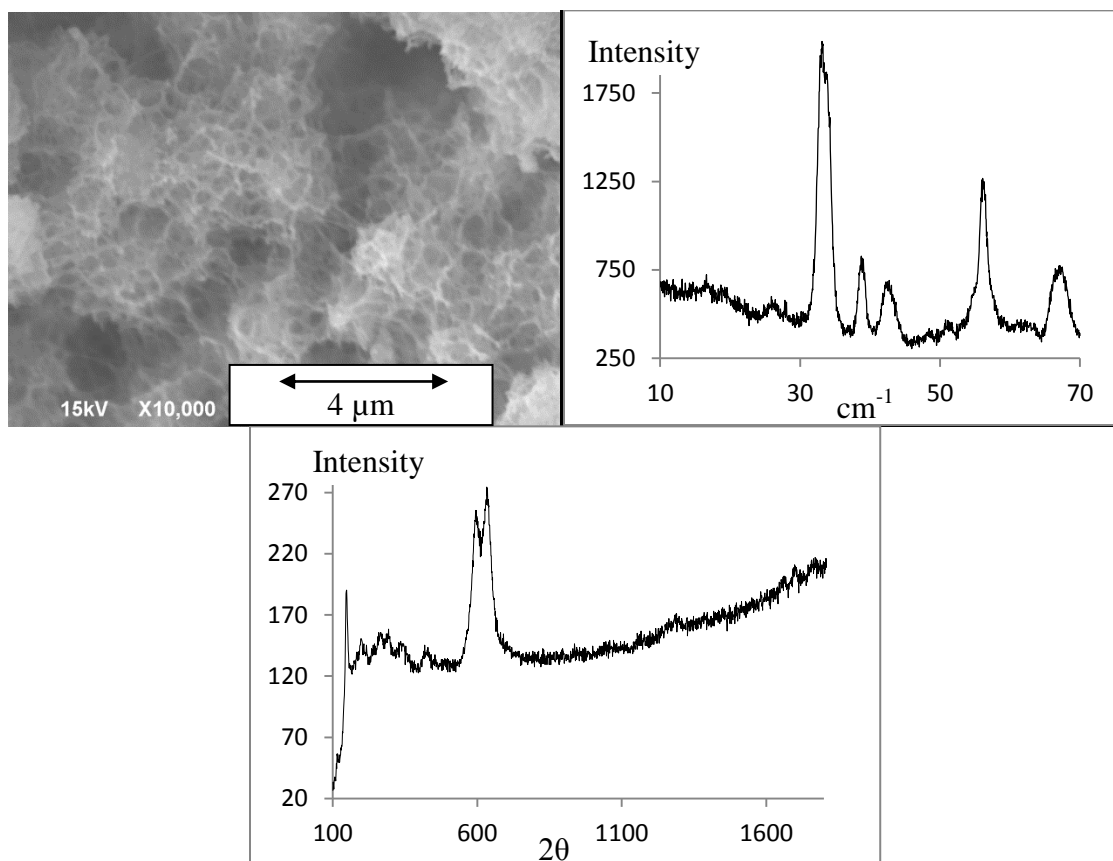


Figure B.4 (Top Left) SEM of calcined nanowires. Note the nanowire morphology is still intact. (Top Right) XRD of calcined nanowires, which indicates the calcining process creates a more crystalline material. (Bottom) Raman of calcined material. Interestingly, the Raman signal is not dramatically altered through the calcining process.

In conclusion, a scalable room temperature aqueous solution process involving the reduction of manganese sulfate to rapidly synthesize a largely amorphous wire or fiber-like oxide nanostructure is described. Interestingly, however, if nickel or iron sulfate is used in a similar reaction [22-25], the resulting product is nanosized nickel or

iron boride. The reason why the use of manganese sulfate gives oxide nanowires/nanofibers could provide insights into reduction reactions of this type, which could be useful for developing low temperature solution synthesis processes for other nanowires. The electrochemical properties of these manganese oxide nanostructures have not been determined, but prior work in the literature [18-21] indicates these materials should have great potential in a number of different applications. The material can be calcined to remove a good portion of the water, but this may alter the ability of the material to have reversible Li insertion [18]. The calcining process does seem to induce crystallization, however, it does not affect morphology and bond character. The dehydrated nanowires might have some uses as well, and only further investigation will reveal the possible applications of these materials.

APPENDIX REFERENCES

1. K. S. Novoselov, A. K. Geim, S. V. Morozov, D. Jiang, Y. Zhang, S. V. Dubonos, I. V. Grigorieva¹, and A. A. Firsov: Electric Field Effect in Atomically Thin Carbon Films. *Science*. **306**, 666 (2004).
2. Nobelprize.org. *The Nobel Prize in Physics 2010*. 2010
[cited 2012 31 Aug 2012]; Available from:
http://www.nobelprize.org/nobel_prizes/physics/laureates/2010/.
3. A.K. Geim and K.S. Novoselov: The rise of graphene. *Nat. Mater.* **6**, 183 (2007).
4. Z. Chen, W. Ren, B. Liu, L. Gao, S. Pei, Z.-S. Wu, J. Zhao, and H.-M. Cheng: Bulk growth of mono- to few-layer graphene on nickel particles by chemical vapor deposition from methane. *Carbon*. **48**, 3543 (2010).
5. M. Losurdo, M. M. Giangregorio, P. Capezzuto, G. Bruno: Graphene CVD growth on copper and nickel: role of hydrogen in kinetics and structure. *Phys Chem Chem Phys*. **14**, 13 (2011).
6. A. Reina, S. Thiele, X. Jia, S. Bhaviripudi, M. S. Dresselhaus, J. A. Schaefer, and J. Kong: Growth of Large-Area Single and Bi-Layer Graphene by Controlled Carbon Precipitation on Polycrystalline Ni Surfaces. *Nano Research*, **2**, 509 (2009).
7. C. Mattevi, H. Kim, M. Chhowalla: A review of chemical vapour deposition of graphene on copper. *Journal of Materials Chemistry*. **21**, 3324 (2010).
8. K. S. Kim, Y. Zhao, H. Jang, S. Y. Lee, J. M. Kim, K. S. Kim, J.-H. Ahn, P. Kim, J.-Y. Choi, and B. H. Hong: Large-scale pattern growth of graphene films for stretchable transparent electrodes. *Nature*. **457**, 706 (2008).
9. N. A. Vinogradov, A. A. Zakharov, V. Kocevski¹, J. Ruzs¹, K. A. Simonov, O. Eriksson, A. Mikkelsen, E. Lundgren, A. S. Vinogradov, N. Mårtensson, and A. B. Preobrajenski: Formation and Structure of Graphene Waves on Fe(110). *Physical Review Letters*. **109**, 026101 (2012).
10. H. An, W.-J. Leea, J. Jung: Graphene synthesis of Fe foil using thermal CVD. *Current Applied Physics*. **11**, S81. 2011.
11. A. S. Khan, Y.S. Suh, X. Chen, L. Takacs, and H. Zhang: Nanocrystalline aluminum and iron: Mechanical behavior at quasi-static and high strain rates, and constitutive modeling. *International Journal of Plasticity*. **22**, 195 (2006).
12. A. Goyal, D.A. Wiegand, F.J. Owens, and Z. Iqbal: Enhanced yield strength in iron nanocomposite with in situ grown single-wall carbon nanotubes. *Journal of Materials Research*. **21**, 522 (2005).
13. A. Goyal, D.A. Wiegand, F.J. Owens, and Z. Iqbal: Synthesis of carbide-free, high strength iron-carbon nanotube composite by in situ nanotube growth. *Chemical Physics Letters*. **442**, 365 (2007).
14. A. Goyal: *New Approaches To Scaled-up Carbon Nanotube Synthesis and Nanotube-based Metal Composites and Sensors*. 2006, PhD Dissertation New Jersey Institute of Technology.

15. R. B. Patel, J. Liu, S. Roy, S. Mitra, R. N. Dave, and Z. Iqbal: Formation of stainless steel–carbon nanotube composites using a scalable chemical vapor infiltration process. *Journal of Materials Science*. **48**, 1387 (2013).
16. R. B. Patel, J. Liu, J. Eng, and Z. Iqbal: One-step CVD synthesis of a boron nitride nanotube-iron composite. *Journal of Materials Research*. **26**, 1332 (2011).
17. M. J. Matthews, M. A. Pimenta, G. Dresselhaus, M. S. Dresselhaus, and M. Endo: Origin of dispersive effects of the Raman D band in carbon materials. *Physical Review B*. **59**, R6585 (1999).
18. W. C. West, N.V. Myung, J. F. Whitacre, B. V. Ratnakumar: Electrodeposited amorphous manganese oxide nanowire arrays for high energy and power density electrodes. *Journal of Power Sources*. **126**, 203 (2004).
19. J.-S. Lee, G.S. Park, H. Lee, S. T. Kim, R. Cao, M. Liu, and J. Cho: Ketjenblack Carbon Supported Amorphous Manganese Oxides Nanowires as Highly Efficient Electrocatalyst for Oxygen Reduction Reaction in Alkaline Solutions. *Nanoletters*. **11**, 5362 (2011).
20. W. Yan, T. Ayvazian, J. Kim, Y. Liu, K. C. Donovan, W. Xing, Y. Yang, J. C. Hemminger, and R. M. Penner: Mesoporous Manganese Oxide Nanowires for High-Capacity, High-Rate, Hybrid Electrical Energy Storage. *ACS Nano*. **5**, 8275 (2011).
21. H. Liu, B. Lu, S. Wei, M. Bao, Y. Wen, and F. Wang: Electrodeposited highly-ordered manganese oxide nanowire arrays for supercapacitors. *Solid State Sciences*. **14**, 789 (2012).
22. J.J. Fu, Y.N. Lu, H. Xu, K. F. Huo, X. Z. Wang, L. Li, Z. Hu, and Y. Chen: The synthesis of boron nitride nanotubes by an extended vapour-liquid-solid method. *Nanotechnology*. **15**, 727 (2004).
23. Z. Hu, Y. Fan, F. Chen, and Y. Chen: Amorphous iron–boron powders prepared by chemical reduction of mixed-metal cation solutions: dependence of composition upon reaction temperature. *Journal Chemical Society: Chemical Communications*. (1995).
24. J. Jiang, I. D’ezsi, U. Gonser and X. Lin: A study of the Preparation Conditions of Fe-B Powders Produced by Chemical Reduction. *Journal Non-Crystalline Solids*. 124 (1991).
25. Z. Hu, Y. Fan, and Y. Chen: Preparation and characterization of ultrafine amorphous alloy particles. *Applied Physics A*. **68**, 225 (1999).
26. M. Sun, B. Lan, L. Yu, F. Ye, W. Song, J. He, G. Diao, and Y. Zheng: Manganese oxides with different crystalline structures: Facile hydrothermal synthesis and catalytic activities. *Materials Letters*. **86**, 18 (2012).